A STUDY OF POROUS ELECTRODES FOR DNA ELECTROCHEMICAL DETECTION AND THE DEVELOPMENT OF A HYBRIDIZATION EFFICIENCY CHARACTERIZATION TECHNIQUE

A Study of Porous Electrodes for DNA Electrochemical Detection and the Development of a Hybridization Efficiency Characterization Technique

By BARNABAS FUNG, B.Eng.

A Thesis Submitted to the School of Graduate Studies in Partial Fulfilment of the Requirements for the Degree Master of Applied Science

McMaster University MASTER OF APPLIED SCIENCE (2016) Hamilton, Ontario

(Engineering Physics)

TITLE: A Study of Porous Electrodes for DNA Electrochemical Detection and the Development of a Hybridization Efficiency Characterization Technique

AUTHOR: Barnabas Fung, B.Eng.

SUPERVISOR: Dr. Leyla Soleymani

NUMBER OF PAGES: 145

Abstract

Point-of-care DNA diagnostics for resource-limited settings require high sensitivity and low limits of detection but is constrained by a limitation on the complexity of instrumentation and resource consumption. To assist in the research and development of such technology, rapid-prototyping offers quick turnaround times from ideation to proof-of-concept testing at reduced costs.

All-solution processed electrodes which exhibit micro/nano-scale wrinkling and porosity were rapidly-prototyped. Probe density was shown to be tunable with these electrodes and densities were greater than planar electrodes due to a surface area enhancement. Such electrodes also demonstrated favorable characteristics for the electrocatalytic detection of DNA hybridization.

Characterization of hybridization efficiency for DNA biosensors often require the determination of probe and target DNA densities in separate experiments, relying on averaged measurements which lose device specificity. A new method to quantify hybridization efficiency was developed which allows the label-free, sequential determination of probe DNA and target DNA density in one experiment, allowing electrode-specific characterization of hybridization efficiency.

Acknowledgements

"Most pioneers are at the mercy of doubt of the beginning, whether of their worth, of their theories, or of the whole enigmatic field in which they labor"

- *Goethe*

It is with extreme gratitude and humility that I present this work, which is the product of a journey starting from self-doubt and ending in self-confidence. In truth, it was the guidance of Professor Leyla Soleymani that has been critical to my success, especially her demonstration of resilience, patience, and acute scientific ability which I have learned from. For these reasons and more, I extend my thanks.

I would also like to thank the Departments of Biomedical Engineering and Engineering Physics and their respective administrative staff for their provision. I also thank the Biointerfaces Institute, the Centre for Emerging Device Technologies and the Canadian Centre for Electron Microscopy for their facilities and expertise. I would also like to acknowledge the Government of Ontario and McMaster University for their financial support.

The way was fraught with many dangers, toils and snares, and I have many people to thank for helping me persevere to overcome my challenges. I express deep gratitude to Mr. Amin Hosseini, Ms. Christine Gabardo, Ms. Jie Yang, and Mr. Stephen Woo who were my lab-mates, comrades, and teachers. Their comradery and fellowship provided a worthwhile and enjoyable experience. To those people who could not be named here but have provided me assistance even in the smallest of ways – thank you!

I am eternally grateful for the unconditional love of my parents, Cam and Ellen, and my brothers, Solomon and Nathanael. For without this, I am truly destitute.

This work is dedicated to the ever-expanding greatness achievable by the coming together of people. Nothing great can be done alone.

My Utmost for His Highest

Table of Contents

List of Figures

List of Tables

List of Equations

List of Abbreviations

AIDS	acquired immunodeficiency syndrome
APTES	(3-aminopropyl)triethoxysilane
ARI	acute respiratory infections
Au-NP	gold nanoparticle
CA	chronoamperometry
CC	chronocoulometry
CNT	carbon nanotube
CV	cyclic voltammetry
DC	direct current
DI	deionized
DTNB	5,5'-dithiobis-(2-nitrobenzoic acid), Ellman's reagent
DNA	deoxyribonucleic acid
DOD	drop-on-demand
DPV	differential pulse voltammetry
dsDNA	double-stranded deoxyribonucleic acid
E. Coli	escherichia coli
EDTA	ethylenediaminetetraacetic acid
EIS	electrical impedance spectroscopy
FiCN	ferricyanide, $[Fe(CN)_6]^{3-}$
FoCN	ferrocyanide, $[Fe(CN)_6]^{4-}$
HDA	helicase-dependent amplification
HIV	human immunodeficiency virus
IPA	isopropyl alcohol
ISE	ion-selective electrode
ITO	indium tin oxide
IUPAC	international union of pure and applie chemistry

LAMP	loop-mediated isothermal amplification
LF	lateral flow
LOC	lab-on-a-chip
MCE	2-mercaptoethanol
MCH	6-mercapto-1-hexanol
MEMS	microelectromechanical systems
MWCNT	multi-wall carbon nanotubes
NHE	normal hydrogen electrode
NMR	nuclear magnetic resonance
PAN	polyaniline
PB	phosphate buffer
PCR	polymerase chain reaction
PDMS	polydimethylsiloxane
PEDOT	poly-3,4-ethylenedioxythiophene
PET	poly(ethylene terephthalate)
PNA	peptide nucleic acid
POC	point-of-care
PPy	polypyrrole
PS	polystyrene
PSPS	pre-stressed polystyrene
PVC	polyvinyl chloride
RCA	rolling cyclic amplification
RuHex	ruthenium hexamine, $[Ru(NH_3)_6]^{3+}$
QCM	quartz-crystal microbalance
SAM	self-assembled monolayer
SAW	surface acoustic wave
SEM	scanning electron microscopy
SHE	standard hydrogen electrode

SPE	screen-printed electrodes
SPR	surface plasmon resonance
ssDNA	single-stranded deoxyribonucleic acid
STI	sexually transmitted infection
SWCNT	single-wall carbon nanotubes
TB	tuberculosis
TE	tris-EDTA
WEDPE	wrinkled, electrolessly-deposited polystyrene elctrodes
WHO	world health organization
WSPE	wrinkled, sputtered polystyrene electrodes

1.0 Introduction

1.1 Point-of-Care (POC) Diagnostics

Point-of-care diagnostics refer to the performance of biochemical, hematological, coagulation, or molecular diagnostic tests at or near a patient (decentralized), such that the reliance on laboratories and skilled professionals (centralized) for sample processing are minimized or even eliminated [1]. POC diagnostics have proven to be transformative to global healthcare, as health outcomes have shown improvements owing to better disease management [2]. POC testing of diabetes, pregnancy, human immunodeficiency virus (HIV), malaria, and anaemia have become common diagnostic tools in both high- and low-income countries [3].

1.1.1 POC Market

In 2014, the global sale of POC diagnostics reached $17 billion and is expected to reach $20.4 billion by 2019 with 3.7% compounded annual growth. The POC market is divided into two segments: self-testing products (48.5% of 2014 revenue) and professional products (51.5%) [4]. Self-testing products are self-administered tests and can be categorized as those shown in Table 1.1 below. Blood glucose POC testing for diabetes dominates this market with 87.7% share, amounting to $7.24 billion.

Table 1.1 Global POC Self-Testing Market Analysis by Product Subcategory, 2014 [5]

Product Type	**Revenues Estimates (in millions $)**	**Market Share (%)**
Glucose	7,235.00	87.7
Pregnancy & Fertility	701	8.5
Fecal Occult Blood	116.4	1.4
Rapid Coagulation	86.5	1
Drugs of Abuse	56.6	0.7
Urine Strip	26	0.3
Infectious Disease	17.8	0.2
Cholesterol	15.1	0.2
Total	**8,254.40**	**100**

Professional products are diagnostic tests which cannot be classified as self-administered products and cannot easily be obtained over-the-counter. These products are presented in Table 1.2 below.

Table 1.2 Global POC Professional Testing Market Analysis by Product Subcategory, 2014 [5]

Product	Revenues Estimates (in millions $)	Market Share (%)
Drugs of Abuse	2,391.40	27.3
Blood & Electrolytes	1,561.00	17.8
Glucose	1,498.00	17.1
Infectious Disease	940.00	10.7
Rapid Coagulation	587.00	6.7
Cardiac Markers	555.00	6.3
Fecal Occult Blood	492.00	5.6
Cholesterol	292.00	3.3
Pregnancy & Fertility	137.00	1.6
Miscellaneous	118.00	1.4
Urine Strip	99.00	1.2
Cancer	90.80	1
Total	**8,761.20**	**100**

1.2 POC Infectious Disease Diagnostics for Resource-Limited Settings

The impact and utility of POC diagnostics for infectious diseases in the developing world cannot be understated, as infectious disease is the major cause of morbidity and mortality in these locations [6], accounting for more than half of all infant mortalities [7]. At least 95% of deaths caused by infectious diseases world-wide, especially acute respiratory infections (ARIs), HIV, malaria, and tuberculosis (TB) occur in developing countries. Classic diagnostic techniques for these diseases often require access to laboratory facilities which require not only proper instrumentation, but adequate access to electricity, plumbing, and waste disposal. Skilled expertise is required to administer aid but often cannot meet demand, causing patients to abandon the healthcare setting before diagnosis is given [8]. In the absence of adequate diagnostic techniques, certain diseases (ex. STIs) are diagnosed by syndromic management, which is endorsed by the World Health Organization (WHO); however, diseases which do not present symptoms are not treated, and patients are given treatments without proper diagnosis [9].

To this end, POC devices were shown to contribute to the decrease in the use of inappropriate anti-malarial medication in Africa, and to the doubling of the rate in antiretroviral therapies and halving the initiation times of these therapies [3]. POC devices are also often used as the sole diagnostic method due to resource and infrastructure limitations, as is the case for syphilis in South Africa [10].

Despite the positive impacts made by POC diagnostics in resource-limited settings, much work is still required to face the present and future challenges due to the global burden of disease. The world population is currently estimated at 7.1 billion and is expected to climb to 9.4 billion by 2050. Currently, the Zika virus has been declared as an internal health concern by the WHO, and molecular tests to achieve selectivity between acute dengue, chikungunya, and Zika viruses has become top priority [11]. Global HIV/AIDS deaths is predicted to rise to 6.5 million in 2030 [12]. These statistics emphasize the need for the continual development of POC diagnostic technology for both developed and developing worlds.

1.2.1 Current Nucleic Acid Testing Platforms for the POC

The WHO suggests that new diagnostic POC devices for the developing world should meet the criteria of ASSURED: Affordable, Sensitive, Specific, User-Friendly, Rapid & Robust, and Equipment-Free-Delivered [13]. In 2011, the WHO endorsed the Cepheid GeneXpert for diagnosis of TB and multi-drug resistant TB for high-burden, low-resource settings where TB is endemic[1]. However, the cost and complexity of this device prevents its use as a truly POC diagnostic device [14]. A sample of commercial POC nucleic acid testing products that are in market or close to market are given in Table 1.3 below.

[1] http://www.who.int/mediacentre/news/releases/2010/tb_ test_20101208/en/index.html

Table 1.3 A listing of several commercially available or soon-to-be available POC diagnostic platforms as of 2011 [14].

Platform	Manufacturer	Detection	Amplification
GeneXpert	Cepheid	Fluorescence	PCR
Liat Analyzer	IQuum	Fluorescence	PCR
MDx	Biocartis	Fluorescence	PCR
FL/ML	Enigma	Fluorescence	PCR
FilmArray	Idaho Technologies	Fluorescence	PCR
Razor	Idaha Technologies	Fluorescence	PCR
R.A.P.I.D	Idaha Technologies	Fluorescence	PCR
LA-200	Eiken	Turbidimetry	Isothermal
Twista	TwistDX	Fluorescence	Isothermal
BART	Lumora	Bioluminescence	Isothermal
Genie II	Optigene	Fluorescence	Isothermal
SAMBA	Diagnostics for the Real World	Lateral Flow	Isothermal
BESt Cassette	BioHelix/ Ustar Biotech	Lateral Flow	Isothermal

All of the devices listed in Table 1.3, as well as for POC nucleic acid testing platforms in general contain three stages. These include sample preparation, amplification, and detection stages.

In the sample preparation stage, the specimen is processed from the raw biological environment to remove the specific molecule of interest (in this case, nucleic acids) from its native environment and to prepare it for the amplification stage. Sample preparation often poses as a bottleneck for POC device development as many complex laboratory functions must be performed in a controlled and sequential manner, typically including sample concentration and enrichment, drop metering, mixing, and the controlled introduction of various reagents [15]. All of these functions are typically performed with microfluidic/microelectromechanical systems (MEMS) components as a necessity for the smaller device format in POC devices. This preparatory stage also typically involves a lysing step which is necessary to release nucleic acid content from larger molecules, followed by a solid-phase extraction whereby the nucleic acid is captured or filtered from other biological components by attaching to a solid support (typically biologically-modified beads or magnetic particles). This step is necessary to remove any inhibitory agents from passing on to the amplification stage (ex. DNAse or other nucleases) which can affect amplification.

Amplification is necessary to create enough copies of pathogenic DNA to reach assay detection limits (commonly at least 100 copies/mL of the pathogen [14]). The most common technique to achieve this is by polymerase chain reaction (PCR), which is a conventional laboratory DNA duplication technique requiring intervals of cooling and heating steps, which has been implemented in many miniaturized PCR designs applicable to POC diagnostics [16]. However, PCR requires instrumentation to perform thermocycling, which is a cost in POC device design. To address this limitation, other nucleic acid amplification techniques have been explored which permit the amplification of DNA at a single temperature - isothermal amplification - which require less complex and costly instrumentation for POC diagnostic applications.

Following amplification is the detection stage. Detection methods can be broadly categorized as either real-time, in which the detection occurs during amplification, or endpoint, in which detection occurs at the conclusion of amplification [14]. Fluorescence detection is a commonly used method which employs optical detection of either fluorescent dyes or fluorophore-modified probe molecules which bind to the analyte being detected. Lateral flow (LF) detection is an end-point analysis technique which uses a sandwich assay approach for detection – the target analyte binds to a capture element, whereupon a reporter molecule binds to the captured target. Other optical techniques include turbidimetry which measures the change in particle density within a solution, and optical detection of bioluminescence – light emitted from a biologically-relevant molecule [17].

The possibility of relying less on amplification techniques remains an attractive option to simplify instrumentation requirements, reduce costs, and potentially achieve quicker detection-to-readout time. To achieve this, detection limits must be low enough to be able to detect low analyte concentrations found in samples without amplification. This feature will require research and development in biosensing technology.

1.3 Biosensors

Although many definitions exist for what a “biosensor” is, the IUPAC definition describes a biosensor as “a self-contained integrated device which is capable of providing specific quantitative or semi-quantitative analytical information using a biological recognition element which is in direct spatial contact with a transducer” [18]. Two elements are key: a bio-

recognition element which allows the capture of specific target molecules of interest, and a transduction mechanism which transforms the capture event into a useful signal [19]. These are depicted in Figure 1.1 below.

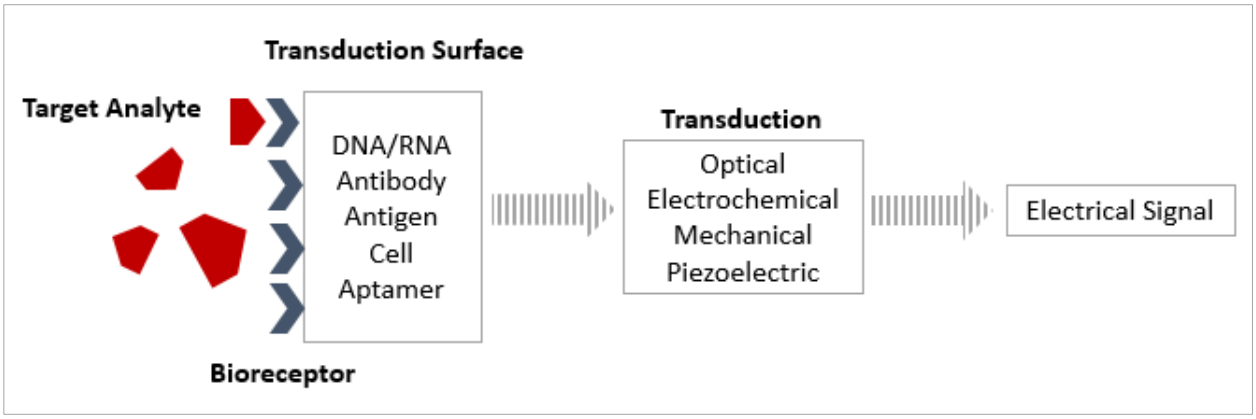

Figure 1.1 Major components of a biosensor, including a bio-recognition element composed of bioreceptors and a transduction mechanism (adapted from [19])

Biorecognition elements can be broadly divided into two categories: affinity-based and catalytic biosensors, which describe the nature of the interaction between target analyte and recognition element. In affinity-based biosensors, the analyte is permanently or semi-permanently bound to the recognition element. Such biosensors include immunobiosensors (antibody-antigen), nucleic-acid sensors (hybridization of probe with complementary target), and receptor-based sensors [20]. In catalytic biosensors, the analyte is reversibly bound, such that products from chemical reactions initiated by the capture process are detected. This class of biosensor includes enzyme-based sensors, whole-cell biosensors relying on biocatalytic reactions, and sensors relying on catalytically-active polynucleotides (ex. DNAzymes) [21].

Signal transduction techniques can be divided between labeling and label-free techniques. Labeling techniques require a reporter molecule with an identifiable characteristic that binds to the captured target analyte such that quantitation of targets is possible. Label-free techniques do not require these reporter molecules and signal transduction occurs without modification to the captured molecule. Common transduction techniques include optical, mechanical, piezoelectric, and electrochemical methods.

Optical detection is a technique which relies on either the naturally-occurring optical properties of the captured analyte or the products, or by the detection of reporter molecules with optical

properties. The former technique detects changes in absorbance, emission, polarization, or luminescence decay, but usually exhibit poor sensitivity owing to background-generated signals [21]. Instead, optical detection of a biomolecule which is covalently modified is performed, which is beneficial due to the ability to tune the detection wavelength to look for the signal of interest. An example of this is in fluorescence detection where fluorophore-modified reporter molecules are detected (as mentioned for the detection techniques for the POC platforms previously discussed). Another optical transduction technique is surface plasmon resonance (SPR) which is a label-free technique that measures the change in the critical angle at which a minimum intensity of reflected light occurs at the interface of media with different refractive indices.

Mechanical and piezoelectric transduction techniques can be considered as mass-sensitive techniques. Surface acoustic wave (SAW) and quartz-crystal microbalance (QCM) represent two of the most common techniques which utilize a piezoelectric element that converts between electrical and mechanical energy. In SAW, acoustic waves are generated by a piezoelectric element which are confined to the surface of the detection area with biorecognition elements [22]. Changes to properties of the SAW, such as velocity or amplitude, can be detected and correlated to the capture of target biomolecules [23]. In QCM, the oscillation of a piezoelectric element changes depending on the mass loading of the element. Capture of biomolecular targets is correlated to an increased loading of the element and the change in oscillation is detected electronically. Mechanical biosensors often employ microcantilevers which translate biorecognition events to the stress-induced bending of a solid element [24]. The deflection of the cantilever can then be detected by optical, capacitive, or piezoelectric/resistive techniques [25].

Electrochemical transduction is an especially attractive transduction technique owing to the simplicity in instrumentation and design requirements over other techniques and its ease of fabrication with micro/nano-fabrication [26]. Briefly, electrochemical detection relies on the changes in electron-transfer between an electrode and species at the electrode surface by monitoring the potential, current, or impedance changes to reduction-oxidation reactions. It is this method of biosensing which the work contained in this thesis employs.

1.4 Thesis Objectives & Overview

As such, the work herein pertains to the development of electrochemical nucleic-acid biosensors for POC diagnostics, pursuing the following objectives:

- **I.** To rapidly-fabricate micro/nano-structured electrodes using an all-solution-processing technique,
- **II.** To characterize the binding of probe DNA to these electrodes by variations in deposition time and probe molar fraction,
- **III.** To demonstrate the electrocatalytic detection of DNA hybridization using these electrodes, and
- **IV.** To develop a label-free technique for the characterization of DNA hybridization efficiency by the sequential determination of probe and target DNA densities in one experiment, yielding electrode-specific information

The remainder of this thesis is organized in the following sections:

Section 2: Rapid-prototyping techniques are introduced in the context of general biosensor development, followed by a description of techniques used in the fabrication of DNA electrochemical sensors. Micro/nano-structuring techniques for DNA electrochemical are also discussed, with particular emphasis on the development of rapidly-prototyped, wrinkled gold film electrodes using pre-stressed polystyrene substrates for POC diagnostic development.

Section 3: Fundamental properties of DNA which make it useful for electrochemical and fluorescence detection are described, followed by a description of how DNA hybridization sensors are created, specifically the binding of probe DNA to a surface, the electrochemical phenomenon permitting detection of target DNA capture, and methods to enhance the detection signal.

Section 4: A more detailed description of the physicochemical processes which occur at the electrode-electrolyte interface is provided, as well as the instrumentation and the specific electrochemical techniques used in this thesis. The protocol for conducting DNA hybridization experiments is detailed here, along with results conducted with planar electrodes as an example.

Section 5: The fabrication procedure for rapidly-prototyped electrodes exhibiting micro/nano-scale wrinkling and porosity is detailed, followed by characterizations of surface topography and probe DNA density measured against variations in deposition time and probe molar fraction. These electrodes were then shown to be able to perform DNA hybridization detection using an electrocatalytic detection scheme.

Section 6: A characterization method for determining hybridization efficiency is presented which allows the sequential determination of probe and target DNA densities in the same experiment. This method employs solution-based methods to denature duplex DNA and to desorb surface-bound probe DNA from the electrode surface. Post-labelling of fluorophores allows for fluorescent quantitation of DNA, resulting in an electrode-specific measurement of hybridization efficiency without relying on pooled measurements.

Section 7: A summary of the major contributions of the thesis is given, followed by a description of future work to be conducted, and ending with a brief conclusion.

2.0 Rapid-Prototyping of Nano/Micro-Structured Electrodes

Rapid-prototyping is the use of fabrication techniques which allow the physical ideation of designs for the purposes of testing proof-of-concepts at reduced cost, material, and time. This chapters provides a description of the relevance of rapid-prototyping for biosensor development, the various prototyping techniques used in this domain, and the use of these techniques in the development of micro/nano-structured electrodes for DNA electrochemical sensing.

2.1 Rapid-Prototyping of Biosensors and POC Devices

Rapid-prototyping has benefitted greatly from the utility of polymer materials, 3D-printing, and paper as a less costly substrate material for biosensor development.

Polymers are less expensive than glass or semiconducting materials and the techniques associated with polymer fabrication (such as injection molding, embossing, and casting) are less expensive and typically do not require the use of hazardous chemicals. Whitesides et. al revolutionized the prototyping of microfluidic devices by demonstrating the ability to create microscale features within polydimethylsiloxane (PDMS) which makes it possible for the full design, fabrication, and testing phases to be completed with short turnaround times [27]. Since then, prototyping with polymeric materials has been a mainstay in microfluidics, with a plethora of polymers in use [28]. Conductive polymers have also been used to perform DNA electrochemical detection [29].

The 21st century has seen a dramatic increase in the popularity of 3D-printing as a prototyping tool. This fabrication technique gives researchers the ability to design prototypes in CAD programs and “print” these designs by an additive process of layering polymers to create physical designs in short turnaround times. The form-factor of these printers and cost effectiveness makes 3D printing an attractive option for prototyping. Presently, there exists several technologies which are classified as 3D-printing, including: stereolithography, digital micro-mirror device-based projection printing, two-photon-polymerisation, fused deposition modelling, inkjet, and bio-printing [30]. Using 3D-printing technology, groups have created assay platforms [31][32], microfluidic components and structures [33][34][35][36], and devices with integrated electrochemical sensors for the detection of biologically-relevant molecules [37].

The popularity of 3D-printing is still seeing an increase in popularity for biological applications [30] as it continues to meet the resolution and throughput requirements which may make it a competitor to traditional fabrication techniques, especially in the area microfluidics [38].

Paper, due to its ubiquity, affordability, and bio-inertness has especially been attractive for biosensor and POC device development, with concerted efforts to producing diagnostic assays for the developing world [39]. Because of its compatibility with other rapid-prototyping techniques, such as inkjet, wax, and screen-printing [40], a wide variety of paper-based assays have been demonstrated. Paper has also found usefulness as assembly components for microfluidic devices [41].

2.2 Rapid-Prototyping/Fabrication of Electrochemical Sensors

For rapid-prototyping of electrochemical sensors, two fabrication techniques have been popular: screen-printing and ink-jet printing.

2.2.1 Screen-Printing

Screen-printing is a thick-film (micrometer thick) material deposition technique which allows the layering of conductive (typically carbon-based) and non-conductive pastes to create sensor designs on a wide variety of substrates. Conductive ink is spread across a thin mesh screen with a mask on the underside, allowing ink to only pass through the mesh through open areas of the mask and onto the substrate. Commercially available inks typically contain additives to increase binding to substrates, such as mineral binders or insulating polymers, but hinder electron-transfer kinetics [42]. Also, the exact composition of inks is typically proprietary information, which limits the exact understanding of how exact compositional variation between inks affect electrochemical detection performance [43].

Several techniques have been employed to overcome this limitation. One widely used method is the addition of materials to the ink prior to printing. For example, Ren et. al [44] doped graphite ink with polyaniline nanotubes and ionic liquid and were able to perform DNA detection with a limit of 80 attomolar. Manganese oxide nanoparticles were mixed with carbon paste for the creation of disposable SPE nitric ion and ascorbic acid sensors [45]. Choudhury et. al [46] created non-enzymatic glucose sensors with copper (II) oxide-modified inks.

Although the addition of materials into inks can enhance electron transfer rates, properties of the ink which make it amenable for screen-printing, such as rheology and drying time, may be adversely affected [47]. To surmount this obstacle, researchers have explored different post-printing treatment strategies. Electrochemical potential cycling, also known as pre-activation, of carbon SPEs was conducted by Su et. al [48] who noticed that the charge transfer resistance and double-layer capacitance of the electrode decreased owing to surface nanostructuring. Wei et. al [49] performed a two-step treatment involving submersion of SPEs in 3M NaOH and subsequent pre-anodization in NaOH, which was shown to enhance heterogeneous electron transfer rates by approximately 70x.

2.2.2 Ink-Jet Printing

Ink-jet printers are found in two varieties – either as a continuous inking system or a drop-on-demand system (DOD) [50]. Continuous ink systems are the older of the two and utilize electrodes to selectively charge ink droplets which can then be deflected onto the printed surface to reproduce an image. The more popularly used variety is the DOD system which only ejects ink when necessary, permitting the printing of both conductive and non-conductive materials at pico-liter amounts. Two main types of DOD ink-jet printing exist: thermal and piezoelectric [51]. In thermal printing, a current pulse heats up a resistive element up to 200 degree Celsius which causes ink vapor bubbles to form. This causes a pressure pulse which ejects ink from the nozzle [52]. In piezoelectric printing, a voltage signal modulates the deformation of a piezoelectric element which pressurizes the ink and ejects droplets from the nozzle [51], allowing materials to be printed without heating.

By adding conductive materials to the ink, electrodes for electrochemical sensors can be printed. A three-electrode electrochemical system was printed on a surface-treated PDMS substrate which allowed adhesion of inkjet-printed silver nanoparticles [53] to create an integrated lab-on-a-chip (LOC) system for glucose detection. A three electrode system was also successively printed on paper by da Costa et. al [54] by ink-jet printing carbon nanotubes (CNTs) and hydrophobic layers of mineral oil for the electrochemical detection of dopamine and iron ions.

2.3 Nano-Structures for DNA Electrochemical Sensors

The pursuit of lower detection limits and sensitivity have led researchers to adopt novel materials and fabrication techniques which enable the creation of both micro and nanoscale features onto the electrode surface. Features in these length scales allow greater immobilization of bio-recognition molecules due to an increase in surface area, as well as enhanced target capture kinetics due to the morphology and size-scale of these features. Decreased feature sizes also allows an overall reduction in sensor footprint and sample volumes consumed for assays, which is a benefit for integration with microfluidic components and for achieving the requirements imposed by POC devices.

2.3.1 Nanomaterials

A wide host of nanomaterials have been employed for DNA electrochemical sensing which typically find usage as materials incorporated into the bulk electrode material, act as electrodes themselves, or facilitate detection by attaching to the DNA recognition layer directly.

2.3.1.1 Noble Metal Structures

Metallic structures are used in a multitude of strategies for enhancement to electrochemical DNA sensors owing to high surface area-to-volume ratios. Gold nanowires were used by Gasparac et. al [55] as an electrode scaffold for detection of attomole amounts of DNA. DNA detection using metal oxide nanowires deposited by chemical vapor deposition on graphite electrodes was performed by Mathur et. al [56].

Metallic and semi-conductor nanoparticles are commonly used as well. Cadmium sulfide, zinc sulfide, and tin sulfide quantum dot nanoparticles attached to surface immobilized DNA probes were used by Hansen et. al [57] to perform DNA detection at fM concentrations. Similarly, Park et. al [58] employed gold nanoparticle-labelled DNA to detect conductivity changes upon target DNA capture and were able to perform fM detection. Authier et. al [59] employed electrochemical detection of oxidative-released captured Au-NP modified target DNA on SPEs for pM detection limits.

2.3.1.2 Carbon-Containing Structures

Among the most employed nanomaterial used are carbon nanotubes. Apart from the nanoscale feature sizes, carbon nanotubes benefit highly from enhanced electronic conduction and mechanical abilities. Single-wall carbon nanotubes (SWCNTs) are single cylindrical graphite sheets with dimensions of 1-2 nm, while multi-wall carbon nanotubes (MWCNTs) are composed of SWCNTs with different radii arranged in a homocentric manner [60]. Li et. al [61] performed detection using MWCNTs embedded in silicon dioxide for detection of attomoles of DNA. Li et. al [60] used chitosan-CNT films on graphite electrodes for the detection in the pM range of DNA. Bonanni et. al [62] mixed carboxyl-modified MWCNTs to SPEs for the detection of 72 pmol of DNA.

Another carbon-based nanomaterial often used is graphene, which exhibits highly efficient electron conduction owing to the in-plane sp^2-hybridized bonds of the carbon sheets [63]. Akhavan et. al [63] created reduced graphene nanowalls by electrophoretic deposition followed by reduction in hydrazine for the detection of single-base mismatches, as well as ssDNA and dsDNA on a graphite electrode. The detection limit of these nanowalls for dsDNA was 9.4 zM. Label-free detection of methicillin-resistant staphylococcus aureus DNA was performed by Wang et. al [64] using reduced graphene oxide attached to indium tin oxide (ITO) electrodes using (3-aminopropyl)triethoxysilane (APTES) as a molecular linker. The limit of detection was 100 fM.

2.3.2 Polymers

Conductive polymeric materials have also been used as nanomaterials for DNA electrochemical sensing. These materials are often combined with other nanomaterials to form nanocomposites for electrochemical DNA sensing.

Polyaniline (PAN) is a conductive polymer which has several advantages over carbon-nanotube and Au-NP nanomaterials, including: low-temperature synthesis, tunable conductivity (although PAN has poorer conductivity than carbon-nanotube materials), and is purification-free [65]. Zhu et. al [66] performed electrochemical detection of polyaniline nanowire-modified carbon electrodes for pM DNA detection. Formation of PAN nanotube arrays by Chang et. al [65] allowed the improvement of polyaniline's poor conductivity, allowing a limit of detection of 1

fM of dsDNA and 37.59 fM of single-base mismatched DNA. An alternative method to improve PAN conductivity was demonstrated by Bo et. al [67] by creating oxidized graphene/polyaniline nanowire-modified glassy carbon electrodes which exhibited a limit of dsDNA detection of 0.325 pM.

A Poly-3,4-ethylenedioxythiophene (PEDOT)-AuNP composites were created by Spain et. al [68] to create a sand-which assay for the electrochemical detection of a sequence related to Staphylococcus aureus.

Polypyrrole (PPy) is another conductive polymer which is typically used as a link between different nanostructures to form nanocomposites. Liu et. al [69] created a MWNT/polypyrrole/Au-NP nanocomposite which was shown to have a limit of detection of 430 fM for a gene sequence related to avian influenza virus (AIV) H5N1. A PPy/PEDOT/Ag nanotube-nanocomposite film was created by Radhakrishnan et. al [70] for the detection of ssDNA with a detection limit of 5.4 fM.

2.3.3 Electrodeposition

Electrodeposition is the controlled addition of electrode material (typically palladium or gold) from the solution-phase by applying a potential or current waveform for direct control of the reduction-oxidation reactions of metal ions in solution [71]. Tunability of deposited feature sizes and morphology is permitted by adjusting the deposition conditions, such as the deposition duration, the concentration of metal ions in solution, and the concentration and composition of supporting electrolyte [72]. This allows the creation of nanostructures of a plethora of morphologies, including dendritic [73][74], spherical [75], pyramidal [76], rod-like [77], pin-like [78], and flower-like [79] structures.

Electrodeposited structures have been demonstrated for performing DNA detection at low target concentrations. Soleymani et. al [72] electrodeposited nanostructures of varying length-scales and morphology by varying the plating potential, plating duration, and concentrations of hydrogen chloride and perchloric acid supporting electrolytes with palladium chloride deposition onto silicon dioxide microelectrodes. Deposition of nanostructures in the 20-50 nm length-scale allowed a limit of nucleic acid detection of 10 aM. This same group [80] created similar structures for the detection of mRNA from E.coli extracts, concluding that nanostructured

length-scales between 1-30 nm with 100 µM footprint size were the most efficient for biomolecular detection. In like manner, Vasilyeva et. al [81] substituted palladium for gold electrodeposition to create nanostructures with a 100 µM footprint exhibiting substructures extending many µm into solution. This sensing platform was able to electrochemically detect mRNA from 10 electrically lysed leukemia cells using a modified PNA probe.

Li et. al electrodeposited dendritic gold nanostructures from a solution of gold chloride and sulfuric acid onto planar gold electrodes, showing tunability of the size and reach of dendritic structures with deposition duration. This group was able to achieve a limit of DNA detection of 1 fM.

2.3.4 Porosity

Porous electrodes have been fabricated from a variety of materials, including: alumina [82], silicon [82][83], metal-oxide nanotubes [82], carbon nanotubes [84], and polymers [85]. Additional details about porous nanostructured electrodes will be given in section 5.0, which describes the creation of all-solution processed electrodes for electrochemical DNA hybridization detection.

2.4 Wrinkled Nano/Micro-Structured electrodes

As mentioned, micro/nano-structuring of the electrode surfaces provide an enhancement in DNA detection capability by lowering the detection limits achievable. Rapid-prototyping of electrodes with tunable micro/nano-structured surfaces remain a challenge. Screen-printing necessitates ensuring that micro/nano-structures mixed with the conductive pastes do not interfere with the printing properties of the ink, which is complicated by manufacturers withholding the formulation of their inks. Ink-jet printing of micro/nano-structures also requires knowledge of the interaction between printed materials and the substrate to allow stable adhesion. Post-processing of electrodes is also often required to either deposit micro/nano-structures to the electrode surface or provide further modifications to the surface.

In light of these challenges, our group has developed a rapid-fabrication technique to create electrodes demonstrating tunable micro/nano-scale features. These features result from the actual fabrication process and as such, do not require post-processing or deposition of micro/nano-scale materials after fabrication. The ensuing portion of this chapter provides a background of research and theory relating to the formation of micro/nano-scale structures by electrodes, and a description of the progress our group has made using these electrodes for the research and development of POC diagnostic devices.

2.4.1 Background

The earliest encounter of wrinkling phenomenon was made by Martin et. al [86] of vacuum deposited gold and indium films onto PDMS. Bowden et. al [87] further examined this wrinkling behaviour on thin gold films evaporated on top of a seed layer of titanium or chromium resting on PDMS. A slight contraction of the thermally-expanded PDMS caused buckling of the thin film which formed relief structures to dissipate the compressive stress. The wavelengths produced were between 20-50 μm.

Mathematical modelling of this wrinkling behaviour was performed by Volynskii et. al [88] by examination of wrinkled-gold and platinum films coated onto rubber and poly(ethylene terephthalate) (PET). They estimated the dominant wavelength for wrinkles produced by uniaxial stress on a thin film resting on an elastomer as related to the film thickness (h), Young's Modulus (E), and Poisson's Ratio (v) of the film (f) and substrate (s):

$$\lambda = 2\pi h\left[\frac{(1-\nu_s{}^2)E_f}{3(1-\nu_f{}^2)E_s}\right]^{1/3}$$

Equation 1. Wavelength of wrinkles generated by a uni-axial stress [88]

Huang et. al [89] and Jiang et. al [90] were the first to quantitatively evaluate the amplitude of wrinkles formed by a uni-axial stress, which depends upon the film thickness (h), the buckling (ε) strain, and critical buckling strain (ε_c) which must be surpassed to allow wrinkling.

$$A = h\left[\frac{\varepsilon}{\varepsilon_c} - 1\right]^{1/2}$$

Equation 2. Amplitude of wrinkles generated by a uni-axial stress [89][90]

In the case where bi-axial/isotropic stress is applied to a thin film on an elastomer, more complex wrinkling occurs with multiple directionality that coalesce [91]. These waves are characterized by a distance (ξ) at which coherence is retained which is dependent on the parameters previously described ($\xi \propto h(E_f/E_s)^{2/3}$) [92]

2.4.1.1 Wrinkling of Thin Films on Polystyrene

There exists a class of polymers which exhibit a programmability in their shape. These shape-memory polymers are moldable into a temporary shape which is retained upon cooling. Heating past a specific transition temperature allows the shape to revert back to its original shape [93]. Pre-stressed polystyrene (PS) is one example of these shape-memory polymers, which can be commercially purchased as a craft material called “Shrinky-Dinks”.

Fu et. al [92] first demonstrated the ability to create tunable metal nanowrinkles on pre-stressed PS (PSPS) sheets. As a temporary shape, PSPS is in a thin planar sheet; however, heating past the glass-transition temperature of PS (95 degree Celsius) but below its melting temperature (240 degree Celsius) causes the PS to revert back to its original shape [94], which causes a bi-axial reduction of less than 50% in length and width dimensions. By depositing a 10 nm layer of gold onto the PSPS sheets and heating past the glass-transition temperature, the size reduction of PS caused the stiffer gold metal layer to buckle and form wave-like shapes with wavelengths that could be tuned between 200 nm to 1 μm [94].

Chen et. al [95] used this inherent property of PSPS to create microfluidic structures. This group used sharp-tipped objects such as syringe tips and razor blades to scribe channels into the pre-stressed sheets, achieving channels of 8 μm thinness and 50-600 μm depth after shrinking past the glass-transition temperature. Using this technique, a vortex mixer could be created.

2.4.2 Wrinkled Sputtered Polystyrene Electrodes

Our group has further developed the PS-induced surface wrinkling of metal films for the creation of bench-top fabricated electrodes. Gabardo et. al [96] combined a xurographic process of cutting pre-defined designs into one-sided adhesive vinyl with a craft cutter which served as a mask for PSPS sheets. Following deposition of gold onto the masked sheets, removal of the mask, and subsequent heating past the glass transition temperature to 160 degree Celsius, wrinkled structures with a defined geometry could be created, demonstrating a reduction to 38% of original transverse dimensions and an increase in thickness to 700% of the original thickness. Electrochemical measurements of the surface area yielded up to a 650% increase in the surface area compared to a strictly planar surface. Varying the sputtered thickness of the gold film allowed nanometer-scale (at 20 nm thickness) to micro-meter scale (at 200 nm) wrinkle thicknesses. These electrodes also demonstrated favorable characteristics for use as working surfaces for electrochemical analysis.

Following this work, Woo et. al [97] used the same fabrication procedure to demonstrate the suitability of these electrodes for performing electrochemical DNA detection. In comparison to planar electrodes, it was demonstrated that these wrinkled, sputtered polystyrene electrodes (WSPEs) exhibited a greater capacity for the attachment of probe DNA by thiol-Au linkage, owing to the surface area enhancement attributed to surface wrinkling. However, this increase in probe density for WSPEs did not match the same enhancement seen for surface areas compared to planar surfaces. It was hypothesized that cavernous regions in between the wrinkled structures prohibited access and subsequent binding of 20mer DNA probes. Electrocatalytic detection of complementary target DNA was achieved which yielded a significant difference to current signals generated from the detection of non-complementary targets.

Interdigitated electrodes created from the same fabrication process have also been created to address the high voltage requirements for bacterial cell lysis in POC devices [98]. WSPEs were

shown to have increased lysis efficiency compared to planar electrodes for voltages less than a 12 V battery, and an even higher efficiency for WSPEs electrodeposited with gold nanostructures. These electrodeposited WSPEs were able to achieve 95% lysis efficiency of *E. coli* cells at 4 V, making these electrodes suitable candidates for low-voltage lysis for portable systems. Wrinkled electromagnetic devices have also been fabricated to demonstrate the low-voltage capture of magnetic particles [99].

One major drawback with the fabrication of these wrinkled, polystyrene-electrodes is the reliance on vacuum-sputtering of metallic layers onto the PS substrate. This method deposits metal non-specifically onto the substrate and as such, contributes to material wasted. An attractive improvement to the fabrication procedure would be to eliminate the use of sputtering in favor of a more specific deposition technique. Section 5.0 will present a replacement technique, allowing more-specific deposition of metal to occur from processing steps conducted only in solution. As will be discussed, this new technique will also create porosity onto the surface film, in addition to the wrinkled structures expected.

2.4.3 Fabrication of Wrinkled, Polystyrene-Sputtered Electrodes

A more detailed description of the fabrication procedure for WSPEs is given here, as these electrodes will be used for further characterization in section 6.0. The fabrication scheme is illustrated in Figure 2.1 below.

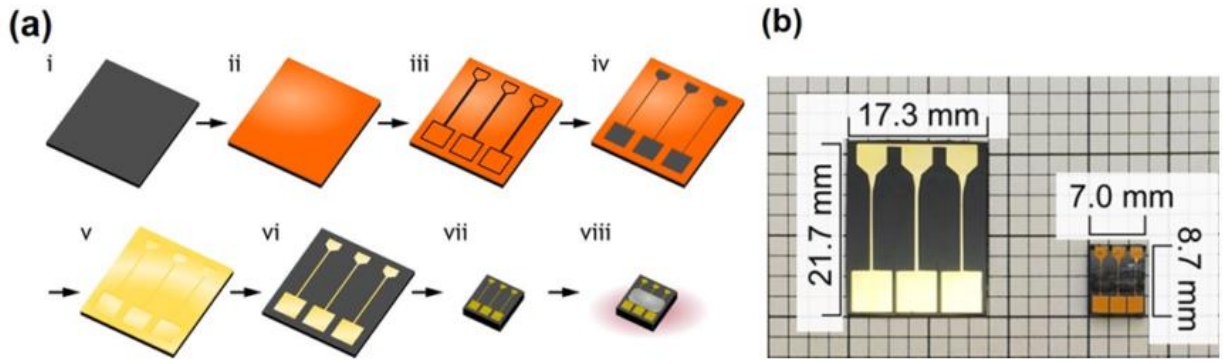

Figure 2.1 Fabrication process of WSPEs. (a) Process flow diagram of the polystyrene (PS) substrate during fabrication, starting with a (i) pre-stressed PS (PSPS) sheet, (ii) masking with a one-sided adhesive vinyl and (iii) subsequent xurography of the electrode design, (iv) removal of cut vinyl, (v) sputtering of gold film, (vi) removal of mask, (vii) heat shrinking, and (viii) gluing to separate contact pad and electrode surface. (b) Images comparing the length and width dimensions of electrodes before and after shrinking [97].

Briefly, mask designs of the devices were created in Adobe Illustrator and cut into vinyl films using a craft cutter (Robo Pro CE5000-40-CRP) (Graphtec America Inc., Irvine, California) using a 0.9 mm blade (CB09UA) with force, quality, and speed values of 10, 1, and 1 respectively. These vinyl masks were then adhered to 2-propanol and water rinsed pre-stressed black polystyrene sheets (Graphix Shrink Film, Graphix, Maple Heights, Ohio). A variable layer of gold was then deposited by DC sputtering (Torr Compact Research Coater CRC-600 manual planar magnetron sputtering system (New Windsor, New York) in an argon atmosphere at a deposition rate of 0.9 Å/s. Following removal of the vinyl mask, sputtered polystyrene devices were heated to 160°C on aluminum boats for 3 minutes in a 3511FSQ (664) Isotemp gravity convection oven (Fisher Scientific, Ottawa, Ontario) which caused the devices to shrink due to the phenomenon previously described. Electrodes were then glued (Elmer's Model and Hobby Cement, Elmer's Products, Inc, Westerville, OH) to separate the connectors between the electrode working surface and the contact pad for electrical connection to the potentiostat. The glue was allowed to dry in room temperature, followed by a final washing in IPA and DI water.

2.5 Conclusion

This section provided a brief description of rapid-prototyping for biosensor development, including a survey of major techniques that have been used to shorten the turnaround time and decrease costs associated with the prototyping stage of electrochemical sensor development. This was followed by a description of techniques and materials used for creating micro/nano-scale structures for DNA electrochemical detection.

To address the challenges associated with the rapid-prototyping of electrodes with tunable micro/nano-scale features, our group has developed rapidly-prototyping wrinkled, polystyrene electrodes which show promise in the development of POC diagnostic devices. One drawback to the fabrication of these electrodes is the reliance on vacuum-based sputtering of metallic films onto the polystyrene substrate. An improvement on the fabrication process which replaces sputtering and creates additional micro/nano-scale features in the form pores is presented in section 5.0.

3.0 Theory of Electrochemical DNA Biosensors

This chapters introduces the basic properties of DNA which make it amenable to electrochemical detection (section 3.1), followed by a description of how DNA interfaces with a solid electrode to create a biosensor and how reduction-oxidation reactions permit the discrimination of target DNA capture events (section 3.2). Relevant methods to generate and enhance redox signals are also described (section 3.3).

3.1 Properties of Deoxyribonucleic Acid (DNA)

3.1.1 Composition

Watson and Crick, in their historical 1953 Nature publication, "Molecular Structure of Nucleic Acids: A structure for Deoxyribose Nucleic Acid"[100] proposed a double-helical structure of DNA which is still valid today. In this model (presented in Figure 3.1), DNA is composed of subunits known as nucleotides, which include a nitrogenous base, a phosphate group, and a deoxyribose sugar of 4 varieties: purines adenosine (A) and thymine (T), and pyrimidines cytosine (C) and guanine (G). In the single-stranded DNA (ssDNA) structure, nucleotides attach in a linear fashion by the phosphate group of one nucleotide to the hydroxyl (OH) group of another (phosphodiester bonds) to create a polymer with ends designated as either the 5' or 3' end.

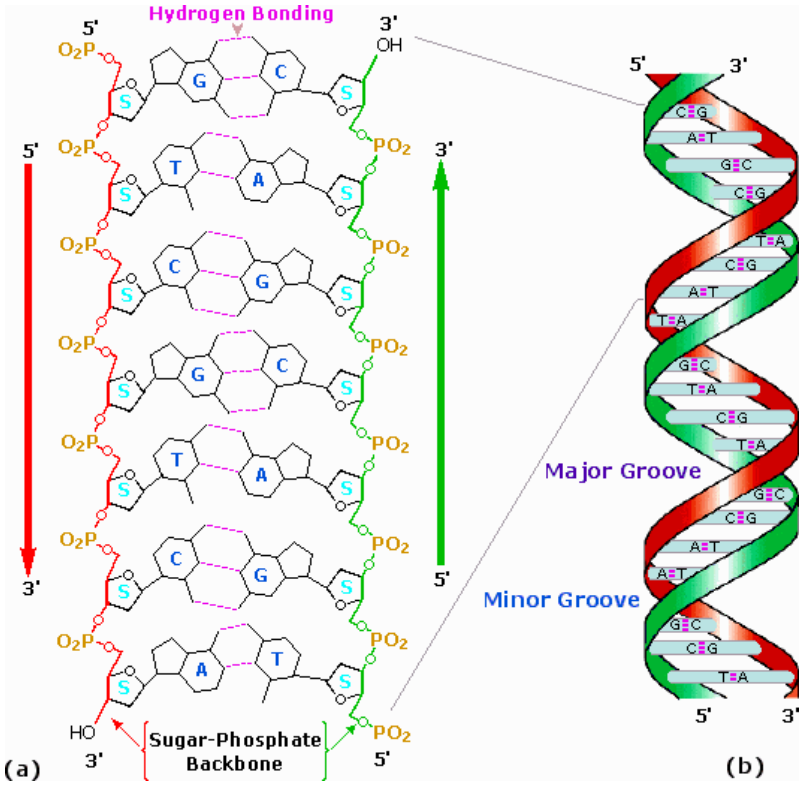

Figure 3.1 (a) The molecular composition of duplex DNA showing the sugar-phosphate backbone and the nitrogenous bases which form hydrogen bonds to adjacent bases. (b) The helical structure indicating repetitive major and minor grooves throughout the structure [www.boundless.com].

Double-stranded DNA (dsDNA) is formed when two ssDNA combine, or hybridize, due to the complementarity of their bases, with adenine forming two hydrogen bonds with thymine, and cytosine forming 3 hydrogen bonds with guanine. Due to the energetic favorability of the hydrogen bonds in the mentioned pairings, other combination of base pairings are unfavorable. The phosphate group of the backbone imparts a negative charge to each nucleotide, such that dsDNA contains twice the negative charge as its individual single-strands. This inherent charge is fundamental to the operation of DNA gel electrophoresis [101].

3.1.2 DNA Melting

DNA in the duplex state can be separated to yield individual ssDNA. Hydrogen bonds between base pairs in dsDNA can be broken and the temperature at which half of a given amount of dsDNA separates is known as the melting temperature (T_m). The temperature scales with the

number of base pairs and also increases with the number of GC base pairs due to the greater number of hydrogen bonds than in AT pairing [101]. Several methods, apart from heating, exist which can also cause dsDNA to unravel to ssDNA. These methods can be broadly separated into chemical methods (ex. formamide, and urea) which compete with the hydrogen bonds between bases, and alkaline agents (ex. NaOH) which causes an increase in solution pH disrupting the favorability of hydrogen bonds, and physical method (ex. sonication, bead milling, and heating) which causes physical disruption to the molecular structure [102]. If the denaturation conditions are removed, formation of dsDNA can reoccur. Denaturation of DNA by using NaOH will be used to separate hybridized probe and target DNA, as will be discussed in section 6.0.

3.1.3 DNA-Binding Fluorophores

The fluorescence imaging of nucleic acids is a technique which permits the quantitative and qualitative study of nucleic acids which has proven especially useful for in vivo studies of complex biological systems [103]. This technique is used predominantly in the biological sciences and biotechnology, but has extended into the areas of medical diagnostics, DNA sequencing, forensics, and genetic analysis [104].

In section 1.0, fluorescence detection was introduced as a common detection technique for POC nucleic acid platforms. Target nucleic acids must first be labelled with a molecular tag or probe capable of fluorescing. To achieve this, fluorescent molecules (fluorophores) may be covalently attached to the structure of probe DNA itself, usually during the synthesis of these oligonucleotides. For example, this work utilizes the fluorescent molecule fluorescein which has excitation and emission peaks at 494 nm and 521 nm respectively and is covalently attached to probe DNA.

Fluorophores may also be introduced into the DNA environment as a dye which then interacts and binds with the structure of DNA in differing modes as illustrated in Figure 3.2. Intercalating fluorophores (ex. ethidium bromide) bind to the duplex structure by inserting between base pairs, groove binders attach to the DNA on either the major or minor grooves, and external binders interact with the phosphate-backbone.

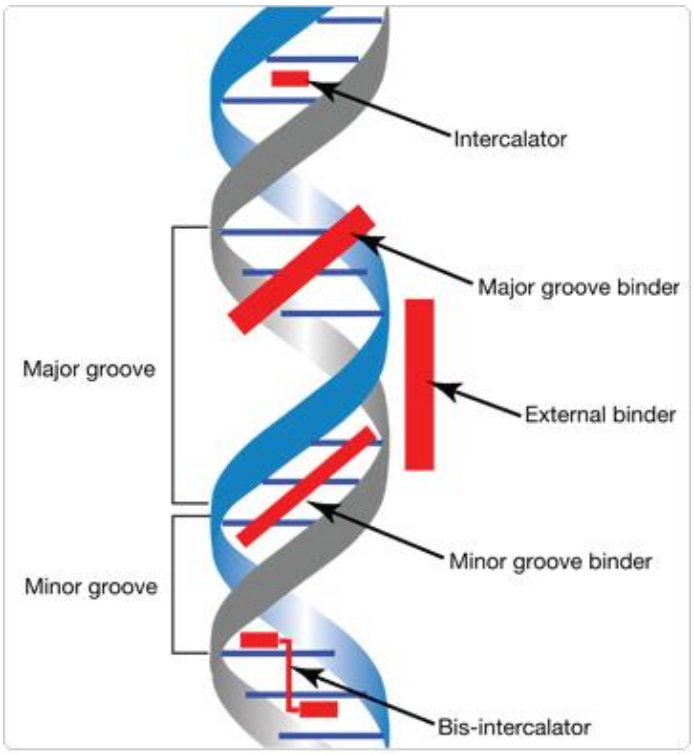

Figure 3.2 Differing methods of which fluorophores interact with the nucleic acid structure to permit fluorescence detection [105].

In addition to fluorophore-modified probe DNA, this thesis also uses a fluorescent dye which allows fluorescent quantitation of DNA without covalent modifications to its structure (as will be discussed in section 6.0)

3.1.4 Charge Transport

The structure of DNA, as illustrated in Figure 3., contain 'lateral' base-pairing of heterocyclic purine and pyrimidines held together by hydrogen bonding. These aromatic molecules also allow vertical interaction between base-pairs through non-covalent interaction of π-bonds. This phenomenon is called π-stacking and proliferates throughout the entire nucleic acid structure, conferring the structure with electron mobility/charge transport ability [106]. As such, charge is able to travel along the length of the DNA by movement through these overlapping π-bonds. Electron tunneling and hopping mechanisms have been proposed as methods of charge transport [107]. Studies with electron donor and acceptor (termed a doublet) intercalating molecules inserted into the DNA structure at various distances have been performed to measure the distance-dependent decay of electron transfer and was seen to persist at distances greater than

200 Å without significant decay [108]. The purines guanine and adenine are more easily oxidized (oxidation potentials of 1.3 V and 1.4 V vs. NHE respectively) than cytosine and thymine which are more easily reduced (reduction potential of -1.1 vs. NHE) [109]. Placing an ATA bulge causes reduced electron transfer interrogated by NMR [110]. Single-base mismatches in the duplex structure causes differences in long-range oxidative guanine damage [111]. Sequence specific flexibility in DNA has been shown to cause dynamical motion and resulting in charge transport inhibition [112].

Of interest for this thesis are the studies of electron conduction in DNA by the interrogation of DNA-modified surfaces. These studies provide an explanation of the foundational mechanisms, as shall be discussed in the following sections, for DNA electrochemical sensing. Redox-active molecules such as methylene blue (intercalator), ruthenium hexamine chloride ($Ru(NH_3)_5Cl^{2+}$, groove-binder), and ferrocyanide ($Fe(CN_6)^{4-}$, external-binder) have been used to interrogate gold-bound DNA for the investigation of single-base pair mismatches by detecting changes in charge transduction [113]. As illustrated in Figure 3.3, these redox molecules interact with the DNA structure in the same manner as fluorescent molecules (Figure 3.2)

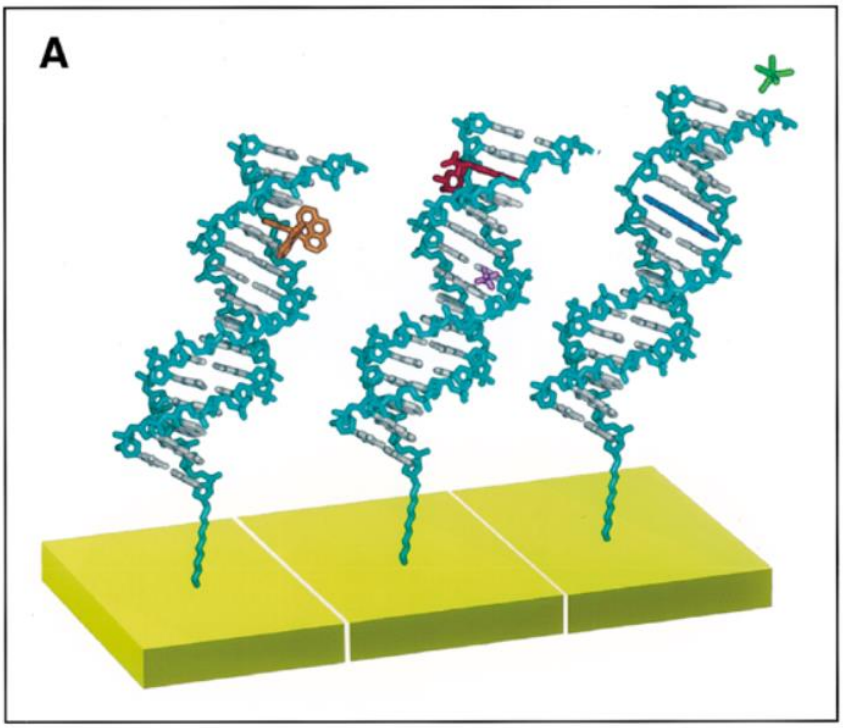

Figure 3.3 The intercalation of methylene blue (blue), groove-binding of ruthenium hexamine chloride ($Ru(NH_3)_5Cl^{2+}$, purple), and electrostatic attraction of ferrocyanide ($Fe(CN_6)^{4-}$) to the DNA duplex structure, bound to a surface, allowing electrochemical studies of DNA-mediated charge transfer [113].

Since these redox molecules, such as methylene blue, bind in greater amount to dsDNA than ssDNA, the change in charge transduction upon binding of redox molecules indicates the presence of dsDNA. It is this mechanism which allows the electrochemical detection of hybridization events of probe DNA bound to a surface.

3.2 Principles of Hybridization Biosensors

As discussed previously, the π-stacked bases of DNA permit charge transfer to occur along its structure. Redox molecules which bind either preferentially or in greater amounts to dsDNA than ssDNA can be used to discriminate between the two. A discussion on how DNA is attached to a solid surface is now given, followed by a description of electroanalytical detection methods commonly used to interrogate these DNA-bound surfaces.

3.2.1 DNA Immobilization

Probe DNA are typically bound to a solid surface which introduces a recognition layer to the surface and confers selectivity for binding complementary target DNA.

A passive method which has been exploited to create a surface assembled monolayer (SAM) of DNA structures is the chemisorption of thiol (-SH) groups to noble metals, such as gold [114]. DNA structures modified with thiol end-groups introduced to the gold surface in the solution-phase spontaneously attach by the aforementioned chemistry. The exact mechanism for this attachment has been contested. Several mechanisms have been reported for the attachment of thiol-groups to the surface of Au(111) and gold adatoms [115]. A basic two-step mechanism for Au-thiol monolayer formation has been proposed [116][117] and initiates with the fast attachment of –SH groups and formation of Au-S bond, followed by a slower arrangement of the attached alkyl groups to form stable layers from the maximization of van der Waals forces between groups (Figure 3.4)

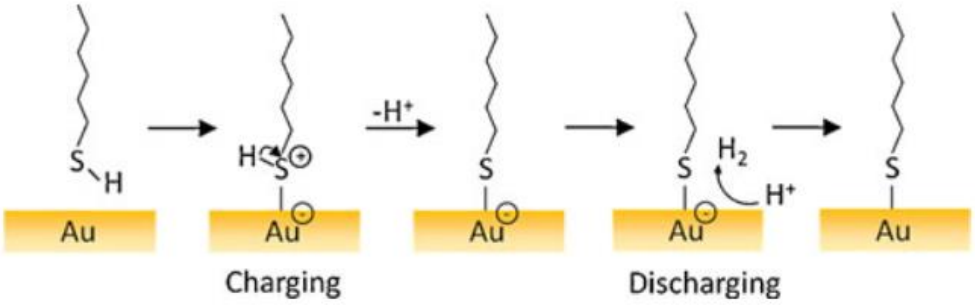

Figure 3.4 Mechanism for the surface-adsorption of thiol groups to Au [114].

It has been shown that the composition of the monolayer is affected not only by the concentration of thiols introduced into the solution but also by the deposition conditions such as solution pH, temperature, and surface structuring [114]. Stability of the monolayer is also modulated by the length of the attached alkyl group, with longer groups creating well-packed, ordered structures due to increased van der Waals forces, over shorter chain groups.

An additional modification to the SAM is often performed to increase monolayer stability and order. The introduction of shorter chain thiol groups, such as 6-mercapto-1-hexanol (MCH), after initial thiol-Au formation allows competitive binding to occur which serves to remove DNA which are non-specifically bound to the gold surface (ex. electrostatic interaction of bases to the surface) and to promote the vertical extension of alkyl chains [118]. SAMs prepared with the previously described methodology described initially create alkyl chains which lie at a 30 degree angle from the surface normal [119]. This backfill step ensures proper SAM alignment for target DNA hybridization.

This work use a 20-base synthetic probe oligonucleotide which is bound to a gold surface by gold-thiol chemistry, and a backfill of MCH is performed to properly align the monolayer.

3.2.2 Electroanalytical Detection

Many electroanalytical techniques have been explored for the transduction of charge transfer-induced signals from DNA hybridization events. These techniques can be broadly classified into potentiometric, conductometric, and amperometric techniques [120].

In potentiometry, the potential is measured as the result of an accumulation of ionic charge at the electrode surface. This techniques typically relies on the translation of hybridization events to the change in the ionic content of the local solution which is detected with ion-selective electrodes (ISEs) [121]. For example, Numnuam et. al [122] performed a potentiometric analysis of DNA hybridization using a sandwich-based assay starting with a probe monolayer, detecting a target strand, and hybridizing a reporter strand with a CdS tag to the captured target. Dissolving with hydrogen peroxide creates a dilute electrolyte solution of Cd^{2+} which is then detected by a Cd^{2+}-selective electrode. Wu et. al [123] performed as similar sandwich hybridization procedure by Ag^{+}-ISE detection of the enzymatic depletion of silver ions by streptavidin-alkaline phosphatase bound to biotinylated reporter strands. Shishkanova et. al [124] employed cholesterol-

oligo$(dA)_{15}$ modified polyvinyl chloride (PVC) membranes which detected the changes in the ionic distribution in the intermolecular regions of hybridized DNA.

In conductometry, the variable of detection is the conductivity of the solution or the medium. A related method is electrical impedance spectroscopy (EIS), which is a measure of the impedance to charge transfer (faradaic impedance spectroscopy) from redox reactions due to changes in the monolayer composition. For example, Kafka et. al [125] performed hybridization detection of 18mer DNA at a gold electrode, interrogating the surface with ferri/ferrocyanide to detect changes to charge-transfer resistance following ssDNA hybridization.

Changes in impedance due to changes in double-layer charging currents (non-faradaic impedance spectroscopy) can also be used as a detection scheme. For example, aM detection of DNA in a µL droplet of water was performed by Ebrahimi et. al [126] by monitoring the change in solution impedance as the droplet progresses in evaporation. The shrinking volume of water increases the DNA concentration, which is detected as a decrease in solution impedance. Ma et. al [127] performed EIS detection of DNA hybridization at a gold surface, employing an enzymatic amplification scheme which enables the formation of insoluble product at the surface after hybridization. This soluble product further blocks the surface for faradaic charge transfer, increasing the detected impedance.

Amperometric sensors apply a potential perturbation to the SAM and record the resulting current flow due to redox reactions of electroactive species. These sensors are further classified in terms of the characteristic of the input potential signal. In amperometry, the current is recorded as a result of a constant potential waveform. For example, Zhang et. al [26] was able to detect fM amounts of target DNA in a 10 µL droplet using a sandwich assay which detects changes in hydrogen peroxide electro-reduction current when the electrode is held at a potential of 0.12 V (vs. Ag/AgCl). In voltammetry, the current is recorded from the application of a time varying potential waveform. This work uses two techniques in this category: cyclic voltammetry (CV) and differential pulse voltammetry (DPV). A more thorough treatment on the theoretical background and explanation of these techniques will be given in the following chapter.

3.3 Redox Signal Generation/Enhancement

In the discussion given in section 3.1.4 on the charge-transport mechanisms of DNA, examples of experiments were given which described the use of redox-active molecules which interact with the DNA structure by several modes (Figure 3..3), including intercalation, groove-binding, and by electrostatic interaction with the polyanionic DNA backbone. Because these interactions are found in greater amount when DNA is in the duplex state, these mechanisms work well for hybridization detection.

The sensitivity of electrochemical DNA sensors describes the amount of signal change that occurs with changes in the target concentration introduced to the sensor. The greater the sensitivity, the lower number of target DNA is required for a discernible signal change. To increase this sensitivity, several techniques have been employed as discussed below.

3.3.1 Electrocatalyis

One method to create a signal enhancement upon target hybridization to probe DNA is the use of an electrocatalytic detection scheme. A redox reporter molecule is oxidized/reduced to generate a faradaic current, whereupon another redox-active molecule replenishes the reporter back to the reduced/oxidized form [128]. This allows a cyclic generation of faradaic current to occur. For example, mutation detection of single-base mismatches and DNA base lesions was performed by methylene blue coupled to ferricyanide [128] as an electrocatalytic detection scheme. An electrocatalytic DNA detection scheme which couples RuHex and ferricyanide was used for the detection of bacterial pathogen Heliobacter pylori, as illustrated in Figure 3.5.

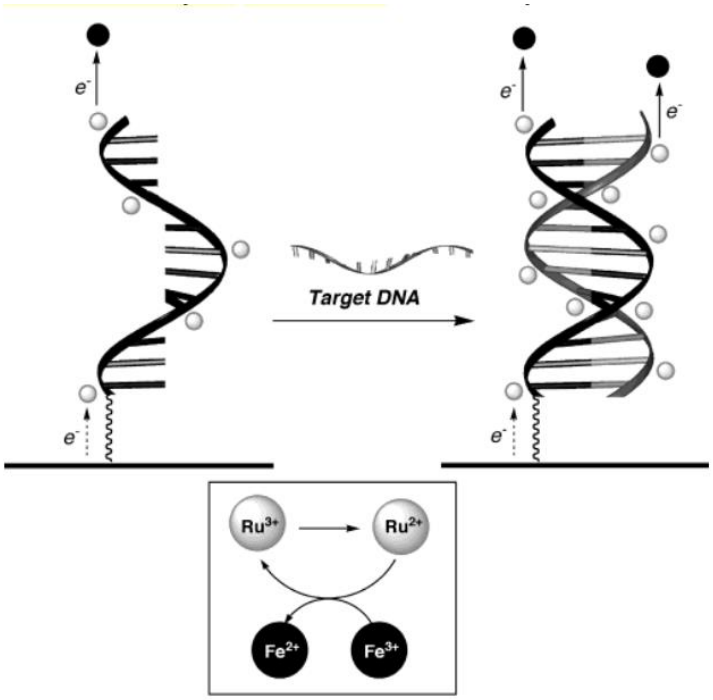

Figure 3.5 The electrocatalytic detection of DNA hybridization showing the interaction of RuHex with the DNA backbone in surface-bound ssDNA and in greater amounts with dsDNA and the oxidation of Ru^{2+} back to Ru^{3+} by Fe^{3+} for signal enhancement [129].

This work uses the same electrocatalytic detection scheme with the reduced form of RuHex replenished by ferricyanide back to the oxidized form. This detection scheme is an attractive detection technique as labelling of DNA is not required, reporter molecules (such as in sandwich assays) are not required, and low detection limits have been achievable.

3.3.2 DNA Amplification

DNA amplification was discussed as an important part of POC diagnostic platforms in section 1.0 to be able to create enough target copies for downstream detection. Well-developed amplification methods in molecular biology have been miniaturized for use in POC diagnostics. Among these methods is the widely used polymerase-chain reaction (PCR). Briefly, PCR is performed under a series of cyclic heating and cooling steps. These temperature changes allow duplex DNA to be unraveled allowing DNA polymerase and primers to attach to a region of interest. Once attached, copying of the DNA segment proceeds which results in another duplex structure. Repetition of these steps causes an exponential increase in copied strands over time.

Research has been conducted to overcome the high temperature requirements and additional processing resources for use in POC appropriate formats [130][131].

More attractive are the isothermal amplification strategies which do not require temperature cycling and is carried out at constant temperature [132]. Loop-mediated isothermal amplification (LAMP) [133][134], rolling cyclic amplification (RCA) [135], helicase-dependent amplification (HDA) [132] are strategies which have been demonstrated to work with DNA electrochemical sensing on the same sensor platform.

3.3.4 Surface Nanostructuring

As discussed in the previous chapter, nanostructuring is the effect of introducing nano-scale features onto the electrode. This structuring of the surface has two main effects: the increase of the surface area which directly increases the amount of probe DNA attached to the electrode, and modulation of the way in which DNA interact with probes at the three-dimensional surface. In comparison to strictly two-dimensional surfaces, an extra dimension allows for less steric hindrance and electrostatic repulsion between DNA.

3.4 Conclusion

This section described the relevant properties of DNA, including the natural affinity between complementary pairs and the ability of DNA to mediate charge transfer. Employing the passive Au-thiol bond allows the attachment of single-stranded probe DNA to create SAMs on electrode surfaces, which allow the interrogation of electro-active redox molecules to single-stranded and duplex structures. A short summary of electroanalytical techniques was then given, followed by a presentation of strategies used to increase the signals generated from electrochemical detection of hybridization events. The following chapter will provide a more detailed understanding of the electrochemical techniques used in this work.

4.0 Electrochemical Detection Techniques

This chapter provides a description of the physicochemical nature of the electrode-electrolyte interface which allows charge to cross between the solid-liquid interfaces and forms the necessary components for electroanalytical detection. A description of current generation is described in terms of the electrode-reaction kinetics (section 4.1). This is followed by a description of the instrumentation (section 4.2) and the analytical techniques – CV (section 4.3), DPV (section 4.4), and CC (section 4.5) – used in this work. Finally, the full DNA electrochemical detection protocol is described and demonstrated with planar gold electrodes (4.7).

4.1 Electrode Kinetics

At the electrode surface, the reductive/oxidative current out of/into the electrode is dictated by the Butler-Volmer equation [136], which describes the current as a function of the reduction and oxidation reaction kinetics:

$$i = i_o \left(\frac{c_o}{c_o{}^o} \right)^{1-\beta} \left(\frac{C_R}{C_R{}^o} \right)^{\beta} \left\{ \exp\left(\frac{(1-\beta)nF}{RT} \eta_s \right) - \exp\left(\frac{-\beta nF}{RT} \eta_s \right) \right\}$$

Equation 3. Butler-Volmer equation

where i_o is the exchange current density or equilibrium current density, c_o is the concentration of oxidized species at the surface of the electrode, $c_o{}^o$ is the concentration of oxidized species in the bulk solution, c_R is the concentration of reduced species at the electrode surface, $c_R{}^o$ is the concentration of reduced species in the bulk solution, β is the transfer coefficient, n is the number of electrons participating in the redox reaction, F is Faraday's constant, R is the gas constant, T is the temperature, and η_s is the surface overpotential ($\phi(t) - \phi^O$), where $\phi(t)$ is the applied potential and ϕ^O is the equilibrium overpotential.

4.2 Potentiostat and the 3-Electrode System

Electrochemical analytical techniques require the precise application of a potential waveform $\phi(t)$ and measurement of the cell potential difference (caused by the movement of charge across boundaries from chemical reactions) between an electrode (the working electrode) and its

solution environment. In fact, all electrodes within an electrochemical cell contain chemical reactions at their electrode/electrolyte interfaces [136].

In a 2-electrode system, the working electrode is complemented with an electrode whose cell potential is kept constant, since only the working electrode is to be investigated. This reference electrode is typically of an inert metal with constant composition, such that its half-cell potential is constant. A widely-used reference electrode is the silver-silver chloride electrode (Ag/AgCl/KCl, typically simplified in notation to Ag/AgCl) whose half-cell potential is +0.235 V (with 1 M KCl) with respect to the internationally recognized Standard Hydrogen Electrode (SHE) which is at 0 V [136]. All mention of potentials related to electrochemical analysis in this work will be implied to be relative to to the Ag/AgCl reference.

An application of a potential across working and reference electrodes in 2-electrode system causes an ohmic drop between the two electrodes due to finite solution resistance. In most techniques, a 3-electrode system, which includes an additional counter electrode, is used to minimize the effects of solution resistance on potential measurements. The potential waveform is now monitored between the working and reference electrode, which is placed in close proximity to the working electrode, and current travels from the working to the counter electrode. The modern potentiostat also contains a high reference electrode input impedance, minimizing the current which enters the reference electrode, subsequently maximizing current flow to the counter electrode. [136]

When a potential is applied to an electrochemical system, the current detected is a function of the concentration of reduction and oxidation species at the surface of the electrode. Considering a simple one electron transfer relationship between species A and B:

$$A + e^{-} \Leftrightarrow B$$

The proportion of oxidized and reduced species is defined by the Nernst Equation [136] which relates these concentrations at the surface to the applied potential, assuming rapid electron transfer:

$$E = E^{o\prime} + \frac{0.0591}{n} \log\left(\frac{[A]}{[B]}\right)$$

Equation 4. Nernst equation

In the Nernst equation, $E^{o'}$ is the formal potential, n is the number of electrons transferred in the redox reaction, $[A]$ is the concentration of oxidized species at the electrode surface, and $[B]$ is the concentration of reduced species.

4.3 Cyclic Voltammetry (CV)

A commonly used electroanalytical technique to investigate the reversibility and kinetics of chemical reactions, as well as the identification of reaction intermediates and unknown analyte concentrations, is cyclic voltammetry. The input potential waveform $\phi(t)$ consists of *n* periodic cycles of two back-to-back linear scans defined by a scan-rate (*v*) and initial, high, low, and final potentials (as indicated in Figure 4.1).

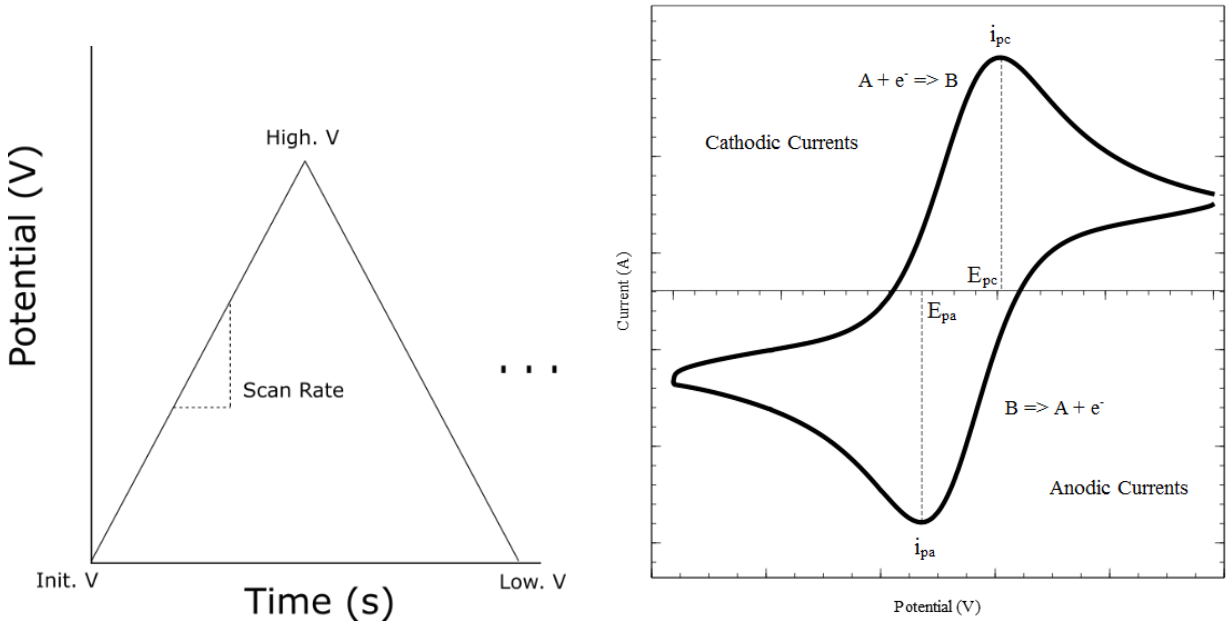

Figure 4.1 (Left) The applied potential waveform for cyclic voltammetry showing key characteristics of the signal. (Right) The resulting current signal detected for a one-electron transfer reaction.

A typical measured i-E response for a one electrode transfer of a single redox couple is illustrated, with cathodic (reductive) currents in the positive y-axis and anodic (oxidative) currents in the negative y-axis. The cyclic voltammogram contains periods of increasing and decreasing current between both a reduction (i_{pc}) and oxidation (i_{pa}) current peak, which represent maximum rates of current generation [137]. These changes in current, assuming an

abundance of redox species in solution, are attributed to diffusion-limited (diffusion of bulk redox species to the electrode surface) and reaction-limited regimes (conversion of surface-adsorbed redox species).

This work utilizes the ferrocyanide/ferricyanide couple for CV measurements:

$$[Fe^{II}(CN)_6]^{3-} + e^- \Leftrightarrow [Fe^{III}(CN)_6]^{4-}$$

Current peaks of a CV are dictated by the Randles-Sevčik equation (assuming T = 25 degree Celsius):

$$i_p = kn^{\frac{3}{2}} AC\sqrt{D}\sqrt{v}$$

Equation 5. General Randles-Sevčik equation [136]

where k = 2.69x10^5 C mol^{-1} V$^{-1/2}$, n is the number of electrons transferred in the redox reaction, A is the electrode area, D is the diffusion coefficient of the analyte, and v is the CV scan rate.

For a reversible system in which electron transfer is rapid between species, the Randles-Sevčik equation reduces to:

$$i_p = 2.69x10^5 AC\sqrt{D}\sqrt{v}$$

Equation 6. Simplified Randles-Sevčik equation

The formal reduction potential of the redox couple is related to the peak separation:

$$E^{o'} = \frac{E_{pa} + E_{pc}}{2}$$

And the difference between peak potentials can be quantitatively determined:

$$E_{p-p} = E_{pa} - E_{pc} = \frac{59}{n}$$

Important metrics observed from the CV include the magnitude of peak currents (correlated to the amount of faradaic current generated at the surface from redox reactions), the difference in potential at which these current peaks occur ($E_{p-p,}$ indicating a departure from reversibility), and the shape of peaks (indicating fast or slow reaction kinetics).

4.4 Differential Pulse Voltammetry (DPV)

The interface between electrode and electrolyte contributes a capacitive effect on the electrochemical system to an applied potential across the interface. To minimize the effect of this capacitance, differential pulse voltammetry applies a step-wise, stair-case waveform (illustrated in Figure 4.2) which steps to a potential, holds this potential for a time t¸ allowing a discharge of capacitive currents to occur, before the current is sampled at the falling edge to construct the resulting i-E curve with capacitive currents minimized. Important metrics observed from a DPV curve include the current magnitude and potential of redox peaks [136].

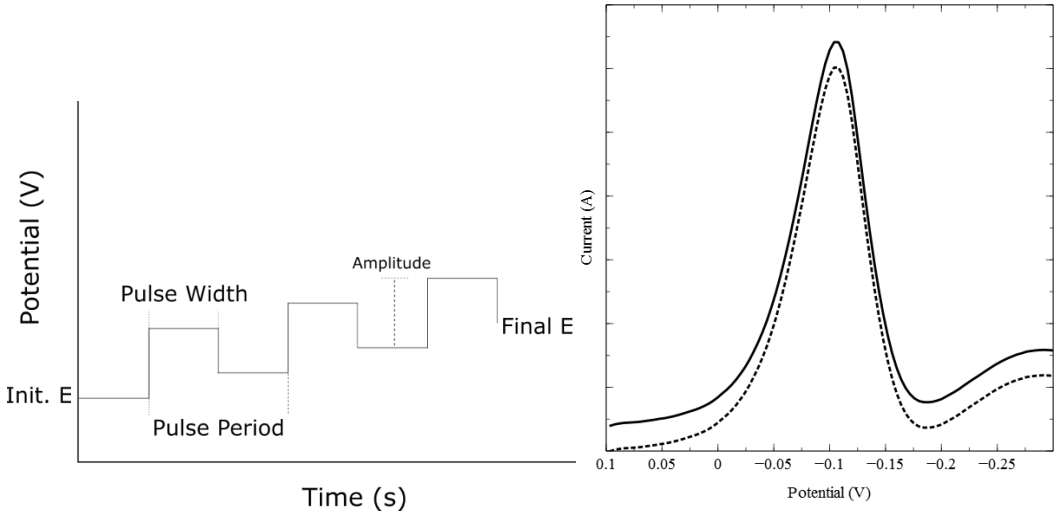

Figure 4.2 (Left) Input signal for differential pulse voltammetry with defining signal characteristics. (Right) The current signal before (solid) and after (dotted) background-signal adjustment.

Current peaks are analyzed by subtracting the detected current peak with background currents (as shown in Figure 4.2). This background current, for this work, is taken to be the lowest observed current at more positive potentials.

4.5 Chronocoulometry (CC)

The input potential waveform for chronocoloumetry is shown below in Figure 4.3. A potential step is applied to the electrochemical system and the resulting charge (Q) is recorded with respect to time [136].

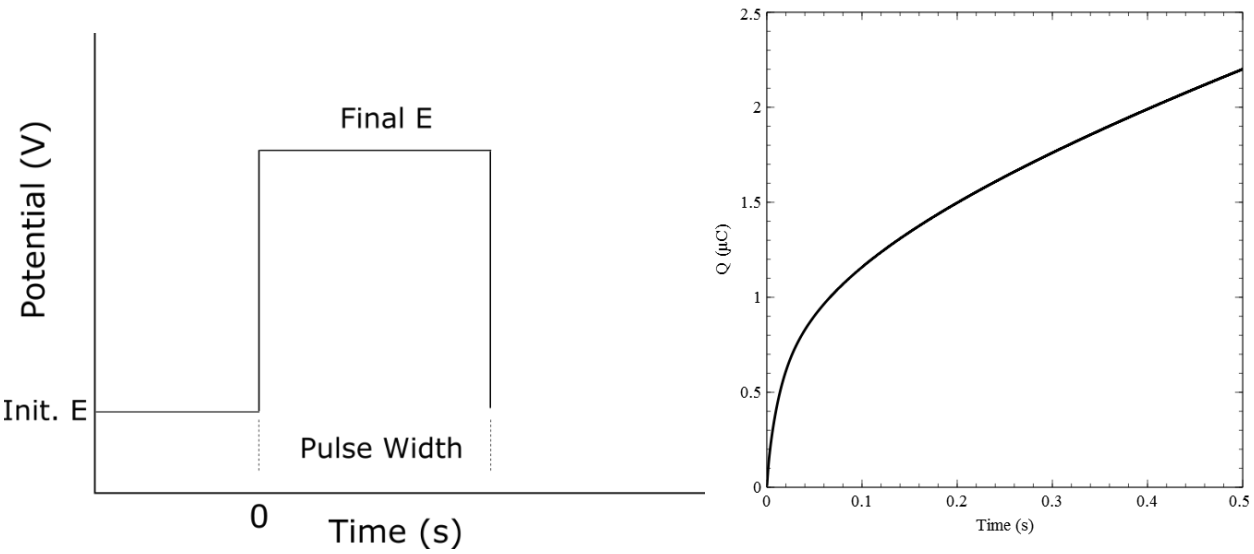

Figure 4.3 (Left) Input potential waveform for CC and its characteristic signal properties. (Right) A typical response to a CC waveform of a redox molecule at a planar gold surface showing reaction-limited and diffusion-limited regimes.

The current at a planar electrode from a potential-step waveform is governed by the Cottrell equation:

$$i(t) = \frac{nFA\sqrt{D_O}C_o^*}{\sqrt{\pi}\sqrt{t}}$$

Equation 7. Cottrell equation

where n is the number of electrons transferred in the redox reaction, F is Faraday's constant, D_O is the diffusion coefficient of the reducible analyte, C_o^* is the concentration of the reducible analyte at the electrode surface, and t is time.

In reference to Figure 4.3 (right), the steep increase in charge is associated with a reaction-limited regime in which redox molecules close to the electrode surface are reduced at a certain rate of reaction. As time progresses, the increase in charge adopts a linear-like trend. This marks a transition to a diffusion-limited regime in which redox molecules from the bulk electrolyte must diffuse to the electrode surface to replenish the concentration of reducible analyte (section 4.1).

4.7 DNA Electrochemical Detection with Planar Gold Macro-electrodes

The electrochemical techniques described in sections 4.4, 4.5, 4.6 are now applied to performing DNA electrochemical detection on planar gold macro-electrodes. The protocol for preparation of DNA and electrodes are given in section 4.7.1. Sections 4.7.2 and 4.7.3 present results for CV electro-polishing and CV detection respectively. Section 4.7.4 presents results for the electrocatalytic detection of DNA with DPV, and section 4.7.5 presents the results for the quantitation of probe DNA surface density by CC. Section 4.7.6 then outlines the protocol for performing limit-of-detection studies for DNA detection.

4.7.1 Protocol for Electrochemical DNA Sensing

This subsection describes the preparation of thiolated-probe DNA and the deposition conditions used to deposit probe, MCH, and target DNA onto the electrode surface.

4.7.1.1 Materials and Reagents

The following reagents were purchased from Sigma-Aldrich (St. Louis, Missouri): Potassium Chloride (KCl, ≥ 99.0%), Phosphate Buffered Solution (PB solution, 1.0 M, 7.4 pH), 2-mercaptoethanol (MCE, ≥ 99.0%), 6-mercapto-1-hexanol (MCH, ≥ 99.0%), hexaammineruthenium (III) chloride (RuHex, 98%), potassium hexacyanoferrate (II) trihydrate (FoCN, 98.5%). Potassium ferricyanide (FiCN, 99.0%) was purchased from Anachemia (Rouses Point, NY). Sulfuric Acid (H_2SO_4, 98%), 2-propanol (99.5%), sodium chloride (NaCl, ≥ 99.0%), methanol (≥ 99.8%) were purchased from Caledon Laboratories (Georgetown, Ontario). Ethanol was purchased from Commercial Alcohols (Brampton, ON). Sodium Hydroxide was purchased from LabChem Inc. (Zelienople, PA). Tris-EDTA (TE Buffer, pH = 8.0) and Tris-(2-Carboxyethyl)phosphine, hydrochloride (TCEP) was purchased from Thermo Scientific (Rockford, Illinois). Tris(hydroxymethyl)aminomethane (tris, ≥99.9%) was purchased from BioShop Canada (Burlington, ON). All other reagents were of analytical grade and were used without further purification. Milli-Q grade ultrapure water (18.2 MΩ·cm) was used to prepare all solutions and for all washing steps.

4.7.1.2 DNA Sequences

The following oligonucleotide sequences were synthesized and purchased from Integrated DNA Technologies (IDT, Coralville, Iowa): Thiolated Probe DNA (‘5-/5ThioMC6-D/CTG GCC GTC GTG GCC CGC AC -3’), Complementary Target DNA (5’-/5ThioMC6-D/CTG GCC GTC GTG GCC CGC AC -3’), and Non-Complementary Target DNA (5’-TTT TTT TTT TTT-3’). The /ThioMC6-D/ represents a 6 carbon alkanethiol mercaptohexanol (MCH) bound by disulfide link to another 6 carbon alkanethiol attached to the phosphate group of the 5’ cytosine as shown in Figure 4.4:

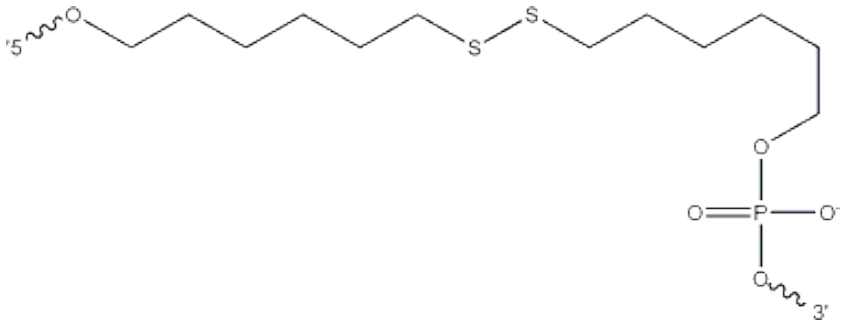

Figure 4.4 5’ modifier on Probe DNA [IDT DNA].

4.7.1.3 Electrode Preparation

Planar gold disk macro-electrodes (CH instruments 101) were used to establish the electrochemical detection scheme. Before use, macro-electrodes were manually polished with CarbiMet to remove large scratches. Next, electrodes were polished in “figure-8” motions with 0.3 μm alumina beads on a polishing cloth damp with DI water, sonicating for 5 minutes each in ethanol and then DI water, and repeating polishing and sonicating with 0.05 μm alumina beads, using the same conditions.

Electrodes were then electrochemically polished together by performing CV in 0.05 M H_2SO_4 between 0 V and +1.5 V scanning at a rate of 0.1 V/s for 80 cycles. Afterwards, each electrode was individually scanned for 6 cycles at a scan rate of 0.05 V/s, or until scans were repeatable and consistent.

Integration of the reduction peak yields the amount of charge from the reduction of chemisorbed oxygen molecules on the electrode surface. Dividing this value by the surface charge density of a

single monolayer of gold (386 μC/cm^2) yields the electrochemically active surface area of the electrode [138]. Afterwards, "Bare" CV and DPV scans were taken as a baseline measurement of a bare gold surface without modification.

4.7.1.4 DNA Preparation

Lyophilized probe DNA, when received, was resuspended with 1 x TE Buffer to 1 mM concentration and 25 uL aliquots were created and stored at 20 Celsius. To cleave the disulfide bond of the 5' modifier on the probe DNA (revealing the thiol attachment of the DNA molecule and releasing MCH into solution), the following series of steps were performed as illustrated in: 50 uL of a 10 mM TCEP solution was added to 25 uL of unreduced probe DNA. This mixture was briefly vortexed and left at room temperature for the reduction reaction to complete for 1 hour. This mixture was then added to a Nanosep 3 kDa spin column with 150 uL of a 1 mM NaCl and 100 mM PB solution. Filtration was performed for 15 minutes at 8.6 kRPM. At conclusion of spinning, 75 uL of 1000/10 was added to the retentate and spun at the same conditions for 15 minutes. This addition of 1000/10 to the retenate and spinning was repeated for an additional 2 times, such that a total of 4 spins were performed. Finally, the retentate was collected in a 75 uL of solution of 1000 mM NaCl and 10 mM PB solution (1000/10) and stored in 4 degrees Celsius wrapped in aluminum foil. This solution was diluted with 1000/10 to a concentration of 5 μM to create the probe deposition solution.

To quantitate the concentration of probe DNA reduced, 15 uL of reduced probe DNA was added to 185 uL of a solution containing 100 uM DTNB, 0.1 M PB solution, and 1 mM EDTA to a UV-transparent 96-well plate. Blanks were created by adding 15 uL of 1000/10 to 185 uL of the same solution. Reduction efficiency was determined by comparing DNA concentrations from 260 nm (native DNA absorbance) and 410 nm (thiol-DTNB absorbance) absorbance readings. This protocol ensures 90-100% reduction efficiencies.

4.7.1.5 Probe Deposition

The electrodes were then washed and placed into individual 50 mL Falcon tubes with Styrofoam pieces, such that electrode surfaces were facing upwards. Water was placed into the tubes to create a humidity chamber limiting evaporation. 5 uL of probe deposition solution was placed onto each electrode and each tube was capped to seal and protect the internal environment.

Chemisorption of thiolated-DNA to the gold surface was allowed to proceed before the electrodes were removed from the chambers and washed with 25/25 and water.

Electrodes were then replaced into the humidity chambers as for probe deposition, and 5 uL of a 1 mM MCH solution was placed onto each electrode for a backfill step for 1 hour. Electrodes were then washed with 25/25 and water, and immersed in PB solution.

“Probe” CV and DPV scans were then taken. In reference to Figure 4.1, the CV scan parameters that were used in this work are given in Table 4.1. CV scans were performed in 25 mM NaCl, 25 mM PB solution,

Table 4.1 CV scan parameters used with the CHI660D potentiostat.

Init E (V)	0
High E (V)	0.5
Low E (V)	0
Final E (V)	0
Initial Scan Polarity	Positive
Scan Rate (V/s)	0.05
Sweep Segments	12
Sample Interval (V)	0.001
Quiet Time (s)	0.5
Sensitivity (A/V)	1.00E-05

In reference to Figure 4.2, the DPV scan parameters that were used in this work are given in Table 4.2.

Table 4.2 DPV scan parameters used with the CHI660D potentiostat.

Init E (V)	0.1
Final E (V)	-0.3
Incr E (V)	0.004
Amplitude (V)	0.05
Pulse Width (s)	0.1
Sampling Width (s)	0.0167
Pulse Period (s)	0.2
Quiet Time (s)	1.5
Sensitivity (A/V)	1.00E-04

4.7.1.6 Hybridization

Electrodes were returned to their individual humidity chambers and 5 uL of a 1 uM hybridization solution was placed on the electrodes, which were then covered and placed onto a shaker for 1 hour at 37 degrees Celsius. Electrodes were then washed with 25/25 and water. “Target” CV and DPV scans were then taken.

4.7.2 Electrochemical Polishing by CV

Cyclic voltammetry can be used for the electrochemical polishing of conductive gold surfaces. This technique is due to the oxidation and reduction of an adsorbed layer of gold oxide at the surface of the gold. A representative cyclic voltammogram of a sulfuric acid scan of a planar gold surface is shown in Figure 4.5 below.

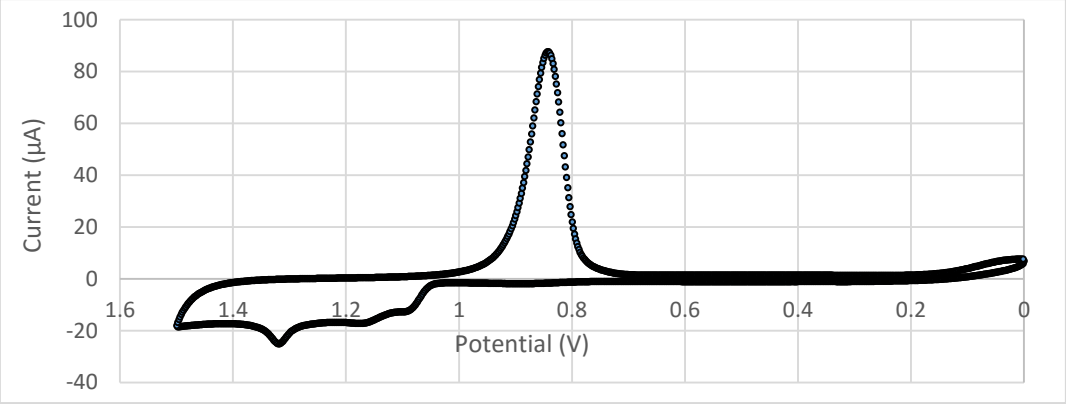

Figure 4.5 Sulfuric acid CV of a planar gold electrode in 0.05 M sulfuric acid at a scan rate of 0.1 V/s.

Between +1.0 V and +1.5 V, the oxidation of gold occurs. Upon a reversal in scan polarity, a reduction reaction occurs indicated by a characteristic peak at approximately +0.83 V. The electro-active surface area may be determined from the charge associated with the reduction current by integrating the peak area, and dividing this value by the surface charge density of gold (386 $\mu C/cm^2$).

4.7.3 CV for DNA Electrochemical Detection

As described in section 4.4, cyclic voltammetry permits an understanding of the dynamic between the state of the electrode surface and reaction characteristics of redox processes at the

interface. Modification of the electrode surface leads to a change in charge-transfer ability to redox species in solution and at the interface.

Figure 4.6 below shows cyclic voltammograms of a bare planar gold surface, probe-MCH monolayer modified surface, and target-bound monolayer surface. Examining the bare CV scan, clear oxidation and reduction peaks can be seen as introduced in section 4.4 and reflects an uninhibited surface for the charge-transfer reaction for the reduction (I_{pc} = 6.15 μA, E_{pc} = 0.19 V) and oxidation (I_{pa} = -7.97 μA, E_{pa} = 0.266 V) of FiCN and FoCN. Sharp peaks indicate rapid diffusion of reduced or oxidized species into or away from the solid-solution interface.

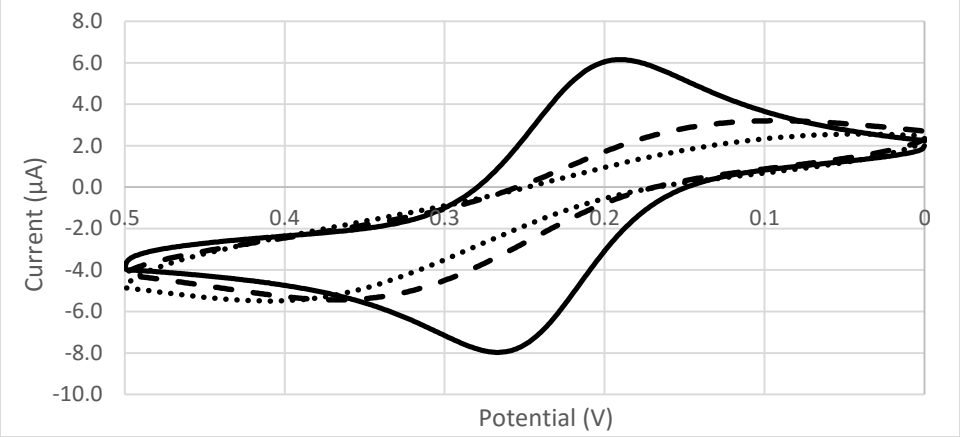

Figure 4.6 Cyclic voltammogram of a planar gold surface at bare (solid), probe-MCH monolayer (dashed), and target-hybridized states (dotted). CV was performed in 25 mM PB solution, 25 mM NaCl, and 2 mM FoCN with the scan settings shown in Table 4.1.

For the bare surface, the E_{p-p} is 0.076 V. Compared to the theoretical E_{p-p} of 0.059 V for a reversible one-electron transfer, there is a small discrepancy owing to finite solution resistance. Following probe DNA deposition and MCH back-fill, the resultant CV shows highly reduced and indistinguishable current peaks (approx. I_{pc} = 3.2 μA, I_{pa} = -5.44 μA) and a wider peak separation (approx. E_{pc} = 0.094 V, E_{pa} = 0.367 V, E_{p-p} = 0.273 V), both indicating slower reaction kinetics and reduced current from fewer faradaic processes. These results are indicative of surface blocking causing fewer FoCN/FiCN molecules from reaching the bare gold surface to be oxidized/reduced to FiCN/FoCN. This blocking is due to the physical impediment of the probe DNA and MCH monolayer, as well as the electrostatic repulsion of negatively charged phosphate groups of the DNA backbone and the negatively charged FiCN/FoCN molecule.

Upon introduction of complementary target DNA, the blocked monolayer exists as before, but now includes duplex DNA. This increases the electrostatic repulsion of FoCN, causing a further decrease in currents and a widening of the peak separation indicating further decrease in reaction kinetics. This is indicated in Figure 4.6, which shows reduced current peaks (I_{pc} = 2.56 μA, I_{pa} = -5.5 μA) and an increase in peak potential separation (approx. E_{pc} = 0.043 V, E_{pa} = 0.409 V, E_{p-p} = 0.366 V)

Although the changes to faradaic charge transfer can be characterized with cyclic voltammetry, specific detection of probe DNA surface-binding and complementary target DNA hybridization cannot be specifically detected, as any surface blocking can reduce faradaic currents. As such, differential pulse voltammetry (DPV) offers specific DNA detection ability.

4.7.4 DPV for DNA Electrochemical Detection

As described in section 3.3.1, electrocatalytic detection is a method to amplify faradaic current generation. In this work, FiCN is used to replenish RuHex back to its oxidized form such that it can be reduced again. RuHex binds in greater amounts to duplex DNA, such that higher electrocatalytic current is generated than when bound to ssDNA. This increase in current signifies the hybridization of target DNA to probe DNA.

An example of DPV scans of bare, probe-MCH, and target hybridized states of planar gold surfaces are presented in Figure 4.7.

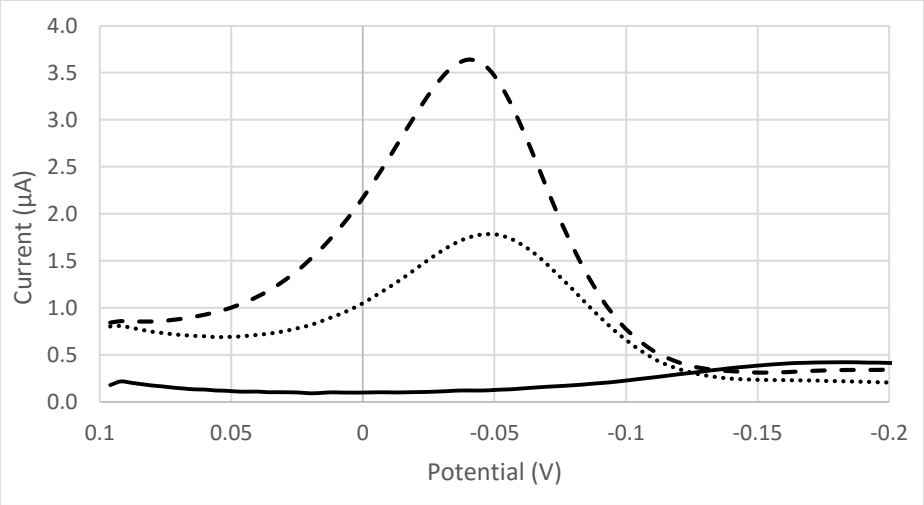

Figure 4.7 DPV of bare (solid), probe-MCH (dotted), and target-bound (dashed) states indicating peak currents due to electrocatalytic detection of DNA. Scans were performed in 25 mM NaCl, 25 mM PB solution, 27 µM RuHex, and 2 mM FiCN with the scan settings given in Table 4.2.

At the bare electrode state, a low background current is detected from double-layer charging currents and residual current from the reduction and oxidation of RuHex and FiCN at ranges outside of the observed potential range. When probe DNA is present, RuHex is electrostatically attracted to the polyanionic backbone in a stoichiometric relation of 1 RuHex molecule to 3 bases. Electrocatalytic detection of this state is indicated by a noticeable peak current. Upon the presence of hybridized DNA, a greater amount of RuHex is attracted due to the increase in anionic charge. This is detected as a greater increase in the peak current than measured with change probe DNA present.

The change in the current signal can be calculated by first subtracting the background potential from each peak value (in this example, the currents at ~0.1 V) and calculating the % change as follows:

$$Peak\ Signal\ Change = \frac{\left|I_{Target} - I_{Probe}\right|}{I_{Probe}} * 100\%$$

Equation 8. Percentage change in DPV current peaks

For this example, the peak signal change between probe and target scans was found to be 185%.

4.7.5 Determination of Probe Density

A method reported by Steel et. al [139] is used to quantify the amount of surface-bound probe DNA on a planar gold surface. CC is performed first in a 10 mmM tris buffer solution, followed by a scan in a solution of both 10 mM tris and 100 µM RuHex, using the scan parameters given in Table 4.3.

Table 4.3 CC scan parameters used with the CHI660D potentiostat.

Init E (V)	0.15
Final E (V)	-0.35
Number of Steps	1
Pulse Width (s)	0.5
Sample Interval (s)	0.00025
Quiet Time (s)	5
Sensitivity (C or A/V)	1.00E-05

The data collected is first plotted as Q vs. $t^{1/2}$, known as an Anson plot, as demonstrated in Figure 4.8 below.

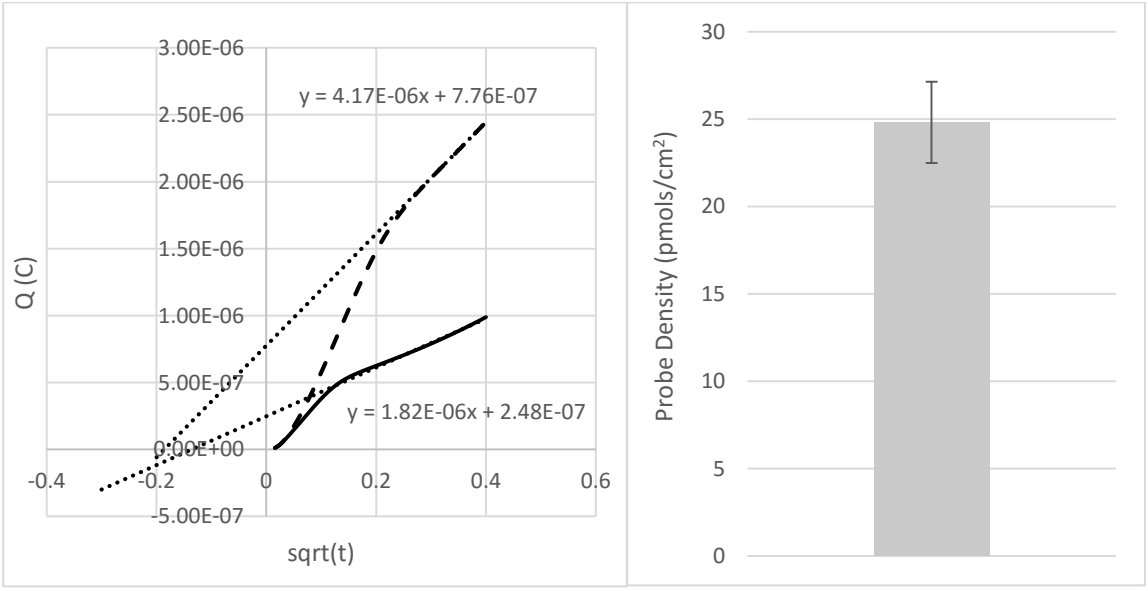

Figure 4.8 (Left) CC data plotted as an Anson plot showing the least-squares fit to the linear portions of the 10 mM tris (solid) and 10 mM tris + 100 µM RuHex (dashed) scans, indicating the y-intercept of both fits. (Right) Probe density measurement from Anson plot analysis.

The defining equation (Equation 9) which relates the total charge detected to the component of charge related to RuHex diffusing to the surface, a charge related to the electrochemical double-layer, and charge associated with reduction of RuHex electrostatically attracted to the polyanionic backbone of DNA in a stoichiometrically defined manner (1 RuHex to 3 bases) is given as:

$$Q = \frac{2nFAD_o^{1/2}C_o^*}{\pi^{1/2}}t^{1/2} + Q_{dl} + nFA\Gamma_o$$

Equation 9. Total charge detected by CC of RuHex

Performing a CC scan without RuHex causes the charge to only occur by the double-layer charge (Q_{dl}). As such, analyzing the Anson plot at t = 0 reduces the above equation to contributions of current by the double-layer charge and surface-confined RuHex. More specifically, by subtracting the y-intercept of the least-squares fit to the linear-charge regime on both scans:

$$Y\ Intercept_{(Tris+RuHex)} - Y\ Intercept_{(Tris)} = (Q_{dl} + nFA\Gamma_0) - Q_{dl} = nFA\Gamma_0$$

This simplification of charge associated with surface-confined RuHex can then be used to determine the probe density (Γ_{DNA}):

$$\Gamma_{DNA} = \frac{z}{m}\Gamma_o$$

Equation 10. Probe density by Anson plot

where *z* is the charge of an individual RuHex molecule and *m* is the number of bases of the probe DNA.

4.7.6 Protocol for Limit of Detection (LOD) Study

The limit of detection experiment characterizes the lowest amount of complementary target DNA which can be detected and distinguished from non-complementary target DNA. The LOD is performed by depositing the maximum number of probes to the sensor surface, performing a backfill of 1 mM MCH for 1 hour, and subjecting electrodes to step-wise concentrations in complementary target DNA from the lowest concentration upwards in 100x increments. A separate set of electrodes is subjected to 1 μM of non-complementary target DNA and the

resulting % change in the DPV signal is considered as the background signal change. The lowest concentration which results in a % change greater than a factor of 3 of its standard deviation, and greater than the background percentage change, is considered the limit of detection. All target DNA are deposited for 1 hour at 37 degree Celsius and electrocatalytic solutions were purged with nitrogen and stored in 50 mL Falcon tubes at 4 degree Celsius for further use.

This protocol will be used to determine the LOD of rapidly-prototyped, all-solution processed electrodes in the following section.

4.8 Conclusion

This section described the nature of the electrochemical double-layer and the mechanism which charge is transferred by redox species through mass transport from bulk solution to the electrode surface, and how charge is then transferred into and out of the electrode due to redox reactions. The techniques used in this work – CV, DPV, and CC – were introduced in the context of performing DNA electrochemical sensing and was demonstrated with planar gold electrodes.

These concepts and techniques will be fundamental to understanding the DNA electrochemical detection scheme using all-solution processed electrodes (section 5.0) and to the investigation of a new technique to measure hybridization efficiency (section 6.0).

5.0 All-Solution-Processed Electrodes for DNA Electrochemical Sensing

Improvements to the wrinkled, sputtered polystyrene electrodes (WSPEs, introduced in section 2.0) include the increase in specificity of metal deposition during fabrication so as to minimize wasted metal, and the movement away from cost-bearing infrastructure and equipment, such as vacuum-based deposition technology. This section describes a novel fabrication procedure for wrinkled, electrolessly-deposited polystyrene electrodes (WEDPEs) performed wholly using solution-based methods (section 5.1), and which retains the micro/nano-texturing feature of polystyrene-based, thin-film metal electrodes. Furthermore, these electrodes contain porous structures. The sizes of these pores change with fabrication conditions and such, offers an additional dimension of tunability unseen in prior devices (section 5.2). The suitability of these electrodes for DNA electrochemical DNA detection is then demonstrated (section 5.3).

5.1 Fabrication Protocol

The following fabrication protocol was devised by a collaborator but performed by the author of this work. A schematic of the overall fabrication protocol is illustrated in Figure 5.1 below. The fabrication scheme combines the following techniques: xurography and surface silanization (section 5.1.1), Au-NP seed-layer formation (section 5.1.2), followed by electroless-deposition and device shrinking (section 5.1.3).

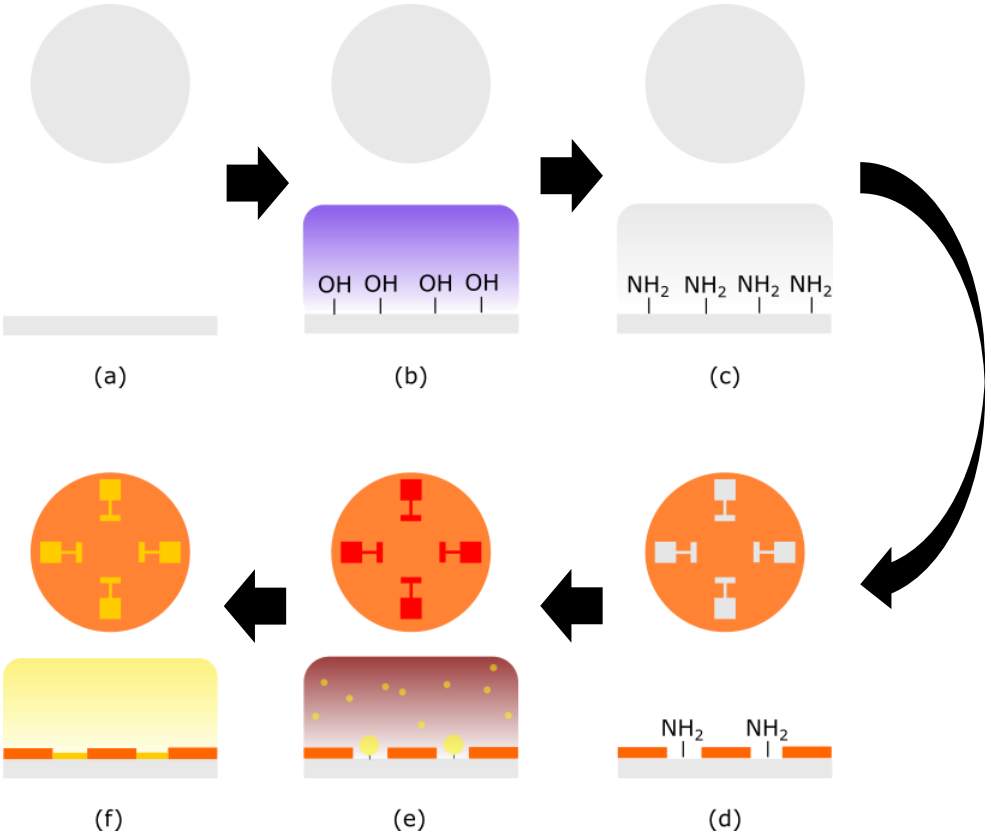

Figure 5.1 Fabrication process flow for wrinkled, electrolessly-deposited electrodes. (a) Clear pre-stressed polystyrene sheets are cut into 33 mm diameter circles and sonicated in DI water. (b) Substrates are then plasma treated to form hydroxyl groups on the surface. (c) APTES treatment then allows the formation of surface amine groups. (d) A vinyl mask with the electrode designs created by xurography is adhered to the substrate. (e) These are then submerged in a solution of 12 nm Au-NPs which allow the attachment of Au-NPs to surface amine groups, creating a seed layer. (f) Electroless-deposition of gold is then performed where the seed layer acts as nucleation sites for the growth of gold structures. Devices are then trimmed of excess polystyrene and heated to shrink the electrodes.

5.1.1 Xurography and Substrate Treatment

Firstly, a xurographic procedure was employed to prepare devices substrates. Circles of diameter 33 mm of clear, pre-stressed polystyrene (Graphix Shrink Film, Graphix, Maple Heights, Ohio**)** were cut using a craft cutter (Robo Pro CE5000-40 CRP; Graphtec America Inc., Irvine, CA**)** and scribed with a tweezer to demarcate bottom and top surfaces. These circular substrates were then sonicated in a beaker containing 2-propanol for 5 minutes, rinsed with DI water, and then sonicated further for 5 minutes in DI water. These substrates were then dried with a stream of air.

A procedure for silanization (the surface self-assembly of organofunctional alkoxysilane groups) of the substrate surface was subsequently performed. The circular substrates (ensuring the unmarked sides were facing outwards) were plasma-treated (Harrick Plasma) on high for 1 minute. Immediately following plasma treatment, substrates were then bathed in a 30% (3-aminopropyl)triethoxylsilane (APTES) solution overnight in a petri dish with slight shaking in an Incubating Mini Shaker (VWR International) to ensure even surface coverage of the APTES solution.

Substrates were then removed from the APTES solution and rinsed with DI water, followed by sonication in DI water for 5 minutes and drying with a stream of air. Mask designs were created in Adobe Illustrator and cut into vinyl (FDC 4304, FDC graphic films, South Bend, Indiana). These vinyl designs (one-side sticky) were then applied to the surface-treated substrates to act as masks for metal deposition and individually placed into small petri dishes, held in place with double-sided tape. As such, exposed areas on the vinyl mask reveal bare-polystyrene surfaces modified with amine functional groups.

5.1.2 Synthesis of 12 nm Gold Nanoparticles

Synthesis protocol 1 by Grabar et. al [140] was followed to create a solution of 12 nm diameter gold nanoparticles (Au NPs) and is based on the Turkevich method [141]. Briefly, a 500 mL Erlenmeyer flask and magnetic stirring rod were thoroughly cleaned with a dilute hydrogen chloride solution and rinsed with DI water. To a graduated cylinder, 207.6 uL of a gold chloride solution (30% wt) was added to 300 mL of DI water to create a 1 mM gold chloride solution and poured into the flask. This gold chloride solution was heated to 100 degree Celsius and stirred on a hot-plate at maximum speed (1200). Upon boiling, 30 mL of a 38.8 sodium citrate solution was

immediately added and the solution was left to heat for an additional 10 minutes. Afterwards, the solution was removed from heating and stirred for an additional 15 minutes. The nanoparticle solution was then separated into 50 mL aliquots and stored at 4 Celsius until further use. Confirmation of 12 nm particle size was confirmed by UV absorbance measurement, identifying a characteristic peak at 520 nm, as shown in

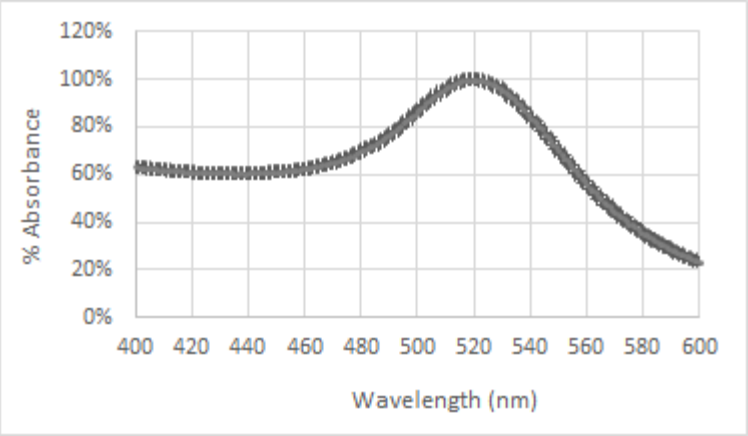

Figure 5.2 Absorbance scan (% of peak intensity) of synthesized Au-NPs. The absorbance maximum occurs at 520 nm which confirms the presence of 12 nm Au-NPs. The scan presented is an average of 3 measurements. Standard error bars are shown.

5.1.3 Electroless Deposition

To create a seed-layer for the subsequent electroless deposition of gold, a sufficient volume of the synthesized 12 nm Au-NP solution was added to the Petri dishes containing the surface-treated, polystyrene circular substrates for complete surface coverage and left at room temperature for 18 hours. This allows for Au-NP attachment from solution to surface amine groups on the on exposed areas of the substrate, which act as a seed layer for nucleation sites for subsequent gold deposition [142]. Substrates were then carefully removed from the dishes with tweezers, thoroughly washed with DI water to ensure that residual Au NP solution was removed before being placed into new Petri dishes. To these dishes, 5 mL of a 0.1% (v/v) gold chloride solution was added and shaken on an incubating mini shaker at 250 RPM at room temperature.

To initiate Au deposition, 250 µL of hydrogen peroxide was added for a desired deposition period, ensuring that bubbles which formed on the vinyl mask were removed by gentle pipetting. The hydrogen peroxide acts as a reducing agent to Au ions according to Equation 11.

$$2AuCl_4^- + 3H_2O_2 \rightarrow 2Au + 3O_2 + 8Cl^- + 6H^+$$

Equation 11. Reduction of Au ions

Samples were then removed from the dishes and vinyl masks were removed and substrates were thoroughly washed with DI water and dried with air. Excess substrate was cut, whereupon samples were heated at 160 Celsius for 3 minutes in an oven (Model 664, Fisher Scientific, Mariette, OH). As with polystyrene-sputtered devices, length and width dimensions shrink by 60% post-heating (section 2.5.2)

5.2 Characterization of Electrode Topography

Surface characterization of WEDPEs was performed by optical analysis of shrunk electrodes (5.2.1), electrochemical analysis of surface area (5.2.2) followed by topographical analysis by scanning electron microscopy SEM (5.2.3).

5.2.1 Optical Measurements

Samples of 2 min., 8 min., and 20 min., WEDPEs are shown in Figure 5.3 below. There is evidence of a varying deposition in gold thickness as indicated from the visual differences in luster, from dark for shorter deposition periods to lighter for longer deposition periods. The pre-shrunk electrode areas were designed to be 4.43 mm x 4.43 mm (area of 19.62 mm^2) such that the theoretical shrunk dimensions would be 1.72 mm x 1.72 mm (a reduction in dimensions by 60% [96]) and give an area of 0.0314 cm^2, or the same geometric surface as the gold planar macro-electrodes.

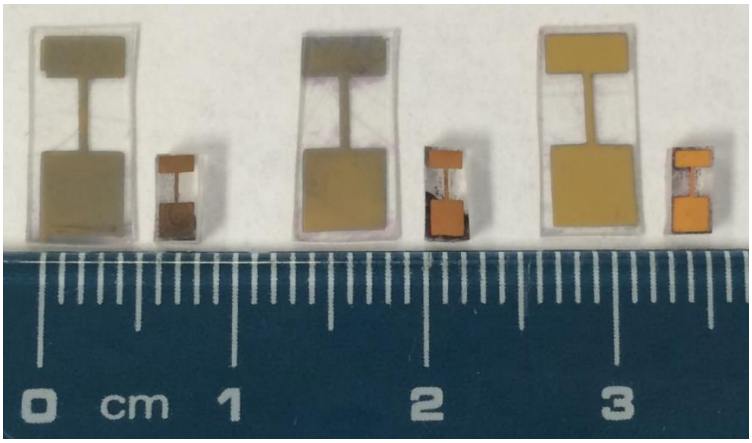

Figure 5.3 Images of pre-shrunk and shrunk 2 min. (left), 8 min. (center), and 20 min. (right) WEDPEs on clear polystyrene before and after shrinking.

ImageJ was used to measure the shrunk area for 3 electrodes in each group, as well as 3 for unshrunk planar electrodes deposited for 8 mins. From Figure 5., the shrunk surface areas are 2.934 mm^2±0.129 mm^2, 2.928 mm^2±0.168 mm^2, 3.014 mm^2±0.026 mm^2 which represents 93.439 %±4.108 %, 93.248 %±5.35 %, 95.987 %±0.828 % of a 60% reduced surface area (3.14 mm^2). For the planar electrode, the surface area is 18.776 mm^2±0.129 mm^2 which is 95.698%±0.657%). As such, all electrodes exhibit within 93% of theoretical area reduction. It was also noticed that electrodes contained a skew to the intended square shape. A % skew was determined by measuring the deviation of angles formed by connecting edges of the electrodes and expressing this as a percentage difference from 90 degrees. Only obtuse angles were measured.

$$\%\, Skew = \frac{Angle - 90^o}{90^o}$$

Equation 12. Calculation of % skew

The % skew was found to be 5.82%±1.36 %, 3.47%±2.43%, and 1.39%±1.28% for 2 min., 8 min., and 20 min., shrunk WEDPEs. For unshrunk planar electrodes deposited at a duration of 8 min., the % skew was 2.37%±2.02%.

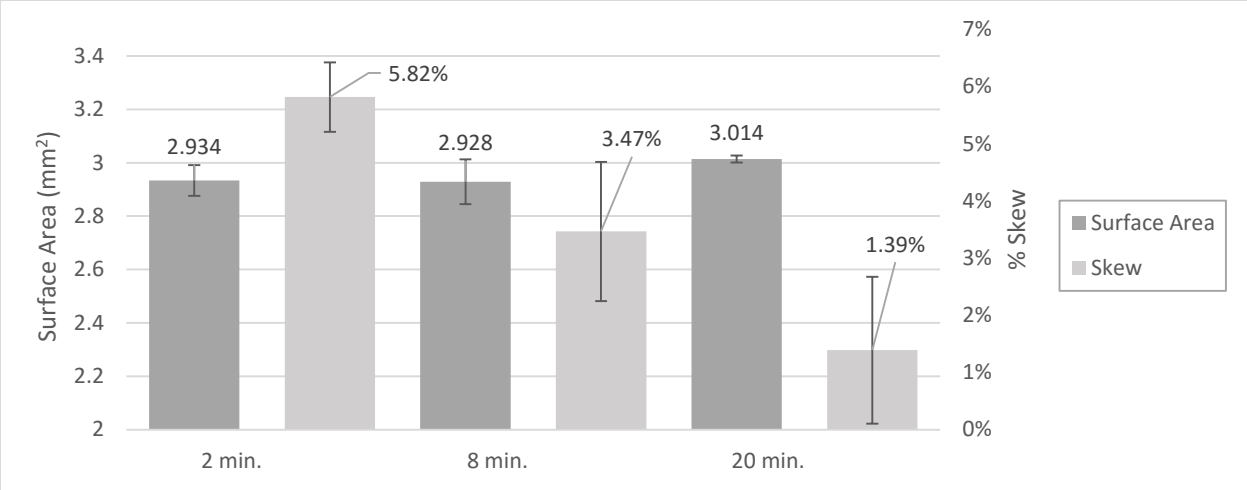

Figure 5.4 Measurements of shrunk WEDPE geometric areas and their associated % skew from a perfect square. Each measurement is an average of 3 electrodes. Standard error bars are shown.

Interestingly, a decrease in skew seems to occur with the increase in deposition duration. This could be due to a greater shape definition caused by a progressively complete gold layer (less sparsely deposited) forming with longer durations of electroless deposition, such that the edges of shapes, as well as areas inside the edges, are more defined with greater time. The definition of edges is also dictated by how well the vinyl mask sticks to the polystyrene substrate and the ability to prevent deposition underneath and around the edges of the mask.

5.2.1 Electro-Active Surface Area

Using the technique presented in section 4.3.1, 80 cycles of cyclic voltammetry were performed with 2 min., 8 min., and 20 min. deposited devices of geometric area 0.04 cm^2 in 0.05 M sulfuric acid at a scan rate of 0.01 V/s. Representative scans of each electrode are presented in Figure 5.5.

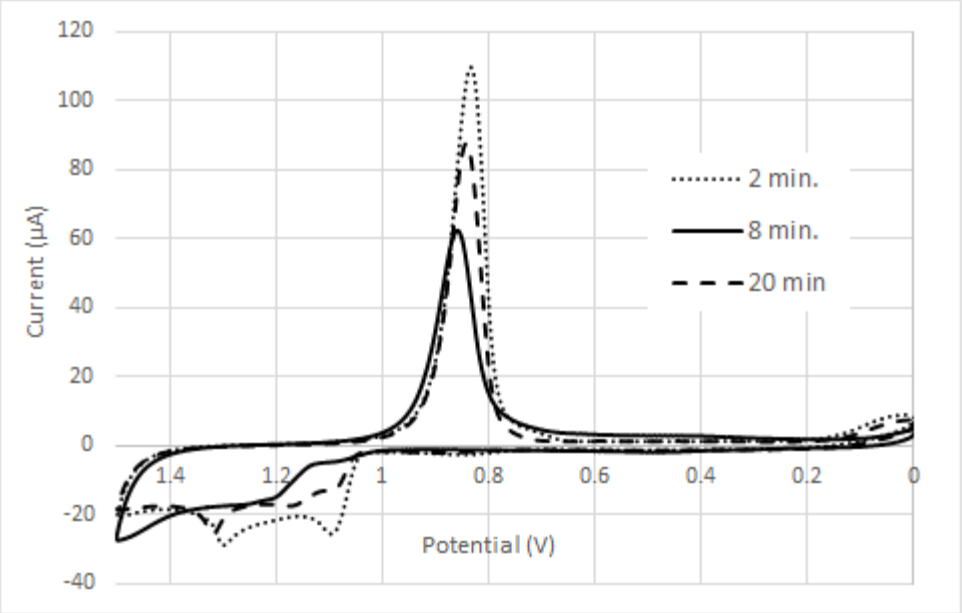

Figure 5.5 Representative H_2SO_4 CV scans of 2 min., 8 min., and 20 min., WEDPEs with geometric area of 0.04 cm^2.

All scans contain a well-defined region between +1.0 V and +1.5 V indicating the oxidation of gold, followed by a clear reduction peak situated at approximately +0.83 V. There exists a small shift to less negative potentials in the reduction peak potentials which does not follow an increase or decrease in deposition timing. This is considered to be a small deviation in the reference potential between scans and does not reflect a structure-dependent phenomenon. The results indicate that 2 min. devices have the largest electro-active surface area, followed by 20 min. and 8 min. devices.

For further analysis, 6 electrodes per each of 3 deposition timings (2 min., 8 min., and 20 min.), and 6 planar gold electrodes of geometric surface area 0.0314 cm^2, were scanned and the resulting electro-active surface areas were calculated (section 4.7.2) and averaged. The resulting areas for planar, 2 min., 8 min., and 20 min., devices are 0.044±0.0026 cm^2, 0.194±0.013 cm^2, 0.108±0.019 cm^2, and 0.112±0.0248 cm^2 respectively (results are shown in Figure 5..6).

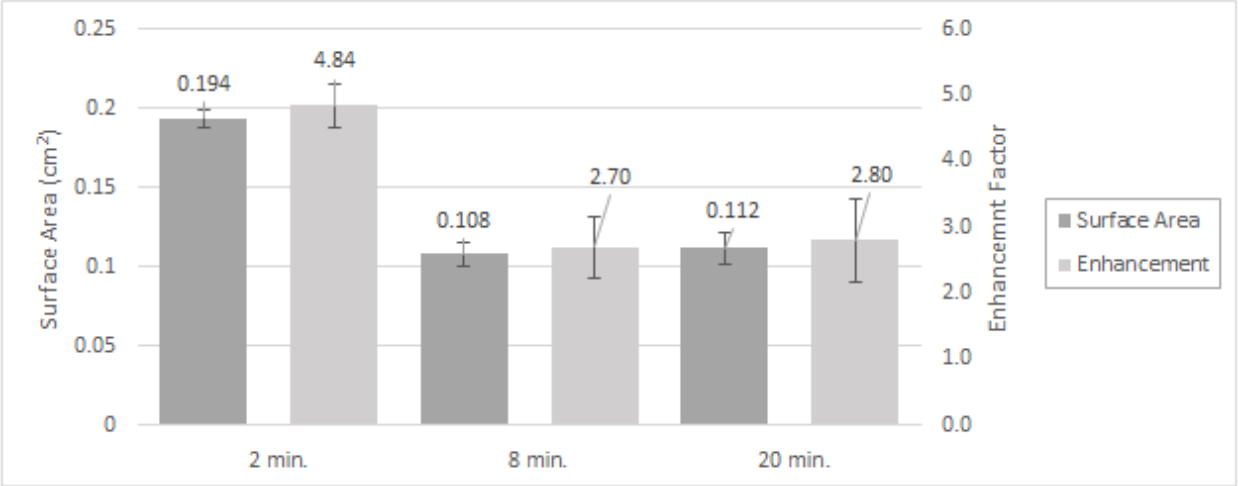

Figure 5.6 Electro-active surface area measurements of WEDPEs after shrinking, performed by CV scans in H_2SO_4 for 2 min., 8 min., and 20 min. deposition durations. Each is an average of 6 electrodes. Standard error bars are shown.

Electrolessly-deposited devices, after shrinking, were designed to be of geometric surface area 0.04 cm^2. Dividing the electro-active surface areas by the geometric area would yield the surface area enhancement arising from electrode structuring. For the strictly planar surface, this same calculation yields the roughness factor.

$$Surface\ Area\ Enhancement = \frac{Electro - Active\ Surface\ Area}{Geometric\ Surface\ Area}$$

Equation 13. Surface area enhancement factor

Performing this analysis results in surface area enhancements of 4.837±0.324, 2.698±0.470, and 2.797±0.619 for 2 min., 8 min., and 20 min. devices (Figure 5.6). A roughness > 1 for planar electrodes indicates a surface roughening attributed to uneven polishing of the electrode surface prior to sulfuric acid scanning. Despite this planar roughening, there is a clear increase in surface area enhancement of electrolessly-deposited devices over planar gold surfaces.

Preliminary work by our group have investigated the relationship between gold deposition thickness by electroless deposition against deposition time (shown in 5.7a), as measured by step-height measurements.

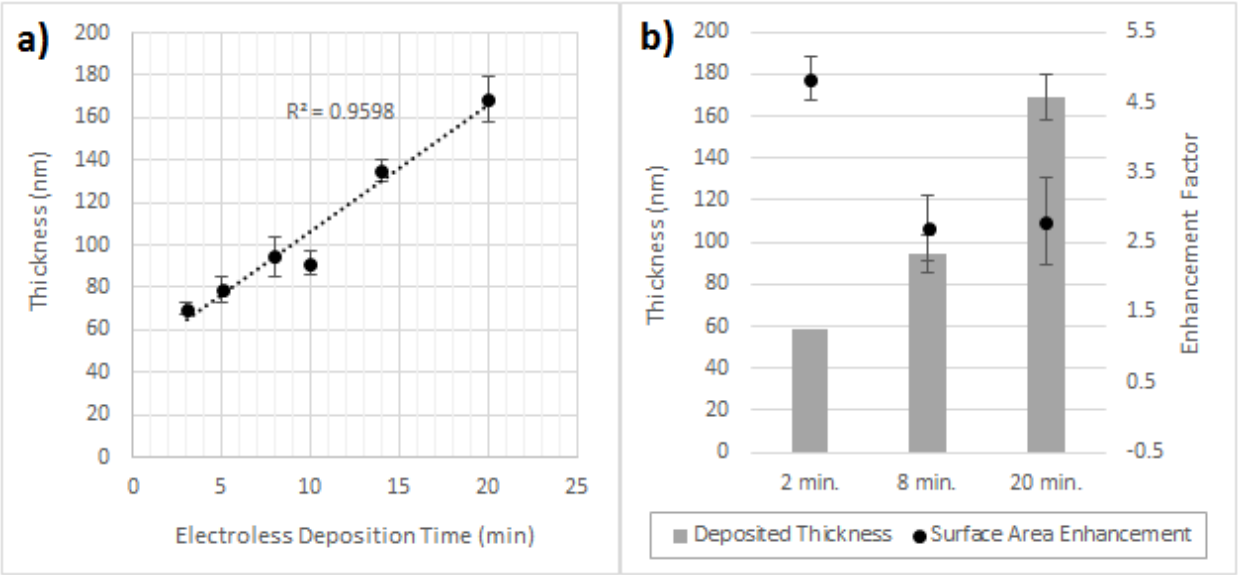

Figure 5.7 (a) The thickness of deposited gold on a glass slide as a function of the duration of electroless deposition (data collected by collaborator). (b) The surface area enhancement after shrinking for each duration indicates enhancement is not positively correlated with electroless-deposition duration.

The expected thickness of gold for 8 min. and 20 min. electrodes before shrinking are approximately 95 nm and 170 nm. Data for 2 min. was not measured, but extrapolation indicates an expected thickness less than 70 nm. Comparison of deposited thickness prior to shrinking against surface area enhancement after shrinking (5.7b) indicates that there is no positive correlation between surface area enhancement and deposition thickness.

5.2.2 Scanning Electron Microscopy

To explain the greater surface area enhancement for 2 min. deposition duration than 8 min. or 20 min., SEM analysis of WEDPE topology was performed. Results are presented in Figure 5..

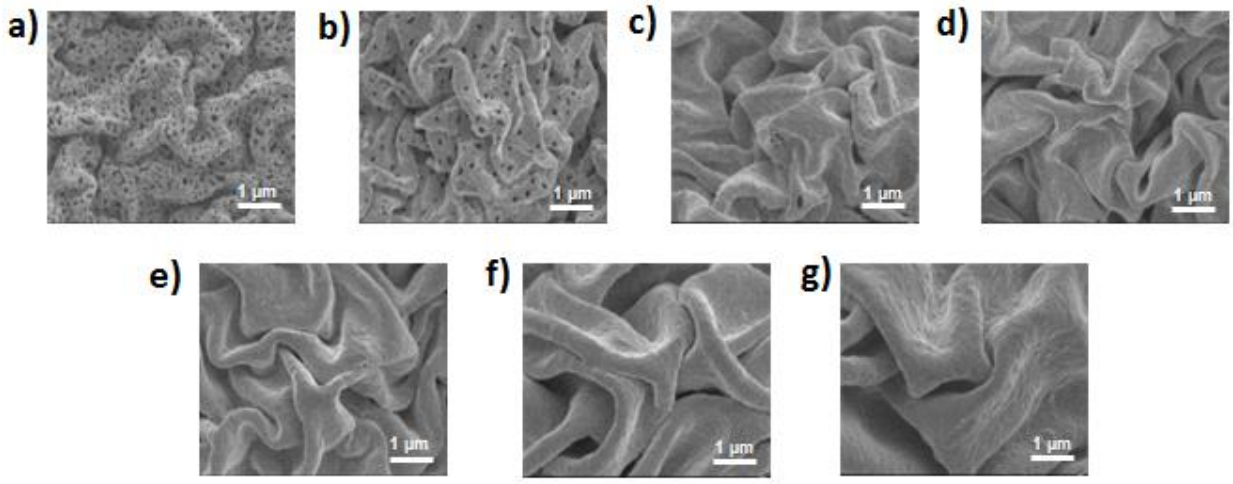

Figure 5.8 SEM images of shrunk WEDPEs (from a-g: 1, 2, 3, 5, 8, 10, and 20 mins.) illustrating the changes in topography with deposition duration (data taken by collaborator).

It is revealed that the same film wrinkling behaviour seen with wrinkled gold-sputtered electrodes exist with WEDPEs, indicating that the biaxial stress from shrinking confers to the surface film a similar texturing [96], [97]. The sizes of wrinkles increases from the nanometer-scale at shorter deposition times, and progresses to micrometer-scale with longer deposition times. However, unlike WSPEs, porosity in films is seen in electrodes, especially those deposited at shorter durations. The density of these pores (number of pores per area) is seen to decrease with increasing deposition times. This property can be attributed to the filling-in of pores with increasing deposition times, until a continuous gold film is created once all the pores have been filled. In relation to the electro-active surface areas reported in the previous section, this porosity may be the cause of a larger surface area enhancement see in 2 min. deposited WEDPEs compared to 8 min. and 20 min. WEDPEs. Although the wrinkle sizes are predominantly smaller in 2 min. devices, it is hypothesized that the porosity allows for the greater surface area enhancement than for films without porosity.

5.3 Electrochemical DNA Detection

The characterization of the previous section indicated a tunability in wrinkle size as well as the presence of porosity for electrodes deposited at most for 2 minutes. WEDPEs were tested with the electrocatalytic detection scheme (described in section 4) to gauge their functionality as DNA hybridization sensors, and to understand how structural features impact DNA sensing. Experiments were performed to understand the relation of surface-bound probe DNA density with co-deposition of probe DNA and an alkanethiol MCH (section 5.3.1) and the extent of probe density with deposition duration (section 5.3.2). WEDPEs were then evaluated based on the electroanalytical methods of CV (section 5.3.3.1) and DPV (section 5.3.3.2). Finally, a limit-of-detection experiment was performed (section 5.3.4) to determine the lowest concentration of complementary target DNA detectable by the electrocatalytic detection scheme introduced in 4.7.4.

5.3.1 [DNA]:[Thiol] Ratio on Probe Density

It has been previously shown that a co-deposition of alkanethiol spacers with thiolated probe DNA onto a sensor surface has an effect on both the amount of probe attached onto the sensor surface (allowing for the tunability of probe surface density) and the resulting spacing between attached probe DNA [143][144]. These two features impact the hybridization efficiency and electrochemical detection performance [129][97][139].

An experiment was performed on planar sputtered gold electrodes and on 2 min. and 8 min. WEDPEs to examine the effect on probe density caused by the presence of MCH in the probe deposition solution. To perform this experiment, electrodes were deposited with a certain concentration of fluorescent probe DNA such that the total thiol concentration with MCH in 1000/10 would always be kept at 5 µM. These concentrations are explicitly listed in Table 5.1.

Table 5.1 Concentrations of probe DNA and MCH for varying [DNA]:[Total Thiol]

[DNA]:[Total Thiol]	[Probe] (µM)	[MCH] (µM)
0.01	0.05	4.95
0.1	0.5	4.5
0.2	1	4
0.3	1.5	3.5
0.4	2	3
1	5	0

After a 4 hr deposition, a 1 mM MCH backfill was performed for 1 hour. Fluorescent DNA was then desorbed in 12 mM MCE, 0.3 M PB solution and quantitated by fluorescence plate reading. The results are presented in Figure 5.9 below.

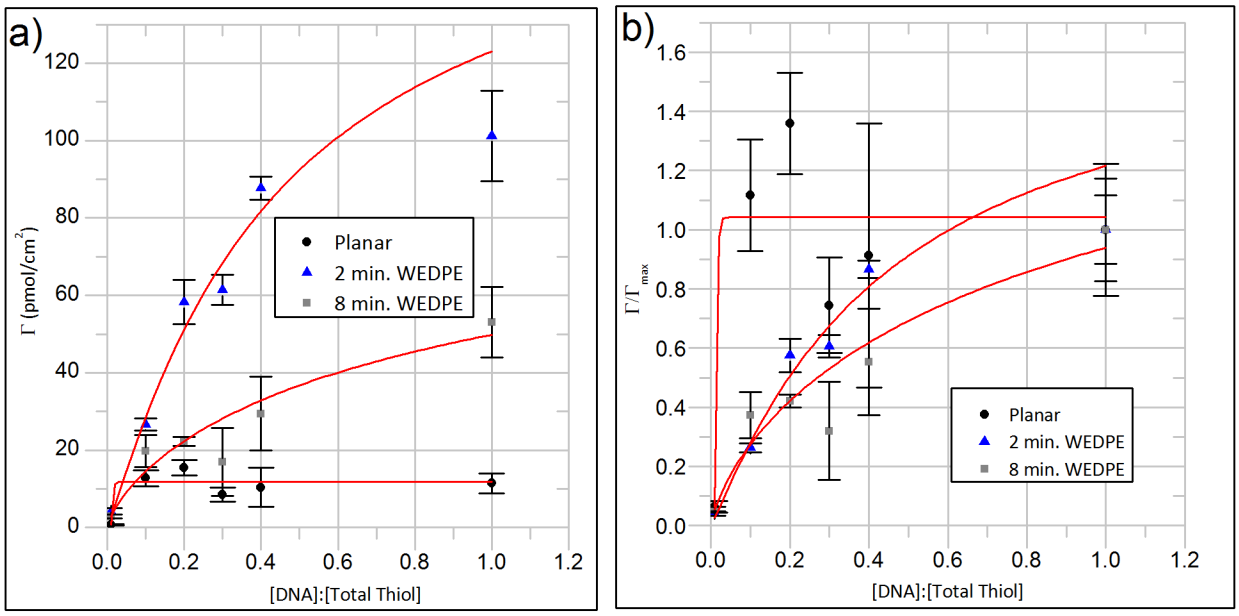

Figure 5.9 (a) Probe density of planar gold and 2 min., and 8 min. WEDPEs deposited with varying [DNA]:[Total Thiol] ratios in 1000/10 at 4 hours each, followed by a 1 mM MCH backfill for 1 hour. (b) Plot of the normalized probe density with varying [DNA]:[Total Thiol] ratio showing the approximate probe binding kinetics. Each point is an average of 3 samples. Standard error bars are shown.

Surface area measurements have shown that 2 min. devices, due to porosity, have higher surface area enhancements than 8 min., which in turn has a higher enhancement than planar surfaces. At all [DNA]:[Total Thiol] ratios, the probe density reflects this ordering. Probe densities for 8 min. and planar electrodes show a similar trend until a ratio of 0.4, whereupon further increases in the ratio does not increase the planar probe density but does increase the 8 min. density. This trend

between 8 min., and planar electrodes can be attributed to the similarity in availability for surface binding of wrinkled and planar areas until a [DNA]:[Total Thiol] of 0.4. Past this ratio, planar surfaces are saturated with probe DNA, whereas the wrinkling (and higher surface area) of 8 min. electrodes allows further probe binding upon increases of DNA concentration by 3 µM from a ratio of 0.4 to 1.

For the 2 min. electrode, the probe density behaviour is unlike that for planar and 8 min. electrodes. A much larger rate of increase in the probe density occurs until a DNA molar fraction of about 0.4, whereupon the rate increases until a fraction of 1.0, but at a slower rate. This characteristic can be ascribed to the porosity of the surface. At molar fractions below 0.4 at which the probe density increase is the largest, the additional area created by the porous structures allows the deposition of probes to proceed into these area as well as onto the wrinkled structures. Past molar fractions of 0.4, the available surface area created by these cavernous regions becomes limited as pores are filled, causing the total surface are for deposition to decrease, leading to a more gradual increase in probe density with increasing molar fraction.

The probe density behaviour of planar electrodes is in line with previous results [97][144] which report an increase in the probe density until a probe molar ratio of 0.5, whereupon the density exhibits a small decrease until a ratio of 1.0. This behaviour was attributed to the deviation away from an ordered monolayer in which MCH causes probe DNA to project perpendicular from the surface and prevents non-specific adsorption, leading to maximum density. This orderliness declines as the MCH concentration decreases which prevents maximum probe binding to occur.

5.3.2 Effect of Deposition Duration on Probe Density

Next, an experiment was performed to gain greater insight into the effect of electrode surface texturing on the binding kinetics of probe DNA on 2 min. WEDPEs, chosen for its highest probe density. Using a probe molar ratio of 1.0, which was shown to produce maximum probe density, 2 min. WEDPEs and planar electrodes were deposited with 5 µM fluorecsent probe DNA in 1000/10 for durations up to 16 hours, followed by a 1 mM MCH backfill of 1 hour. A 16 hour deposition duration was considered enough time for probe saturation of the electrode surface to occur. Results are shown in Figure 5.10 below.

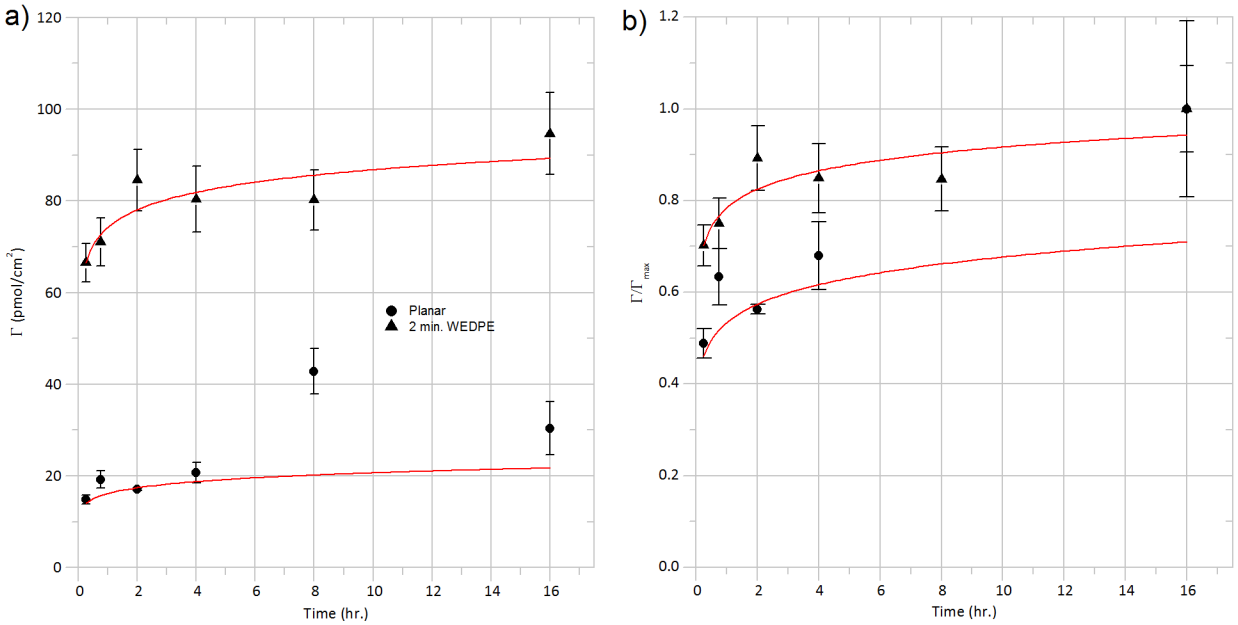

Figure 5.10 (a) Probe density as a function of probe deposition time for planar and 2 min. WEDPEs deposited with 5 µM fluorescent probe DNA in 1000/10 followed by a 1 hour backfill with 1 mM MCH. (b) Normalized probe densities showing the deposition kinetic behaviour for planar and 2 min. WEDPEs. Each measurement is an average of 3. Standard error bars are shown. Sigmoidal curves were matched to data to illustrate trends.

In reference to Figure 5.10a, the planar probe density attains a value of about 18 pmols/cm^2 at 15 min. deposition duration and gradually increases with time. A large density was seen at 8 hours, which is approximately twice the amount expected from a non-linear trend fitting of the data. This value is considered as an atypical reflection of the true density at that duration, as results from similar probe density experiments [97] do not show such a behaviour. This effect is also unlikely caused by non-specific adsorption as the probe density at 16 hours does not show this marked increase. Yet, in comparison to the planar results by Woo et. al, the maximum probe density at 16 hours is comparatively higher, as well as for densities at other durations. This is due to having a much more ideal probe molar ratio of 1.0 as compared to the experiments performed by Woo et. al who did not perform a complete filtration of MCH in the probe reduction stage. This has the effect of decreasing the amount of probe DNA for surface binding for each time point.

The 2 min. WEDPEs attain a larger density of about 63 pmols/cm^2 at 15 minutes, and as mentioned previously, the surface area enhancement allows for a greater probe density at all time points compared to a planar surface. The rate of density increase with respect to time is the

greatest at durations less than about 4 hours, whereupon the gradual increase proceeds until a maximum density of approximately 95 pmols/cm^2.

In reference to Figure 5.10b, the probe binding kinetics for each surface can be more appropriately compared by normalizing each density value with the maximum probe density at 16 hours (Γ_{max}), as such, the resulting plot indicates the rate of density growth per time until maximum density is reached. A sigmoidal curve is approximately fit to both data sets to illustrate the trend in kinetics. Comparing these two curves between planar and 2 min. WEDPE, it is evident that the rate of increase in density for 2 min. WEDPEs is great than for planar surfaces. This behaviour is not only attributed to strictly the surface area enhancement, but also reflects a topography-induced enhancement in probe binding kinetics. More specifically, the wrinkling and porosity has an effect on the way probe DNA bind to the surface which allows more DNA to bind to the surface per time, as compared to a planar surface. This enhancement is diminished for durations longer than approximately 4 hours, as the change in density between 2 min. WEDPEs and planar electrodes follow a similar trend.

5.3.3 Detection with Electrolessly-Deposited Devices

The previous experiments demonstrated that porous 2 min. WEDPEs had higher probe densities than other surface topographies and WEDPEs had higher probe densities than planar surfaces. Next, the electrochemical DNA detection protocol described in section 4 was performed on 2 min., 8 min., and 20 min. electrodes, with each of three electrodes in two groups – one group for the detection of complementary complementary target DNA, and another for control detection of non-complementary target DNA to gauge detection selectivity. All electrodes were electrochemically polished for 80 cycles. Probe DNA deposition duration was allowed to proceed overnight, followed by a MCH backfill duration of half an hour. Target DNA deposition was allowed to proceed overnight. These conditions were implemented to allow for the most favorable conditions for initial testing of DNA hybridization sensing capability.

5.3.3.1 Cyclic Voltammetry Results

Cyclic voltammetry was performed for 2 min., 8 min., and 20 min., WEDPEs to understand the impact of changes to electrode topography on surface-mediated redox reactions, more specifically, how the creation of a DNA and MCH monolayer on the electrode surface effects the access of redox couple FoCN/FiCN to/away from the electrode surface. The resulting scans are presented in Figure 5.11 below.

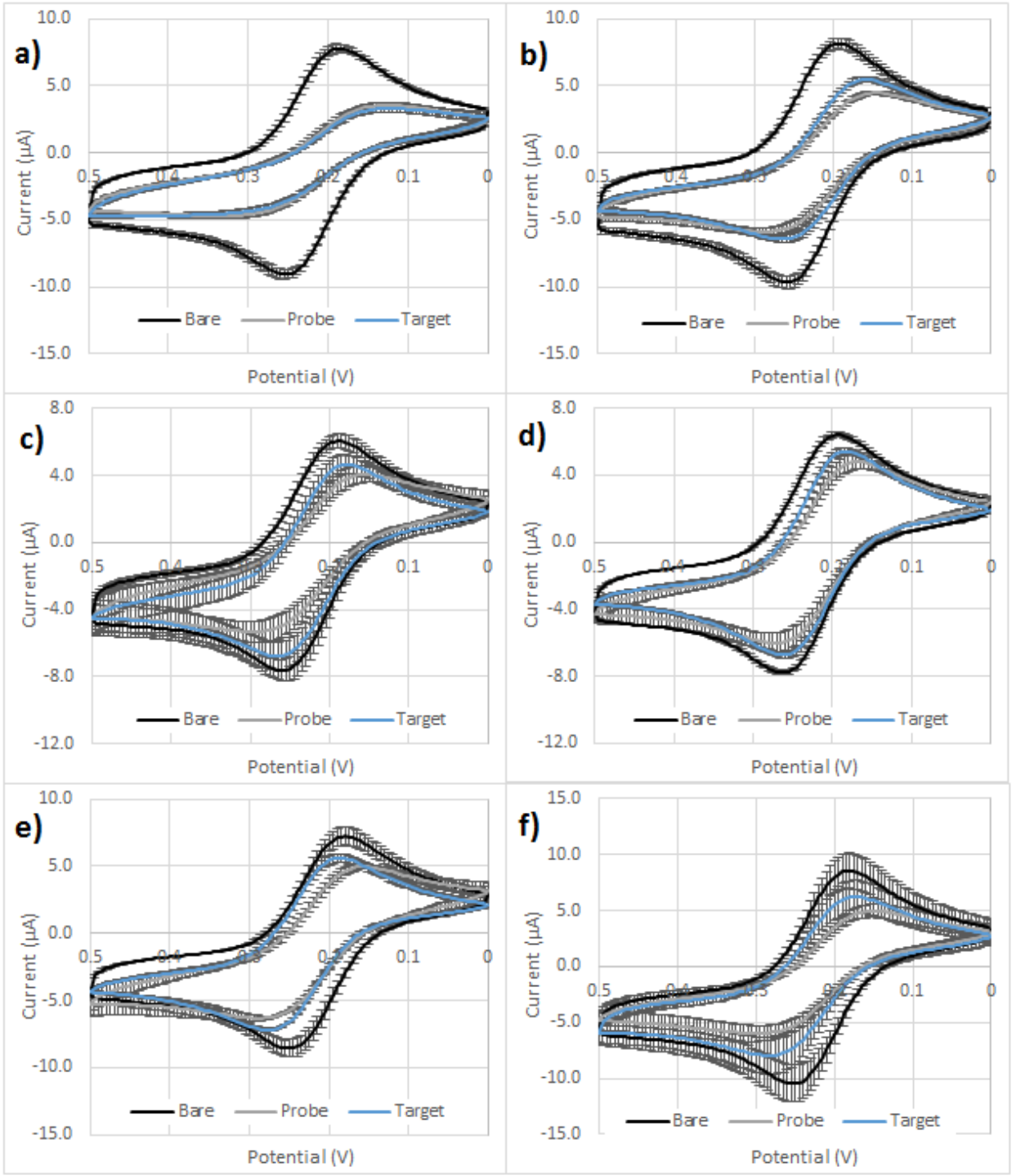

Figure 5.11 Overlays of cyclic voltammograms taken of 2 min. (a-b), 8 min. (c-d), and 20 min. (e-f) WEDPEs at bare surface states, following overnight probe deposition of 5 µM probe DNA in 1000/10 and 1 hr backfill of 1 mM MCH, and following target deposition (complementary DNA are shown on the right column, non-complementary on the left) overnight at 37 degree Celsius in 1000/10. All scans are an average of 3, with standard error bars showing the reproducibility between scans.

All bare scans show clear reduction and oxidation peaks for all WEDPEs and resembles the behaviour of planar electrodes (section 4.7.3). The reduction and oxidation peak-to-peak differences for bare, probe, and target hybridized states are compared in the slope charts in Figure 5.12 below.

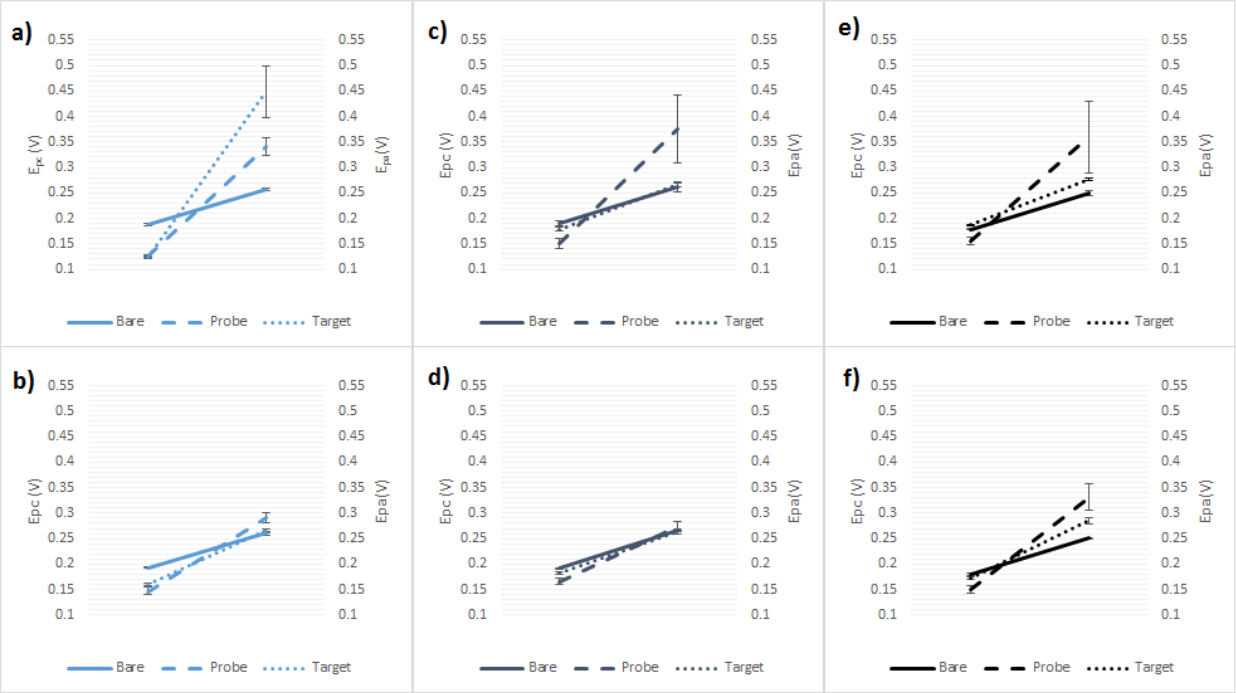

Figure 5.12 E_{pc}, E_{pa}, and E_{p-p} (slope) for bare, probe, and target states for (top row) complementary and (bottom row) non-complementary 2 min. (a-b), 8 min. (c-d), and 20 min. (e-f) WEDPE DNA detection. Standard error for 3 average scans are shown.

Bare scans for all WEDPEs exhibit good reproducibility for all deposition timings. As indicated in Figure 5., E_{pc} and E_{pa} for all electrodes show little variability. The average E_{pp} (slope of the line) for all bare electrodes is 0.070±0.002 V which indicates greater reaction reversibility than for the bare electrode (0.076 V) tested in section 4.7. Upon probe deposition and MCH backfill, the E_{p-p} is expected to increase indicating a decline in reversibility due to electrode surface blocking. This trend is seen for all electrodes but is most evident for 2 min. and 8 min. complementary electrodes and in 20 min. electrodes. This is considered to be caused by the variation in probe density for electrodes, as indicated by the larger error bars for E_{pa} values. Interestingly, corresponding E_{pc} values show a much smaller variation between electrodes of the same group. Upon complementary target DNA hybridization, the E_{p-p} is expected to increase further while exposure to non-complementary DNA should cause little to no change. This is only

evident for 2 min. WEDPEs while other electrodes, irrespective of exposure to complementary or non-complemtary DNA, show a decrease. This decrease indicates an increase in reaction reversibility caused by additional defect regions in the monolayer where additional bare gold is exposed. An overnight exposure of the monolayer to the ionic content of the deposition buffer may allow additional non-specifically absorbed probe DNA on the surface to be removed revealing bare gold.

In a similar manner, the I_{pa}, I_{pc}, and I_{pp} results are summarized in Figure 5.13 below.

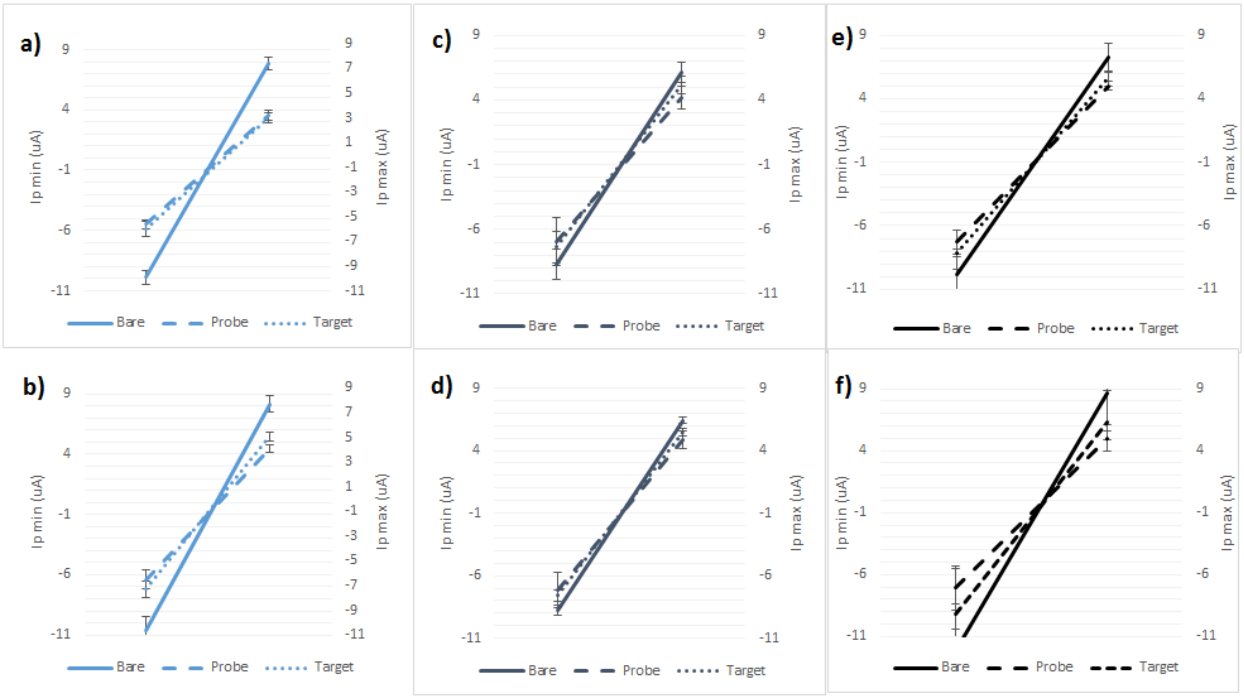

Figure 5.13 Summary of I_{pa}, I_{pc}, and I_{pp} (slope) of electrodes for complementary (top row) and non-complementary (bottom row) cyclic voltammograms for 2 min. (a-b), 8 min. (c-d), and 20 min. (e-f) WEDPEs. Each is an average of 3 scans. Standard error bars are shown.

As indicated in section 5.2, the surface area enhancements for WEDPEs of the same projected surface area are the greatest for 2 min., followed by 20 min., and 8 min. This is expected to be reflected in the current peak values, with I_{pa} and I_{pc} magnitudes being larger for electrodes of greater enhancement. This trend is seen in the bare scans for 2 min. and 8 min. WEDPEs, but not for 20 min, which show larger errors in peak current values. This could be caused by the electrodes within the non-complementary set having varied surface areas owing to incomplete blocking of the portions of the connector (section 5.1) with glue.

Upon addition of probe DNA and MCH, the peak currents are expected to decrease due to the decrease in the accessibility of FoCN able to the bare surface causing a decrease in faradaic current. This behaviour is seen for all electrodes (figure 5.13) as indicated by the decrease in the slope (difference between current peaks) of the probe line as compared to that for the bare. This change in the peak current is most evident for 2 min. (figure 5.13a-b) WEDPEs and is attributable to surface porosity allowing for the greatest probe density compared to other WEDPEs and planar surfaces.

5.3.3.2 Differential Pulse Voltammetry Results

Following CV, DPV of electrodes were conducted in a solution of 25 mM PB solution, 25 mM NaCl, 27 µM RuHex, and 2 mM FiCN to specifically detect the presence of probe and target DNA at the electrode surface using the electrocatalytic detection scheme presented in section 4.7.4. Briefly, RuHex will electrostatically bind to the polyanionic DNA backbone at a stoichiometric ratio of 1 RuHex molecule to 3 phosphate groups. A faradaic current will be generated from the reduction of RuHex which is amplified from the replenishing of RuHex back to the oxidized form by FiCN, allowing it to be repetitively reduced.

Representative scans for each of 2 min., 8 min., and 20 min. WEDPEs are shown in Figure 5.14 below. The standard error bars shown demonstrate the reproducibility of the DPV scans per electrode.

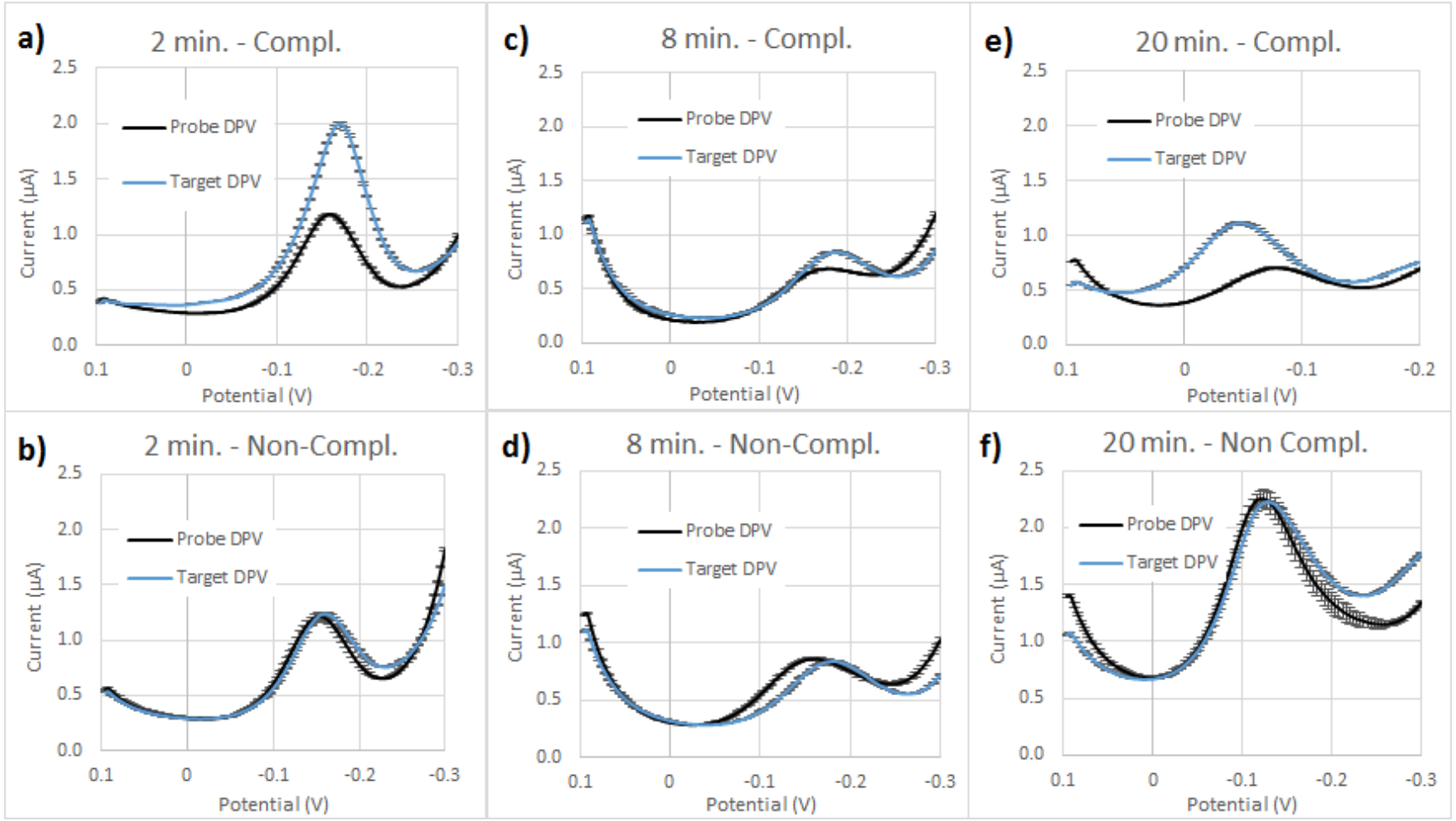

Figure 5.14 DPVs for complementary (Top) and non-complementary (Bottom) DNA hybridization detection for 2 min. (a-b), 8 min. (c-d), and 20 min. (e-f) WEDPEs following deposition of probe DNA and MCH backfill. Each scan is an average of 3 scans. Standard error bars are shown.

All WEDPEs exhibit low non-complementary target detection as evidenced by a small % change in background-adjusted current peaks following probe deposition (Figure 5.14, bottom row). A more significant change in current peaks can be seen for all scans following introduction of complementary target DNA. A shift in the peak potentials is seen for 8 min. and for 20 min. WEDPE complementary target DNA scans. This is likely due to an anomalous shifting in the reference potential of the Ag/AgCl electrode upon DPV acquisition. A summary of the average percentage peak changes are given in Figure 5.15.

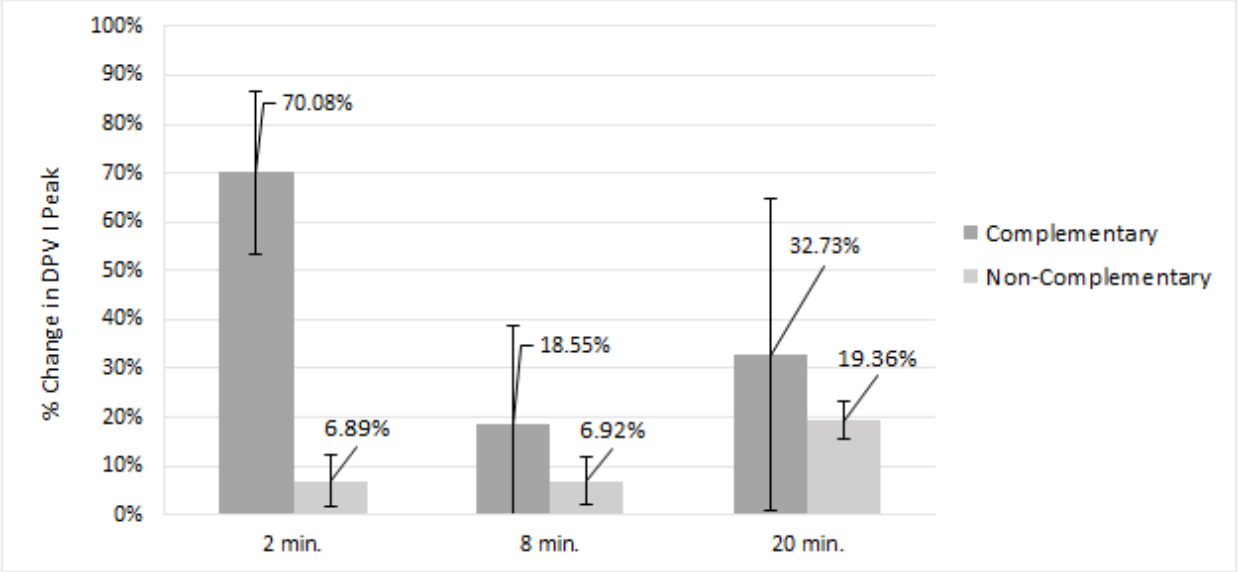

Figure 5.15 Average % change in peak currents for complementary and non-complementary DNA detection of 2 min., 8 min., 20 min. WEDPEs. Each indicates an average of 3 devices. Standard error bars are shown.

Average percentage peak changes for complementary and non-complementary DNA sensing are 70.08%±16.69% and 6.89%±5.36%, 18.55%±20.02% and 6.92%±4.80%, and 32.73%±31.93% and 19.36%±3.93% for 2 min., 8 mins., and 20 min., WEDPEs. The exposure to complementary target DNA causes a large variation in the DPV response of individual electrodes, as reflected in the error. Despite this variation in probe density, 2 min. WEDPEs indicate the largest response to complementary target DNA hybridization and the lowest non-complementary DNA target detection. It is concluded that the porous nature of 2 min WEDPE surfaces creates a greater surface area enhancement leading to a greater probe density and greater signal change when performing electrocatalytic DNA hybridization detection with DPV.

5.3.4 Limit of Detection Study

Results from the previous DNA electrochemical detection experiment indicate that 2 min. devices allow the largest % DPV signal change upon complementary detection and the lowest % change upon non-complementary detection. Next, a limit-of-detection test, as described in section 4.7.6, was performed for 2 min. WEDPEs to measure the lowest concentration of target DNA able to be detected by the electrocatalytic DPV detection method.

To perform this experiment, six 2 min. WEDPEs were deposited with 10 µM of probe DNA overnight, followed by a 30 minute MCH backfill. Three of these electrodes were used to detect 1 uM non-complementary DNA to gauge the background signal, and the other three were used for complementary target DNA detection. Electro-active surface area of electrodes were gauged to ensure surface areas between electrodes were uniform and were in range with surface areas measured in Figure 5..6. The results of the LOD experiment are shown in Figure 5.16 below.

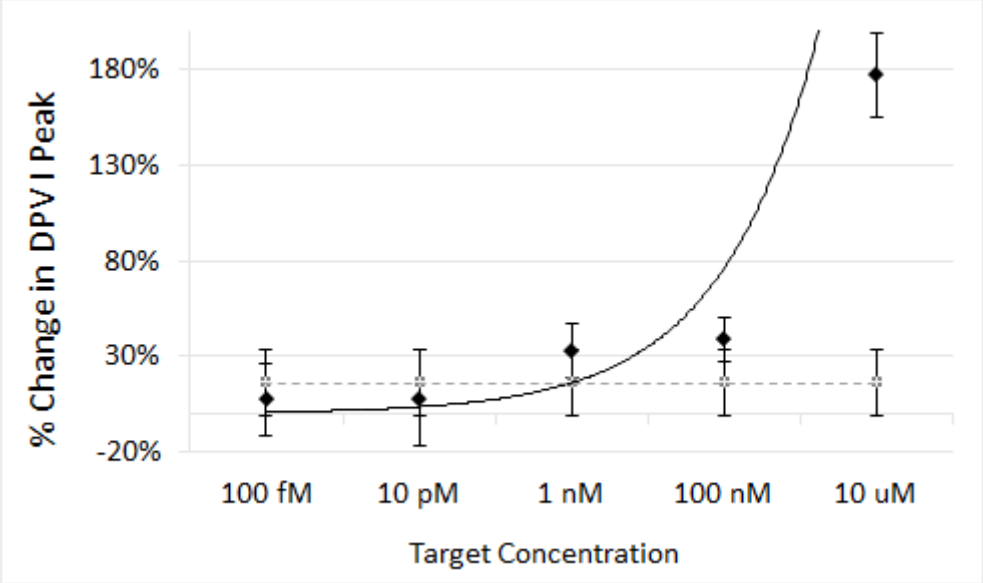

Figure 5.16 The % change in DPV I signal with 100x concentration changes of complementary target DNA. The grey dotted line indicates the background signal. Each point is an average of 3 scans. Standard deviation bars are shown.

The LOD for 2 min. WEDPEs was determined to be 10 µM with a background signal of 16.52%. This LOD is 1 order of magnitude greater than the LOD obtained previously for 100 nm WESPEs (1 µM) [97], although a smaller concentration difference (10x) was used in the LOD

experiment compared to the difference (100x) used in this work. It is likely that the true LOD is in fact less than 10 μM if a finer concentration difference were to be used.

In the context of literature, two groups have performed similar studies of DNA electrochemical detection with porous electrodes and have reported detection limits. Hu et. al [145] performed DNA electrochemical hybridization detection with nanoporous gold electrodes created by nitric acid de-alloying of silver/gold alloys. An LOD of 28 aM was reported with CC detection of RuHex, although this method employed a signal amplification strategy employing a bio bard code scheme. Briefly, reporter strands with a Au-NP modified with ~100 ssDNA hybridizes to the complementary strands allowing greater electrostatic attraction of RuHex and ensuing electrochemical signal generated. The nanoporous electrodes used had an electro-active surface area enhancement of 9.2 compared to planar.

Daggumati et. al [146] also created porous electrodes from a similar nitric acid de-alloying process by first co-sputtering silver and gold onto layers of gold and chrome on a glass slide. Thermally unannealed porous electrodes exhibited a similar surface area enhancement factor (9.26) of that achieved by Hu et. al. Square-wave voltammetry was used with both annealed and unannealed electrodes to perform hybridization detection of 26mer DNA using methylene blue as a redox reporter. Annealed electrodes demonstrated a dynamic range between 0.5 to 10 nM.

In this work, the surface area enhancement for 2 min. WEDPEs (4.84) is in between those demonstrated by Daggumati et. al for annealed and unannealed electrodes, and lower than those by Hu et. al. The LOD achieved by 2 min. WEDPEs (10 μM) is higher than the annealed electrodes demonstrated by Daggumati et. al of 0.5 nM, if this is considered the LOD, although a satisfactory comparison cannot be made for two reasons: a signal amplification strategy was employed and a broad concentration difference was used for the LOD experiment (yielding a higher LOD of 10 μM). These results demonstrate the potential attractiveness of using 2 min. WEDPEs for electrochemical DNA detection owing to the use of fabrication techniques which do not require sputtering and de-alloying of metals, and the likelihood of a lower LOD than 10 μM upon repeating the LOD experiment using finer concentration differences.

Other groups have also demonstrated the use of porous electrodes for electrochemical DNA detection. Rho et. al [147] performed hybridization sensing with nanoporous niobium oxide

electrodes with CV of methylene blue; however, the lowest concentration of complementary target tested was 1.5 μM and an explicit LOD test was not performed. De la Escosura-Muñiz et. al [148] used an anodized aluminum oxide nanoporous membrane in conjunction with a screen-printed transduction layer for the detection of target DNA with and without Au-NP modification. The LOD determined was 6.5 μM of 21mer DNA. Takmakov et. al [149] demonstrated the use of hydrothermally treated anodized alumina membranes for impedimetric sensing of DNA but did not report the concentration of target DNA used.

5.4 Conclusion

This section presented a new rapid-fabrication technique which provides an alternative to the use of vacuum sputtering technology in favor of an all-solution processed gold deposition technique. Retaining the use of pre-stressed polystyrene substrates, topographical tuning of microscale wrinkling is shown, as well as the introduction of pores within the wrinkled structure which was shown to contribute to an enhancement of surface area for electrodes. These electrodes were then shown to have potential to be used as electrochemical DNA hybridization sensors, demonstrating the ability of 2 min. WEDPEs for electrochemical hybridization sensing of complementary target DNA to 10 μM concentration.

6.0 Development of a Hybridization Efficiency Characterization Method

This chapter describes the development of a method to determine hybridization efficiency of DNA hybridization sensors, bringing together two classes of techniques – one for the determination of captured target density and another for the determination of probe density – such that both measurements can be performed in the same experiment. A literature review will first be given describing previously reported methods of hybridization efficiency characterization and their associated limitations (section 6.1), followed by a description of the development of the proposed novel characterization scheme (section 6.2, 6.3, and 6.4) which addresses the aforementioned limitations. This scheme is then used to characterize hybridization efficiency of planar, 100 nm and 200 nm WSPEs and (section 6.5),

6.1 Literature Review

The measurement of hybridization efficiency provides a quantitative count of the number of complementary target DNA captured by probe DNA, and allows for an understanding between the transduced signals for hybridization detection to the actual number of DNA participating in the capturing process. This characterization also provides insight into the role of electrode structuring on the changes to probe DNA binding and target captured as compared to a strictly planar surface.

Several groups [150] have used the electrochemical method developed by Steel et. al [139] to detect the differences in redox charge associated between RuHex electrostatically attracted to ssDNA and to hybridized duplex DNA; however, this technique is restricted for use with only planar surfaces due to the method's assumption of diffusive flux to a planar surface. Lao et. al [151] and Cho et. al [152] performed hybridization efficiency of thiol-modified 20mer oligonucleotides on gold surface with an MCH backfill procedure with Quartz Crystal Microbalance (QCM), but Cho et. al concluded that QCM results, as compared to fluorescence detection, resulted in overestimates of the true density.

Peterson et. al [153] examined the hybridization efficiency of thiolated 25mer oligonucleotides on planar gold substrates with Surface Plasmon Resonance (SPR). Likewise, Nelson et. al [154] performed SPR analysis of 18mer hybridization on planar gold surfaces. Although SPR studies

of hybridization efficiency have been conducted on planar surfaces, no similar studies have been performed for wrinkled or porous electrodes. It is uncertain if SPR characterization of hybridization efficiency is permitted for these electrodes, especially for determining probe and target DNA densities in cavernous regions within the bulk electrode structure which may be accessible to DNA and other molecules in solution, but not to light.

A method based on the desorption of Au-thiolated bound fluorescent-modified DNA molecules by alkanethiols and measuring the ensuing fluorescence[155] in solution is a widely used technique[156][97][157][144] to perform hybridization efficiency studies. Using this method, the probe density is determined by desorbing fluorescent-modified DNA from the electrode surface. The target density is determined by measuring fluorescent-modified target DNA which is either separated from the probe DNA or is measured still in the duplex form which was desorbed from the surface. As such, the determination of probe and target densities necessitates at least two electrodes to be processed – one for the determination of probe density and another for the determination of target density, which leads to the loss of electrode specificity. This measurement technique may also yield inaccurate results owing to slight differences in surface structuring between electrodes of the same design.

Due to the inapplicability of electrochemical methods for determining hybridization efficiency for non-planar electrodes, as well as the difficulty which SPR analysis may encounter in interrogating probe and target DNA in complex porous structuring and cavernous regions, this chapter is dedicated to the investigation of a scheme for hybridization efficiency characterization which would achieve the following:

I. Label-free method of measuring hybridization efficiency of DNA

II. The direct determination of hybridization efficiency by sequential measurement of probe and target densities for the same electrode, instead of relying on average values from multiple experiments

III. Development of a versatile method that is applicable to surfaces with planar and non-planar structures including 3D and high topography structures.

6.2 Preliminary Hybridization Efficiency Measurement

Initially, a hybrid electrochemical/fluorescence method was developed to determine the hybridization efficiency of planar gold. This method utilizes electrochemical readout using chronocoulometry (CC) to determine the probe density and fluorescent-modified complementary target DNA to indicate duplex density. For this measurement, six planar gold macro-electrodes were deposited with a 20mer thiolated probe DNA in a 1000/10 buffer overnight followed by a 1 hour MCH (1 mM) backfill to passivate the surface of non-modified gold and to achieve the ideal vertical orientation of the probe monolayer. CC scans were performed on these electrodes with the protocol described in section 4.6 and probe densities were determined. Three electrodes were then deposited with fluorescent complementary target DNA and three electrodes were deposited with non-complementary fluorescent DNA in 1000/10 to serve as controls. Target hybridization was allowed to proceed overnight at 37 degree Celsius followed by a desorption of all thiolated molecules in MCE using the protocol developed by Demers et. al [155]. Fluorescence measurements were then taken to determine the amount of fluorescent target DNA bound. Figure 6.1 below shows the results of the DNA hybridization detection experiment of complementary and non-complementary target DNA.

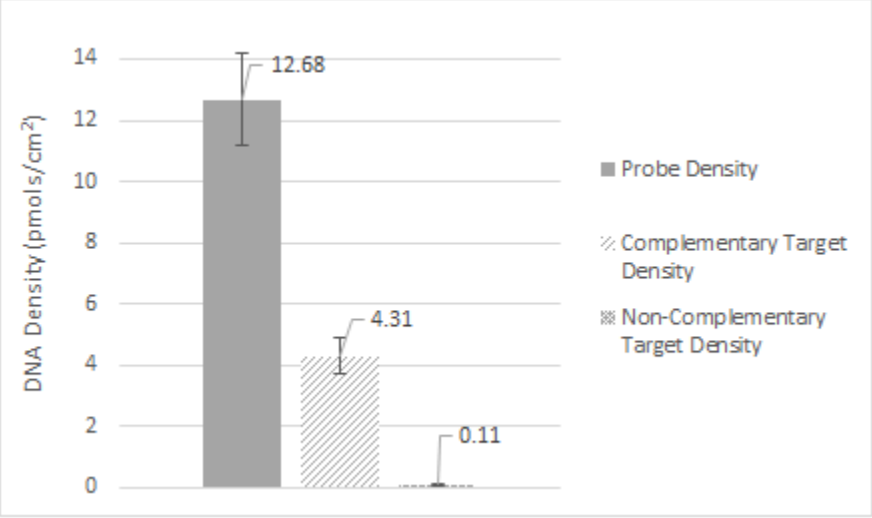

Figure 6.1 Hybridization efficiency for planar Au macro-electrodes. Probe density was determined from electrochemical Anson plot analysis and target densities were measured by fluorescence reading.

Table 6.1 A sample of probe/target DNA quantification experiments for Au surfaces using difference characterization techniques reported in literature

Group	Characterization Technique/Substrate	Density Results
Woo et. al, 2014	• **Fluorescence** detection of β-mercaptoethanol desorbed fluorescein-modified probe 20mer DNA on planar Au, 20 nm, 100 nm, and 200 nm WSPEs*	• **Probe density** vs. time, 1 hr. 1 mM MCH: planar max density ≈ 20 pmols/cm^2; 200 nm WSPE max density ≈ 59 pmols/cm^2 • **Probe density** vs. [DNA:Total Thiol], 1 hr. 1 mM MCH = 1.0 for 4 hr. dep.: planar max density ≈ 12 pmols/cm^2; 20 nm WSPE max density ≈ 38 pmols/cm^2, 100 nm WSPE max density ≈ 45 pmols/cm^2, 200 nm WSPE max density ≈ 55 pmols/cm^2
Castelino et. al, 2005	• **Fluorescence** detection of β-mercaptoethanol desorbed fluorescein-modified probe 10mer, 20mer, 30mer, 40mer probe DNA on planar Au • Fluorescein-modified 10mer, 20mer, 30mer complementary target DNA	• **Probe density** vs. [NaCl] = 1M in dep. buffer for 24 hr. dep., no backfill: 40mer max density ≈ 11 pmols/cm^2; 30mer max density ≈ 12.5 pmols/cm^2; 20mer max density ≈ 18 pmols/cm^2; 10mer max density ≈ 20 pmols/cm^2 • ***Hybridization density*** (2 µM targets) vs. [NaCl] = 200 mM, 24 hr. dep, no backfill: 30mer max density ≈ 4 pmols/cm^2; 20mer max density, [NaCl] = 500 mM ≈ 5.5 pmols/cm^2; 10mer max density ≈ 6.6 pmols/cm^2 • ***Hybridization efficiency*** vs. Probe Density, 24 hr. dep, no backfill: 30mer max efficiency ≈ 75% at 3.3 pmols/cm^2 probe density; 20mer max efficiency ≈ 60% at 6.6 pmols/cm^2 probe density; 10mer max efficiency ≈65% at 8.3 pmols/cm^2 probe density
Steel et. al, 1998	• **Electrochemical quantitation** (chronocoloumetry of RuHex) of 25mer probe and target DNA on planar Au	• **Probe density** vs. time, 1 hr. 1 mM MCH, 1 uM probe dep.: mixed base 25mer max density ≈ 10 pmols/cm^2 (250 min.), poly-T 25mer ≈ 17 pmols/cm^2 (250 min.) • ***Hybridization density*** vs. probe density, 1 uM target dep. 60 min.: mixed based 25mer max density ≈ 6 pmols/cm^2 (6.6 pmols/cm^2 probe density), poly-T 25mer ≈ 8.8 pmols/cm^2 (15 pmols/cm^2)
Cho et. al, 2004	• **Fluorescence** detection of 3-mercaptopropanol desorbed fluorescein-modified 15mer probe	• **Probe density** by fluorescence ≈ 7 pmols/cm^2 deposited with 0.58 uM 1xTE buffer, 1 M NaCl; 1 mM MCH for 1 Hr.) • ***Hybridization efficiency*** ≈ 60% (4.3 pmols/cm^2)

*WSPEs = wrinkled, gold sputtered polystyrene electrodes

A maximum probe density of 12.69 ± 4.47 pmols/cm^2 was determined. Of this density, 4.31 ± 1.4 pmols/cm^2 complementary targets were detected. This leads to a hybridization efficiency of 34%. A low contribution of non-complementary target (0.11 ± 0.05 pmols/cm^2) was detected. These densities are in range with those reported in literature using similar quantitation methods (Table 6.). For example, Steel et. al [139] reported a maximum probe density of approximately 10 pmols/cm^2 for planar gold using electrochemical Anson plot analysis of 25mer DNA. Castelino et. al [156] reported a target density of 5.5 pmols/cm^2 for 20mer DNA. As indicated in the results reported in Table 6., different groups report a range of probe densities between about 10-25 pmols/cm^2 and target densities between about 1-10 pmols/cm^2 for planar gold surfaces. This variation of values reported between groups exists due to the differences in deposition conditions (duration and buffer components) [152], DNA length [156], and quantitation method employed.

The method described previously permits the measurement of probe and target densities per electrode, which allows for the determination of hybridization efficiency for individual electrodes. Unfortunately, the determination of probe density by CC cannot be used for structures other than planar surfaces due to technique's assumption (section 4.5.1) that redox-active molecules are diffusing to a strictly planar surface. For more complex surfaces, such as those containing wrinkled and porous structures, other methods for hybridization efficiency measurement need to be investigated.

To overcome the limitations of the structure-dependent electrochemical method described above, two additional methods were explored for the quantification of probe density. Both of these are based on desorption of probe molecules labelled with a fluorescent tag. Exposure of a thiol-attached monolayer to MCE allows the displacement of surface-bound probes in exchange for MCE surface-binding. Fluorescence detection of desorbed ssDNA probe in solution is then carried out [155]. A secondary method explored, as demonstrated by Wang et. al [158] utilizes chronoamperometry (CA) to supply a constant potential across the monolayer which is adequate to disrupt thiol-Au bonding. Figure 6.2 presents DPV data showing this monolayer desorption. DPV scans were collected after a 5 μM probe DNA deposition overnight in 1000/10 and 1 hour backfill of 1 mM MCH. Complementary target DNA (μM in 1000/10) was then deposited onto a planar gold surface and DPV scans were taken. CA was performed in a 2-electrode setup applying -2.0 V (vs. Ag/AgCl) for 5 minutes in a 0.05 M PB solution.

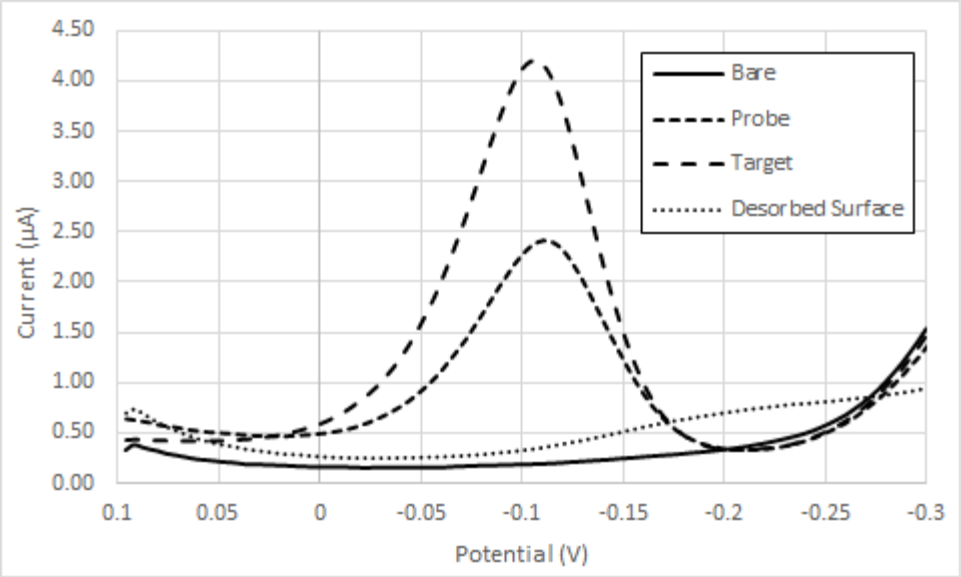

Figure 6.2 The effect of electrochemical monolayer desorption on the electrocatalytic signal. DPV scans were recorded at the bare electrode state, after probe and MCH deposition (5 µM probe DNA in 1000/10 overnight, 1 mM MCH for 1 hour), after complementary target deposition (1 µM complementary target DNA in 1000/10 overnight), and after electrochemical monolayer desorption (2-electrode CA, 2.0 V vs. Ag/AgCl).

A DPV scan was performed following CA and indicates an absence of an electrocatalytic peak, indicating the removal of DNA from the electrode surface and a return to a bare-like state.

Although displacement by an applied constant potential was shown to be adequate to remove surface-bound probes, the MCE method was chosen due to it being a passive method which eliminates the use of active electrochemical components and is more amenable to batch processing.

6.3 Duplex DNA Denaturation

The denaturation, or separation of dsDNA into its ssDNA components, is a typical requirement of common molecular biology techniques. In PCR, heat is increased past the melting temperature of duplex DNA to separate template strand and copied strand, such that successive cycles allow primers and DNA polymerase to duplicate DNA from these separated strands. In denaturing gel electrophoresis, a sample of protein or DNA is treated with a denaturing agent such as NaOH or urea to unravel secondary, tertiary, or quaternary structure such that identification of protein and DNA are based strictly on linear length. In a similar manner, these denaturing agents, specifically urea (section 6.3.1) and NaOH (section 6.3.2), were evaluated for use in denaturing hybridized target DNA on gold sensor surfaces to replenish the probe monolayer.

6.3.1 Urea

An experiment was performed to evaluate the denaturation of duplex DNA captured on a planar sensor surface subjected to urea and NaOH by comparing the similarity of DPV responses to probe-MCH monolayer DPVs and evaluating percentage differences. It is expected that a negligible difference will occur between probe DPV and DPV response after electrode exposure to the denaturants, as only complementary target DNA should be removed without modification to the probe monolayer, causing RuHex to interact with the polyanionic probe DNA in the same manner as with the inital probe monolayer DPV scan. As such, 6 macro-electrodes were deposited overnight with 10 uM probe DNA in 1000/10 followed by a 1 hour MCH backfill. Complementary target DNA was then deposited overnight in 37 degree Celsius. Bare, probe, and target DPVs were recorded as before. Electrodes were then subjected to 8 M urea followed by DPV acquisition. DPV results of the aforementioned scans are presented in figure 6.3 below with a summary of current peaks presented in Figure 6.3.

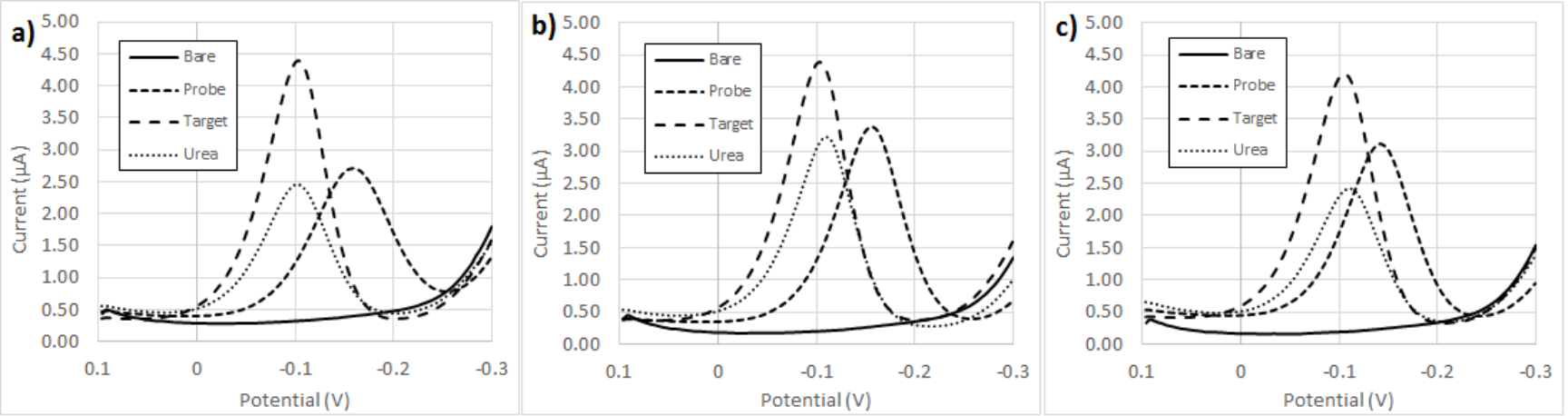

Figure 6.3 Denaturation of duplex DNA in urea. The differential pulse voltammogram of three different macro-electrodes (a-c) are displayed before and after probe deposition, after hybridization with 1 µm complementary DNA, and after treatment with 8 mM urea for 30 minutes. The DPV scans are obtained in solutions containing 25 mM NaCl, 25 mM PB solution, 27 µM RuHex, and 2 µM FiCN

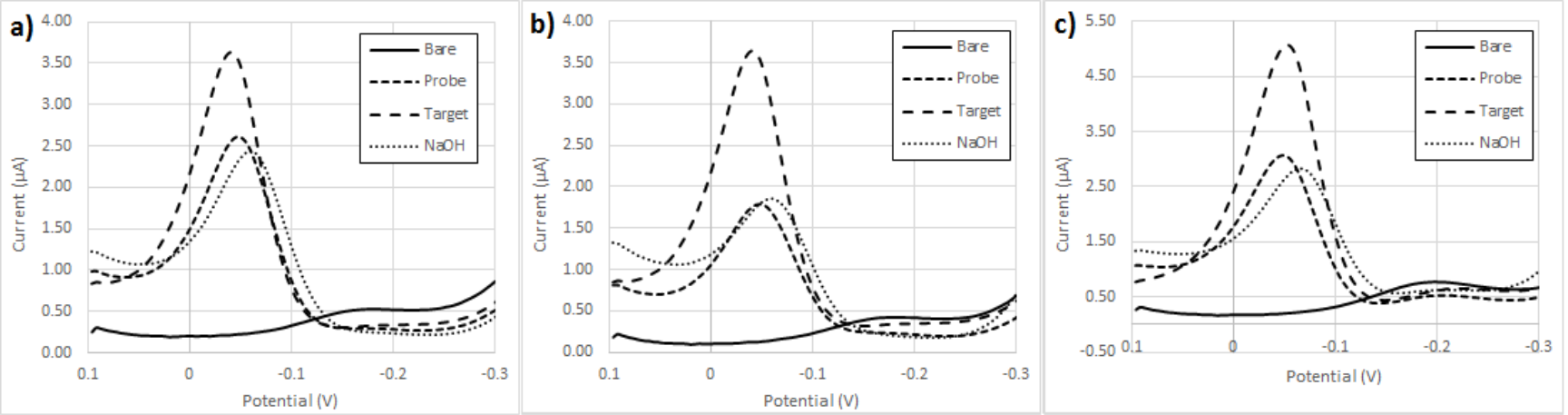

Figure 6.4 Denaturation of duplex DNA in NaOH – The differential pulse voltammogram of three different macro-electrodes (a-c) are displayed before and after probe deposition, after hybridization with 1 µm complementary DNA, and after treatment with 50 mM NaOH for 6 hours. The DPV scans are obtained in solutions containing 25 mM NaCl, 25 mM PB solution, 27 µM RuHex, and 2 µM FiCN.

In reference to Figure 6.3, all bare scans show an absence of catalytic current peaks which indicate the absence of charged DNA at the electrode surface. The positively-charged redox reporter RuHex is not electrostatically-bound and thus an electrocatalytic signal cannot be generated. Current peaks are evident for probe scans and indicate the presence of surface-bound probes. A shift in the peak potentials is also seen in comparison to the peak potentials for other scans. This shift in potential is attributed to a shift in the reference potential during measurements and does not reflect a probe-dependent phenomenon. The larger magnitude of the target electrocatalytic peaks indicate a greater negative charge on the electrode surface and is attributed to the formation of duplex DNA from complementary target hybridization. Following the urea denaturation, the current peak is expected to be equal to the probe current peak indicating the removal of target DNA from the surface monolayer.

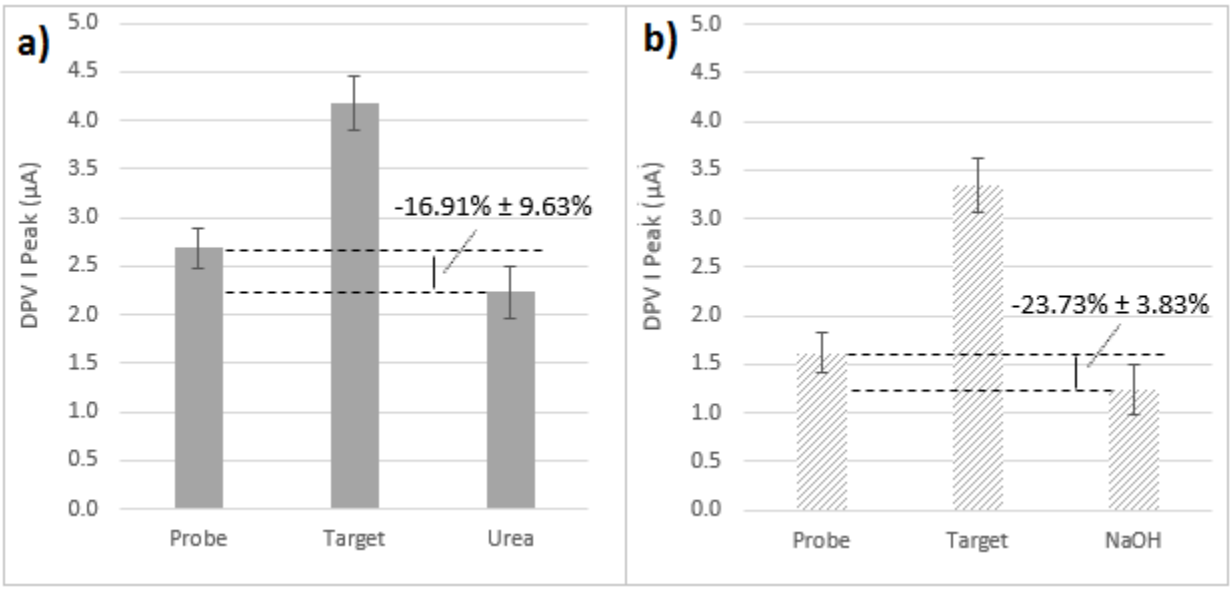

Figure 6.5 Average DPV current peaks of probe, target, and denaturation scans shown in Figures 6.3 & 6.4. The percentage change between probe and urea (a) and between probe and NaOH (b) scans are shown. Standard error bars are shown.

In reference to Figure 6.5a, the average % difference between probe and urea scans is -16.91%±9.63%. All background-adjusted peaks for urea scans are lower in magnitude than those for probe DPV scans. It can be inferred that duplex DNA was denatured indicated by the reduction in target DPV peaks for all electrodes. The negative % changes compared to probe DPV scans suggests the removal of probe DNA, assuming that the attraction of RuHex to the polyanionic backbone is unchanged between probe and urea scans. The mechanism by which

urea denatures double-stranded DNA is the competitive exchange of the hydrogen bonding between purines and pyrimidines of DNA to the functional groups of urea, which destabilizes the duplex structure.

The magnitude of the DPV signal peak after the urea treatment reduces to a value below the original peak obtained from an untreated probe monolayer. Following denaturation of the duplex structure with urea, probe DNA still tethered to the Au surface may have urea molecules hydrogen bonded to the exposed bases. These residual urea molecules may affect the electrocatalytic detection by either hindering the access of RuHex molecules to the phosphate groups or the distribution and access of FiCN/FoCN to/away from RuHex.

6.3.2 NaOH

In a similar manner, NaOH was tested as another candidate to perform duplex denaturation of hybridized DNA on sensor surfaces. Three gold planar macro-electrodes were deposited with 10 uM probe DNA in 1000/10 for 4 hours followed by a 1 hour backfill of 1 MCH. Complementary target DNA was then deposited for 1 hour in 37 Celsius. Using the same NaOH concentration for duplex denaturation as reported by Demers et. al [155], electrodes were then subjected to 50 mM NaOH for 6 hours for the denaturation to occur. The resulting DPV scans are shown for the three electrodes in Figure 6.4 shown previously.

The average percentage difference between probe DPV and DPV following NaOH treatment is -23.73%±3.88%. Similar to the results seen for urea, a clear reduction in target DPV current peaks occurs indicating the denaturation of duplex DNA. NaOH causes denaturation by increasing the pH of the solution environment (increase [OH]) disrupting the hydrogen bonding between bases. A negative % change compared to probe DPV indicates the possibility of probe removal by disrupting Au-thiol bonds or the presence of dissociated sodium ions which are electrostatically bound to DNA phosphate groups which persist after washing. This would cause inaccessibility of the same number of phosphate groups to RuHex and cause a decrease in DPV I currents.

It is concluded that both 8 mM urea and 50 mM NaOH are able to perform duplex DNA denaturation. As indicated by the negative percentage differences between scans following denaturation and probe scans (-16.91%±9.63% for urea, -23.73%±3.88% for NaOH), an exact

replication of the untreated probe monolayer did not occur, either due to probe removal or a decrease in the accessibility of RuHex causing a reduction in electrocatalytic current peaks.

6.4 Qubit Fluorescence Quantitation

By combining the use of either urea or NaOH for DNA duplex denaturation and the method of probe DNA desorption by MCE, it is now possible to proceed backwards from a duplex state to a bare sensor state by step-wise removal of target and probe DNA, which can then be quantitated and a hybridization efficiency can be measured.

Performing hybridization studies with probe and target-labelled DNA would be non-ideal due to possible steric hindrance of the fluorescent labels which would affect the interaction and hybridization between probe and target DNA. The use of the Qubit ssDNA is explored which enables the fluorescent post-labelling of ssDNA such that quantitation is possible with initially unlabeled probe and target DNA, allowing unhindered hybridization to occur. Unfortunately, urea is considered a contaminant for this assay (up to 2 mM, causing a 47% increase in signal[2]); therefore, NaOH was chosen for duplex. As such, the proposed scheme to determine hybridization efficiency is illustrated in Figure 6.6 below.

[2] https://tools.thermofisher.com/content/sfs/manuals/Qubit_ssDNA_Assay_UG.pdf

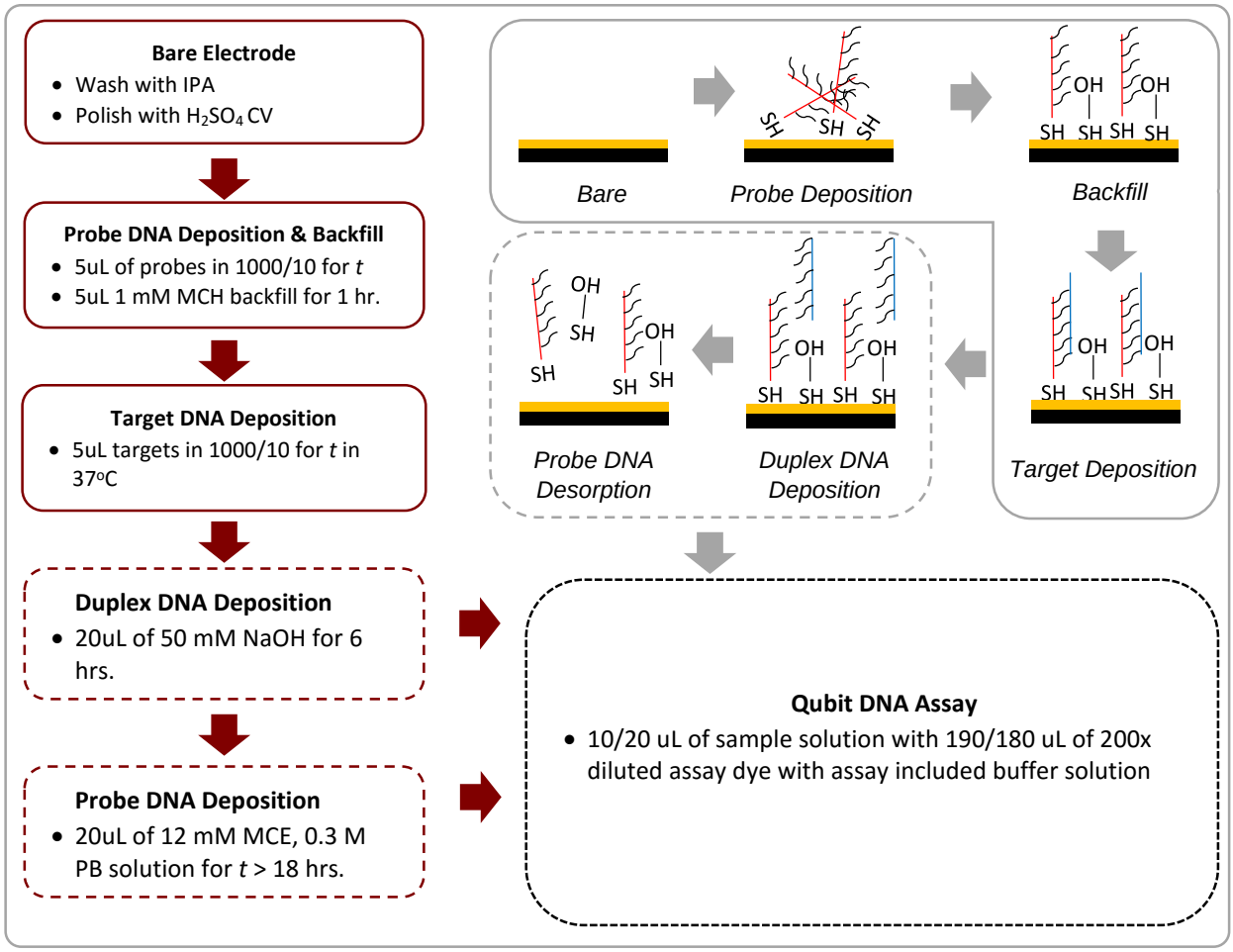

Figure 6.6 Schematic of the hybridization efficiency protocol. The steps in the solid outlined boxes illustrate the probe and target DNA deposition procedures. The steps in the dashed outlined boxes indicate the dsDNA denaturation and probe desorption procedures. The duration *t* for probe and target deposition vary with the experimental conditions. The Qubit assay was performed with the Qubit 3.0 fluorometer in raw fluorescence mode. The experimental description of this protocol is presented in section 6.4.1.

6.4.1 Qubit Assay Protocol (ssDNA and dsDNA)

In order to perform the Qubit assay, 20 uL of sample solution was added to 180 uL of a 200x diluted solution of Qubit DNA dye and Qubit DNA buffer. All DNA denaturation (50 mM NaOH) and desorption solutions (12 mM MCE, 0.3 M PB solution) were performed using 20 uL of the respective solution such that all of the sample is used for quantitation and no dilution is required. Once the 200 uL sample solution is created the mixture is briefly vortexed and equilibrated for 2 minutes to allow binding of the dye to DNA to maximize fluorescence. The Qubit 3.0 was operated in fluorometer mode such that manual collection of raw fluorescence units could be obtained. The provided standards with the assay contain lambda DNA (composed of 48,502 bases) and would be inappropriate for the creation of standard curves for 20mer DNA. Instead, a standard dilution of DNA was made in the same solution which the sample to be measured is in such that the only difference measured is from the variation in DNA concentration.

Following this protocol, standards dilution of ssDNA (10 nM, 50 nM, 100 nM, 500 nM, 1 µM) were first made in 50 mM NaOH and 12 mM MCE, 0.3 M PB solution to determine if linearity exists between ssDNA concentrations and the fluorescence signal emitted, and whether the solutions affect this linearity in fluorescence. These standard curves are shown in Figure 6..7 below.

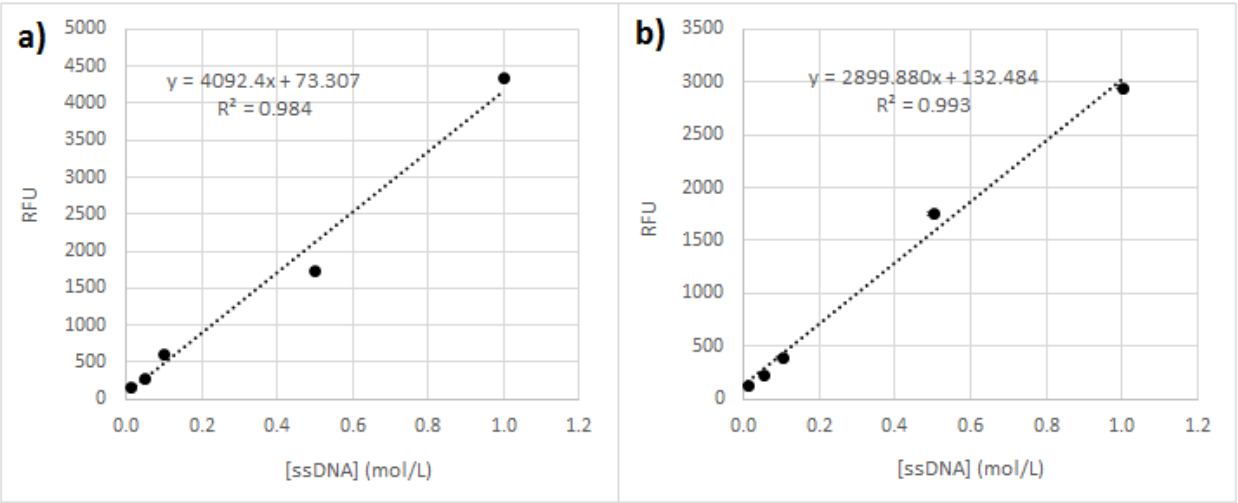

Figure 6.7 Standard dilutions of 20mer ssDNA in (a) 50 mM NaOH and (b) 12 mM MCE, 0.3 M PB solution showing the linearity of the Qubit ssDNA fluorescence assay.

Standard dilutions in 50 mM NaOH and 12 mM MCE, 0.3 M PB solution show acceptable linearity as indicated by the goodness of fit parameter. This demonstrates that desorbed and denatured DNA concentrations can be measured with the Qubit ssDNA assay.

In order to determine if a difference exists between ssDNA density measurements performed by fluorescence plate reading and by the Qubit assay, an experiment was performed to gauge the difference in fluorescence density measured due to differences in measurements based on florescence covalent pre-labelling and post-labelling. The method of fluorescence measurement using the plate reader was chosen as the standard with which the Qubit will be compared to. Measurements of probe density on 100 nm WSPEs will be the common measurement, with fluorescent probe DNA detected by the plate reader and non-fluorescent probe DNA detected by the Qubit ssDNA assay. For each measurement, 18 sample were measured.

Data were plotted as quantile-quantile plots to qualify fit to a normal distribution, as given in Figure 6.8 below. These plots were constructed by computing the rank-based z-scores of each of the probe density values and plotting against the same density values. A line is plotted to indicate a theoretical normal distribution with the same mean and standard deviation as the sample data. Comparison of how well the plotted data adheres to the line provides a qualitative assessment of normally distributed data.

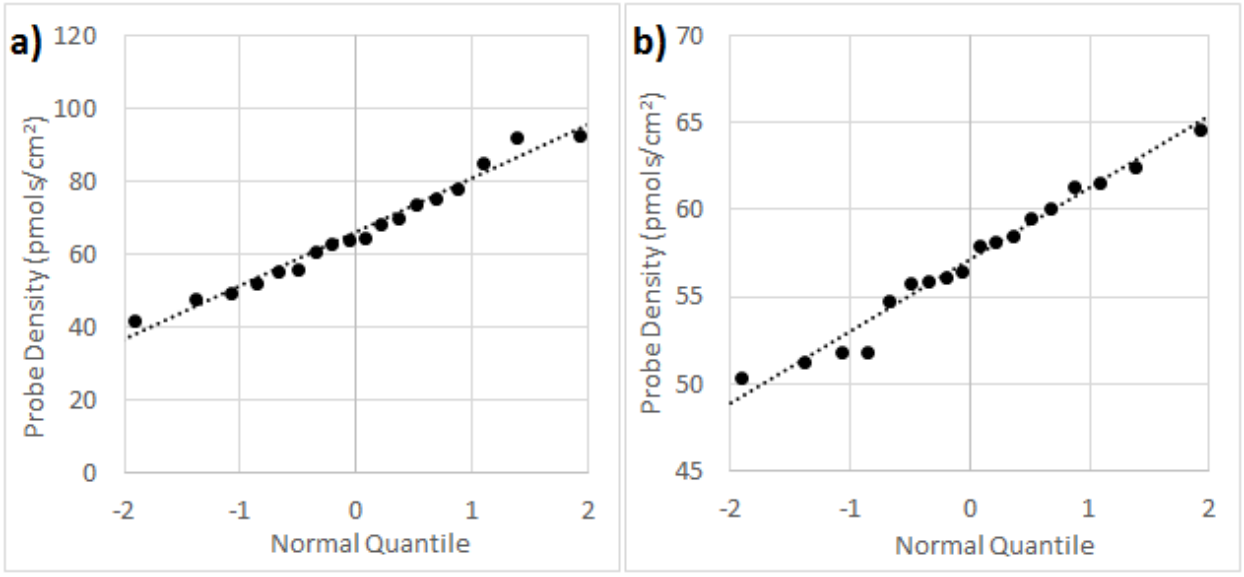

Figure 6.8 Quantile-Quantile plots for (a) probe density measured by plate reader and (b) probe density measured by Qubit ssDNA assay indicating data follows a normal distribution.

As the data indicates in Figure 6.8, both datasets are normally distributed. The fluorescent probe density measured by plate reader yielded an average value of 66.1±14.74 pmols/cm^2 and average non-fluorescent probe density by Qubit ssDNA assay was 57.17±4.06 pmols/cm^2. A two-tailed t-test was performed to test significance of difference of mean probe density values. The null hypothesis was chosen as 0 difference between probe density means (H_o: μ_1-μ_2 = 0), with alternate hypothesis as a non-zero difference between probe density means (H_μ: μ_1-$\mu_2 \neq 0$). Level of significance (α) was chosen as 0.01. The computed p-value of 0.0225 > α, therefore the null hypothesis of 0 difference between mean probe densities cannot be rejected. This concludes that the difference between measurements of densities between fluorescent plate reading and the Qubit ssDNA assay is not statistically significant.

6.5 Duplex DNA Denaturation with 50 mM NaOH

Section 6.5.1 presents the results for a full hybridization efficiency characterization with 50 mM NaOH on 100 nm sputter planar gold electrodes, 100 nm WSPEs, and 200 nm WSPEs. Sections 6.5.2 describes the ethanol concentration procedure to combine samples for PAGE analysis in sections 6.5.3, 6.5.4, and 6.5.5.

6.5.1 Hybridization Efficiency vs. Hybridization Duration Results

For all electrode types, 5 substrates (each 0.04 cm^2 projected area) for each group of target hybridization durations (15 minutes, 45 minutes, 2 hours, 4 hours, 8 hours, and 16 hours) were modified with 10 uM non-fluorescent ssDNA probe DNA for at least 18 hours to allow maximum probe deposition to occur. Following deposition, a 1 hr 1 mM MCH backfill was performed. 5 uL of 1 uM complementary target DNA was then deposited for the durations mentioned previously and incubated in 37 degree Celsius. Following the termination of hybridization duration, electrodes were submerged in 20 uL of 50 mM NaOH for 6 hours. This solution then used for the quantitation of un-labelled target DNA with the Qubit ssDNA assay. Following the target denaturation with NaOH, the electrodes were washed with DI water, and submerged in 20 uL of 12 mM MCE, 0.3 M PB solution for at least 18 hours. This solution was used to quantitate the probe density with the Qubit ssDNA assay. The probe and target densities, as well as the associated hybridization efficiency calculations are shown in Figure 6.9.

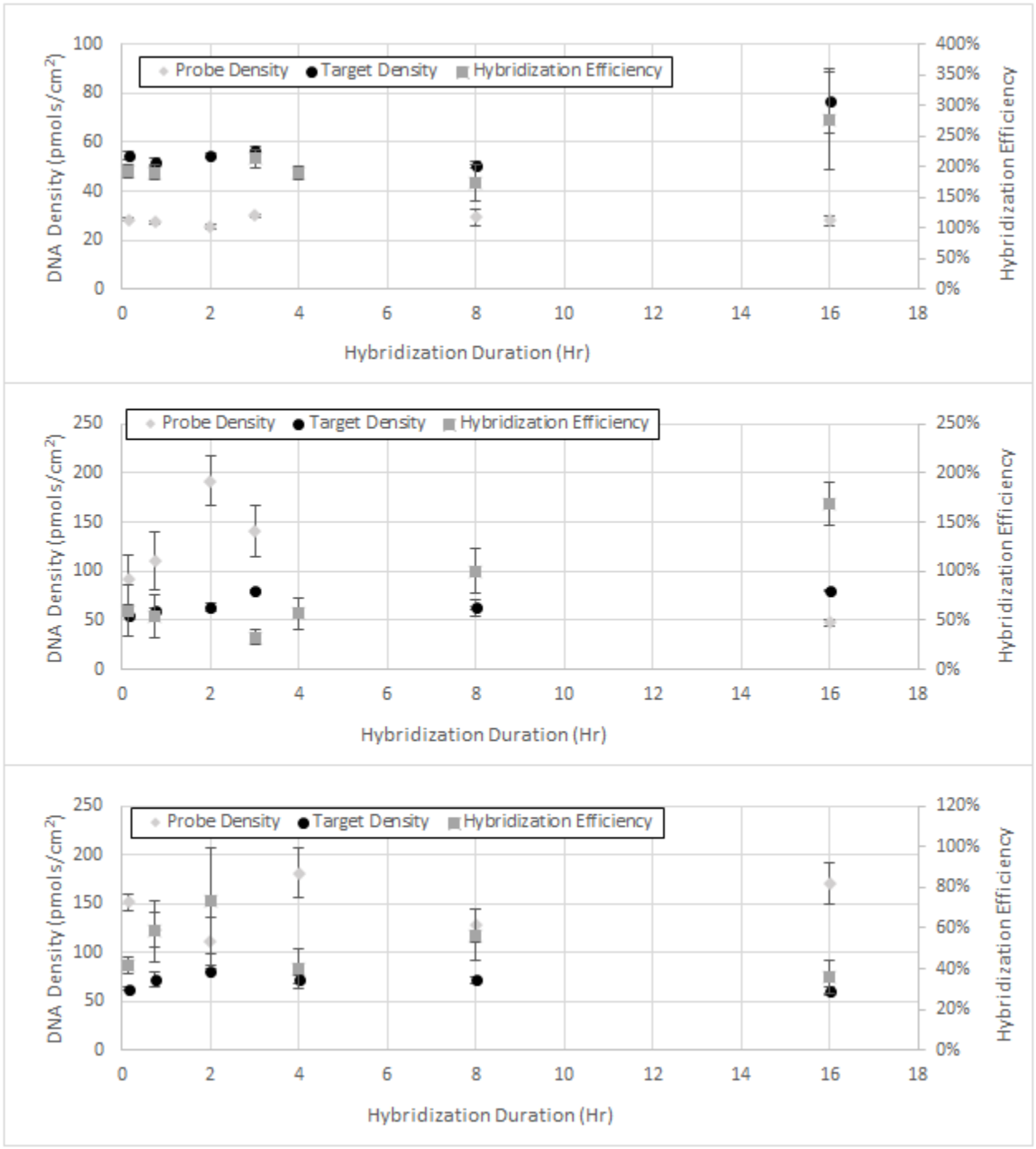

Figure 6.9 Hybridization efficiency of (a) planar, (b) 100 nm WSPEs, and (c) 200 nm WSPEs with various target hybridization durations as measured with the Qubit ssDNA assay. Duplex DNA denaturation was performed with 50 mM NaOH, and probe desorption with 12 mM MCE, 0.3 M PB solution. Probe deposition was performed for at least 18 hours for all electrodes. Each sample is an average of 5 electrodes. Standard error bars are shown.

The probe density shown for planar gold electrodes indicates a density which deviates slightly from 30 pmols/cm^2 which correlates well with previous probe deposition results. Since all electrodes are deposited with the same amount of probe DNA for maximum duration, it is expected that the density should deviate minimally between all electrodes. The target densities detected are much greater than the probe density, causing a concomitant inflation of the hybridization efficiency past 100%. It is unlikely that approximately twice the amount of probe DNA of target DNA was attached to the surface due to non-specific adsorption considering the rigorous washing steps employed.

The trend in hybridization efficiency is towards expectation. At short durations, an immediate capture of target DNA at the surface occurs and hybridization is mainly limited by the kinetics of the capture process. By 15 minutes the hybridization process becomes diffusion-limited as indicated by the longer duration of time required for the target density to increase to its maximum value at 16 hours.

For the results with 100 nm WSPEs, a larger deviation in the probe density was detected. Compared to densities seen previously with 100 nm WSPEs, the densities measured are higher at all points [97] and decreases to a minimum at 16 hours. The validity of these probe density values are questionable due to the fluctuation seen as well as the error associated with each average value, especially for those time points below 16 hours. As mentioned previously, there should be minimal variation in the probe densities between all electrodes, as all probe depositions were carried out with the same conditions.

Similar results in the probe density are seen with 200 nm WSPEs. A constancy which is expected is not seen with the probe density and the densities are higher than those expected [97]. The target densities contain much less variation and do show an initial increase over the first 2 hours followed by a slight decrease after a plateau during the 4th and 8th hour. Due to the probe readings, the hybridization efficiency mirrors this variability, but at all points the efficiency is below 100% due to the probe density being greater than the target density at all points.

In summation, the probe densities for planar gold show the most favorable probe density results and target deposition trend, but the hybridization efficiency is greater than 100% due to the target

DNA densities being greater than the probe density. For both 100 nm and 200 nm WSPEs, the probe density contains a large variability with the target densities showing a smaller variability and a trend towards what is expected from theory. This variability directly affects the calculation of hybridization efficiency, and as such, further investigation of the variability is required before the efficiencies can be definitive of the true state.

6.5.2 Detection of Duplex DNA Signal Contamination

Because the determination of hybridization relies on both probe and target densities, variability in both measurements must be minimized and sources of error need to be investigated and corrected. As mentioned previously, a target density much larger than the probe density is unlikely due to residual non-specifically-adsorbed ssDNA left after the washing procedure. A much more likely hypothesis is the presence of dsDNA in the two solutions used for target and probe quantification. In the target quantification step, this could be due to removal of duplex DNA from the electrode surface which is not denatured before quantitation. In the probe quantification step, duplex DNA could exist which did not get denatured from the denaturation procedure. According to product literature, the Qubit ssDNA dye is not specific for ssDNA; therefore, dsDNA is likely to cause an increase the fluorescence signal[3].

To validate this hypothesis and evaluate the presence of duplex DNA in both target and probe sample solutions, the Qubit dsDNA Broad-Range assay was used. 10 uM of probe DNA was fully deposited on 8 sets of electrodes for each planar gold, 100 nm WSPEs, and 200 nm WSPEs (total of 24 electrodes) for 16 hours. A backfill was performed with 1 mM MCH for 1 hour, followed by a 4 hour target deposition. Complementary target DNA was deposited on 4 electrodes, and non-complementary target DNA was deposited on another 4. Duplex DNA denaturation was performed by submerging electrodes in 20 uL of 50 mM NaOH for 6 hours. This solution was evenly split such that 10 uL was used for ssDNA characterization as before, whereas the other 10 uL was used for dsDNA analysis. Electrodes were then submerged in 20 uL of 12 mM MCE, 0.3 M PB solution for probe desorption. And the 20 uL volume was split as previously mentioned for ssDNA and dsDNA analysis. The average ssDNA and dsDNA quantitation results are shown in Figure 6.10 below. The title of each graph describes which DNA (probe or target) is being quantitated for

[3] https://tools.thermofisher.com/content/sfs/manuals/Qubit_ssDNA_Assay_UG.pdf

which electrode structure. Each bar in the graph indicates which assay kit was used (ssDNA or dsDNA) and which set of electrodes were used to perform the quantitation, either electrodes subjected to complementary target DNA (“compl.”) or non-complementary (“non-compl.”).

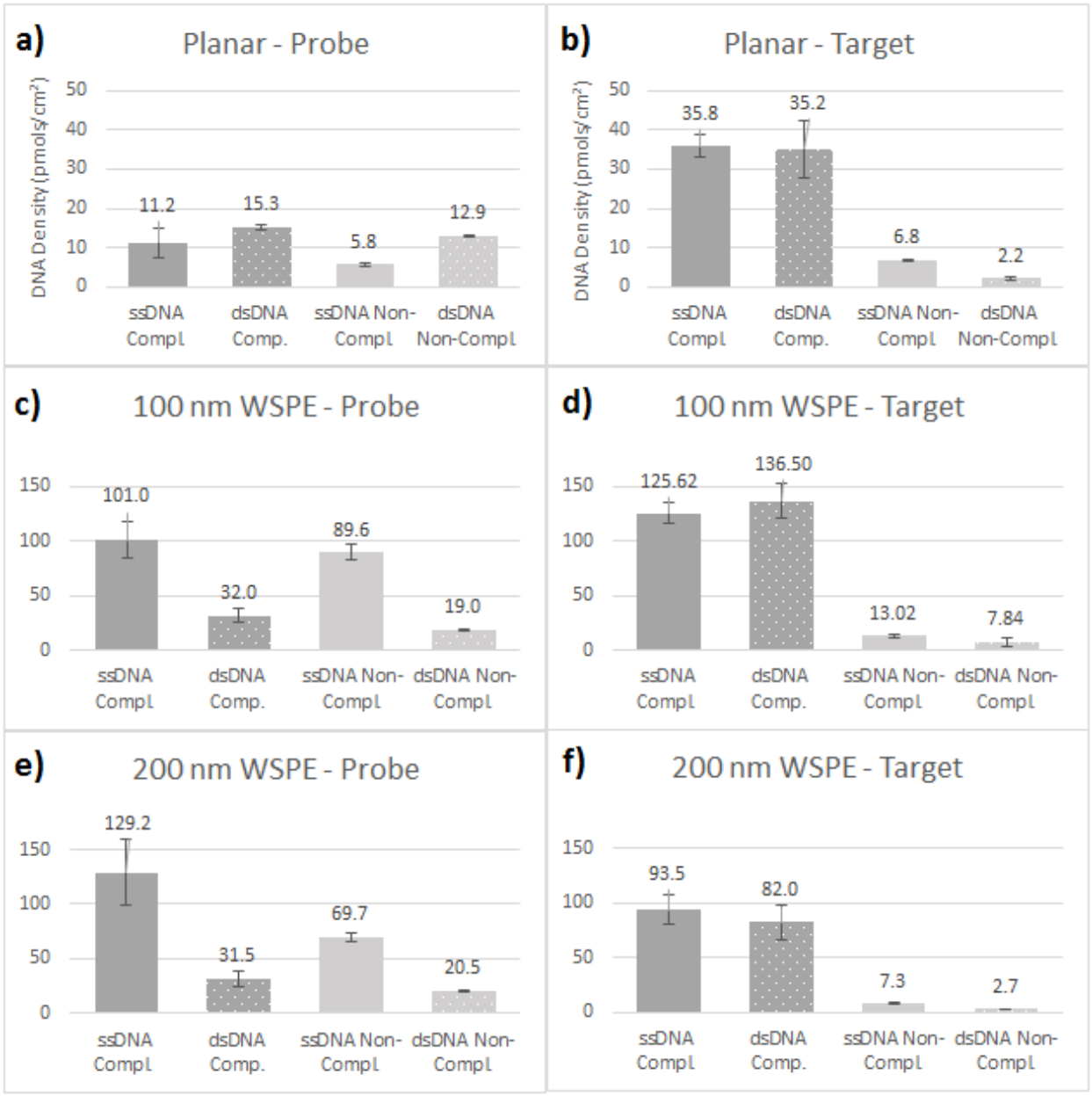

Figure 6.10 DNA density measured by Qubit ssDNA and dsDNA assay kits for solutions following probe denaturation with 12 mM MCE, 0.3 M PB solution (left column scans) and following dsDNA denaturation with 50 mM NaOH (right column scans) for planar (a-b), 100 nm WSPE, and 200 nm WSPE structures. Each bar indicates the assay kit used and if measurements were made from electrodes subjected to complementary or non-complementary DNA. Each measurement is an average of 3. Standard error bars are shown.

For all measurements of probe DNA (left column scans of Figure 6.10), it is expected that the densities for "ssDNA compl." and "ssDNA non-compl." for all electrode structures should be similar as all electrodes were deposited with probe DNA with identical conditions. No dsDNA should be detected in the solutions with probe DNA, as all target DNA should be either denatured with NaOH or removed by the washing procedure. It is seen that only 100 nm WSPEs contain equivalent probe densities between electrodes subjected to complementary and non-complementary target DNA (89.6 pmols/cm^2 and 101.0 pmols/cm^2). For planar and 200 nm WSPEs, the probe densities for electrodes subjected to complementary targets contain approximately twice the amount of probes as for electrodes subjected to non-complementary targets. For all electrodes, a higher amount of dsDNA was detected for electrodes subjected to complementary targets as compared to non-complementary targets. The presence of dsDNA in these solutions indicates either the detection of the dsDNA dye bound to ssDNA and/or the presence of duplex DNA which was not denatured by NaOH treatment.

For all measurements of target DNA (right column scans of Figure 6.10), it is expected that the complementary target densities measured by the ssDNA assay should be less than the respective probe densities. Non-complementary targets detected with the ssDNA and dsDNA assays should be low to reflect minimal non-complementary target hybridization. The measured complementary target densities (Figure 6.10b,d,f) for planar and 100 nm WSPEs are higher than the respective probe densities, which was a phenomenon seen for the experiments in Figure 6.9. Unlike the previous results, the complementary target densities are lower than the probe densities for 200 nm WSPEs. Low non-complementary target DNA was detected with the ssDNA assay (13.02 pmols/cm^2 and 7.3 pmols/cm^2) relative to their probe densities (89.6 pmols/cm^2 and 69.7 pmols/cm^2) for 100 nm and 200 nm WSPEs respectively, but was comparable for planar electrodes (6.8 pmols/cm^2 non-complementary target density against a probe density of 5.8 pmols/cm^2). Low dsDNA was detected for all electrodes subjected to non-complementary target DNA which aligns with expectation.

All measurements of dsDNA in solutions with complementary target DNA contain a comparable amount of dsDNA relative to the amount of complementary target ssDNA detected. The amount of dsDNA detected in solutions containing complementary targets seems to scale with the amount of ssDNA complementary targets detected. This suggests that as the number of ssDNA

complementary targets increases, a proportional increase of intact duplex DNA (and signal inflation) exists.

The graph shown in Figure 6.11 below presents the ratio of target density to probe density measurements and indicates the % signal inflation in the target measurements made by the ssDNA assay, compared to the probe measurements made by the ssDNA assay. The graph was constructed by taking the data in Figure 6.10 and dividing the complementary/non-complementary target ssDNA measurements with the appropriate probe ssDNA measurements (for electrodes subjected to either complementary or non-complementary DNA).

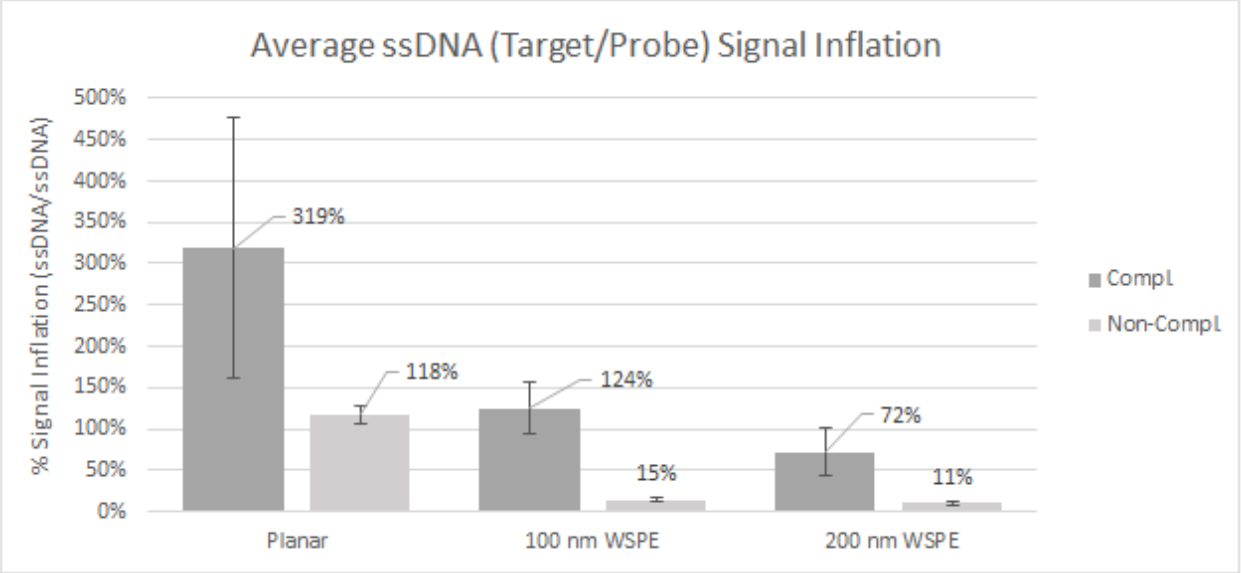

Figure 6.11 Average complementary and non-complementary target ssDNA/probe ssDNA signal inflation for planar, 100 nm WSPEs, and 200 nm WSPEs. Standard error bars are shown.

It is evident that the signal inflation is the largest for planar electrodes compared to the other electrode structures. The signal inflation is also positive for planar electrodes subjected to non-complementary targets and 100 nm WSPEs subjected to complementary targets. All other groups exhibit a lower target DNA compared to probe DNA. Both 100 nm and 200 nm WSPEs subjected to non-complementary DNA show low inflation.

In summary, all electrodes show a similar trend in which dsDNA is detected in larger amounts for complementary target electrodes at numbers that are comparable or even higher than the corresponding ssDNA target densities. This does not correspond to expectations as the amount of dsDNA detected should not equate the amount of target DNA denatured. It appears that the amount of dsDNA detected increases as the amount of ssDNA increases. This suggests that the dsDNA assay may not be specific to dsDNA and reflects a contribution by ssDNA as well. This effect can be seen in the planar MCE densities which indicate that dsDNA densities are greater than ssDNA probe densities.

Due to possible non-specificity of the dsDNA assay, another method was required to definitively conclude that dsDNA exists in the measurements of ssDNA.

6.5.3 20% Native-PAGE Protocol

In order to determine if dsDNA exists in the measurements of ssDNA, native (non-denaturing) polyacrylamide gel electrophoresis (PAGE) was used. PAGE allows the separation of DNA based on the differences in electrophoretic mobility in a gel, which is determined by the number of DNA bases (and associated charge). A 20% gel was cast by mixing 50 mL of a 20% 29:1 Bis/Acrylamide in 1xTBE buffer solution with 50 uL of tetramethylethylenediamine (TEMED), followed by 500 uL of 10% ammonium persulfate (APS) to initiate polymerization. 10 uL of DNA samples were combined with 6.77 uL of loading buffer consisting of 40% (w/v) sucrose and 1xTBE buffer and 3.333 uL of a 6x loading dye consisting of bromophenol blue and xylene cyanol FF, for a total loading volume of 20 uL. A vertical gel apparatus was used (VWR ASG-250). A maximum voltage of 1 kV was applied with an associated current of approximately 38 mA. Once the DNA has migrated about half-way down the gel, the gel was removed and bathed in a 50 mL solution containing 1xTBE buffer and 1xSYBR® Gold intercalating fluorescent dye for 10-20 minutes. The gel was then imaged with a BioRad ChemiDoc MP imaging system.

To gauge the limit of detection of the SYBR Gold fluorescent dye for fluorescence detection, dilutions of 20mer ssDNA were created in TE buffer and run with the protocol previously mentioned. A lower limit of 250 nM (2.5 pmols) was detected. In a similar manner, dilutions of dsDNA in TE buffer synthesized by IDT were processed with 20% PAGE. A lower limit of 0.5 pmols of dsDNA was detected.

6.5.4 Ethanol Purification of DNA

To meet the required minimum amount of DNA imposed by the SYBR Gold fluorescent dye, it was determined that a combination of five 10 uL samples would allow detection of both ssDNA and dsDNA with PAGE, although device specificity will be lost. Nevertheless, if dsDNA is detected from the combined samples, it will be confirm the presence of dsDNA.

To combine samples but maintain the loading volume for PAGE analysis at 10 uL, the combined samples were precipitated by ethanol purification. To the combined volume of 50 uL DNA, 5 uL of sodium acetate (pH = 5.2) and 5.5 uL of glycogen as a co-precipitant (5 mg/mL) was added and vortexed briefly before 153 uL of cold 100% ethanol was added. The mixture was vortexed and stored at -80 degree Celsius for at least 2 hours. After this period, the mixture was centrifuged for 15 minutes at maximum speed. The supernatant was decanted and 1 mL of 70% ethanol was added to the pellet to wash and was vortexed briefly. Finally the supernatant was decanted and the pellet was left to air dry before resuspension in 1xTE buffer. As such, the condensed DNA sample is removed from its original solution (either NaOH or MCE and PB solution) and replaced with a compatible buffer solution for PAGE analysis.

6.5.5 PAGE Results

To prepare samples for PAGE analysis, a hybridization efficiency experiment was performed on planar gold electrodes for 15 minute, 4 hour, and 18 hour hybridization durations. Electrodes were deposited with 5 μM probe DNA in 1000/10 overnight, followed by a 1 mM MCH backfill for 1 hour. Short (15 min.), medium (4 hr.), and long (18 hr.) hybridization durations with 10 μM complementary and non-complementary target DNA in 1000/10 were introduced to 5 electrodes each for each time period (30 electrodes in total). For this experiment, 10 uL of each of 50 NaOH and 12 mM MCE, 0.3 M PB solutions were used to measure with Qubit ssDNA assay, the other five 10 uL samples were combined and purified by ethanol precipitation before analyzing with PAGE. The probe and target DNA measured by the ssDNA assay for are presented in Figure 6.12.

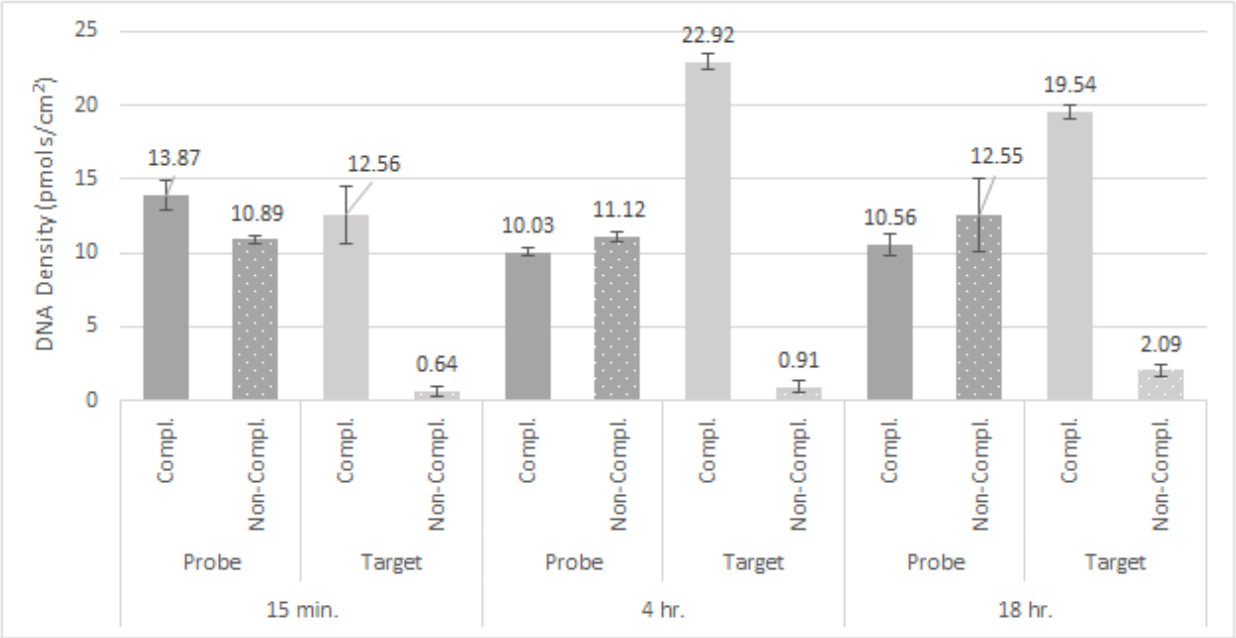

Figure 6.12 Probe and target DNA densities measured by the Qubit ssDNA assay for electrodes subjected to complementary and non-complementary target DNA for 15 min., 4 hr., and 18 hr. hybridization durations. All measurements are an average of 5. Standard error bars are shown.

It is expected that all probe densities should be similar as probe deposition conditions were identical. As shown in Figure 6.12, the probe densities do show similarity between groups with a small variation - the average probe density is 11.50±1.43 pmols/cm^2. As expected from the previous hybridization efficiency experiment, a larger complementary target density than the respective probe density is seen for electrodes subjected to 4 hour and 18 hour hybridization periods. The two densities are comparable for the 15 minute hybridization electrodes. All electrodes exhibit minimal non-complementary target detection.

The PAGE analysis for the purified solutions following duplex NaOH denaturation are presented in the right half of Figure 6.13 below. Standard dilutions of dsDNA were also analyzed with PAGE and are presented in the left half of Figure 6.13 below. Lane markers are shown to help segregate the lanes.

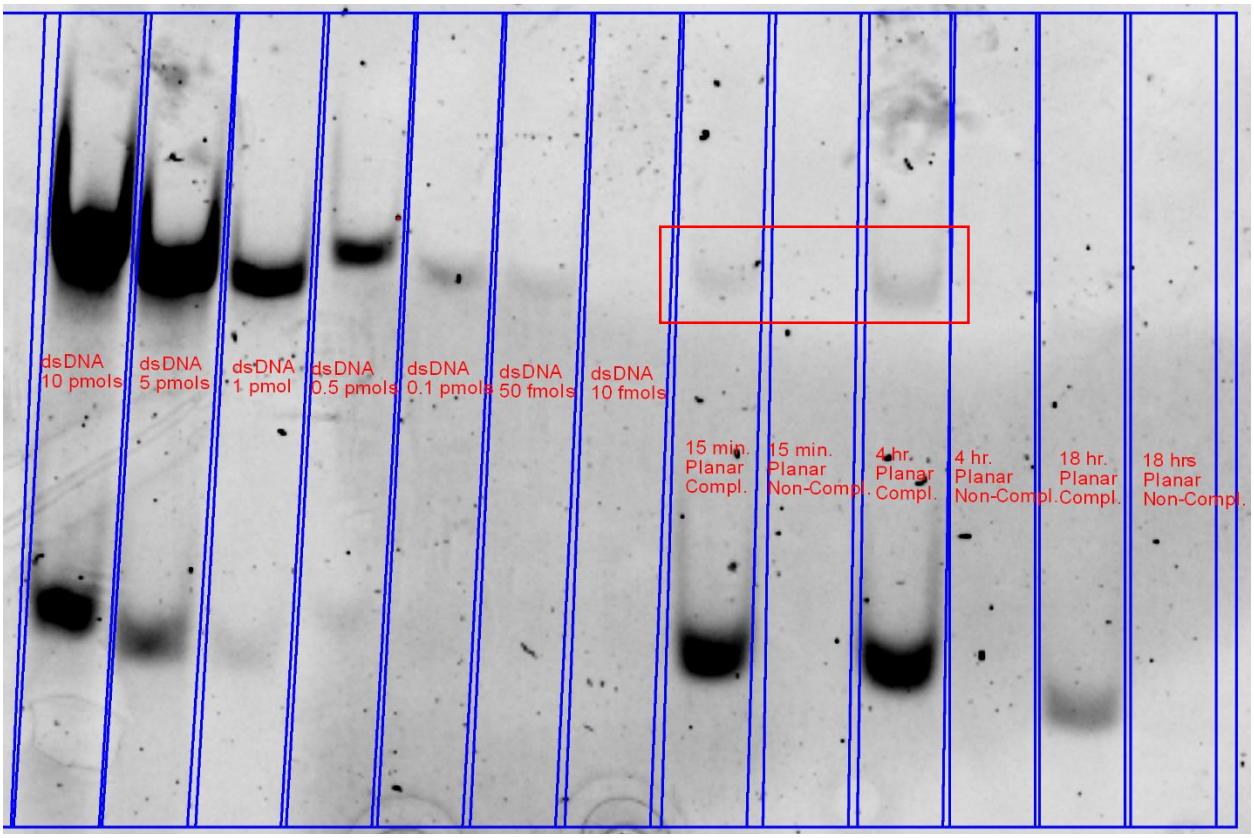

Figure 6.13 20% Native PAGE separation of 20mer ssDNA and dsDNA. Standard dilutions of dsDNA in 1xTE buffer are shown on the left half of the gel. Right half lanes of the gel are loaded with samples hybridized at 15 min., 4 hr., and 8 hr. with complementary or non-complementary DNA, denatured with 50 mM NaOH, purified with ethanol, and resuspended in 1xTE buffer. Bands in the lower half of the gel indicate ssDNA, bands in the upper half indicate dsDNA. The red box indicates the presence of dsDNA in the samples of target ssDNA.

PAGE analysis indicates 20mer dsDNA bands for the standard dilutions until 50 fmols, which corroborates with the lower limit indicated in section 6.5.3. Two bands attributed to 20mer ssDNA are also apparent for the lanes loaded with 10 pmols and 5 pmols of dsDNA. These are ssDNA left over from the synthesis of dsDNA which have not been hybridized. Complementary target ssDNA can be seen in the samples of 15 min. and 4 hr. lanes and to a lesser degree in the 18 hr. lane. The presence of these bands were expected, although the intensity for the 18 hr. samples appears fainter than expected, indicating a smaller amount of complementary target DNA than the other lanes. The ssDNA measurements in Figure 6.12 indicate that the amount of complementary target DNA for the 18 hr. samples is between that for 15 min. and 4 hr., as such,

the band intensity would be expected to be intermediate between these two band intensities. No ssDNA or dsDNA is apparent in any of the non-complementary lanes, indicating the absence of DNA for electrodes treated with non-complementary target DNA, which meets expectation.

More importantly, faint dsDNA bands (approximately between 50 fmols to 100 fmols as compared to the band intensities of the standard dilutions) are apparent in the lanes with 15 min. and 4 hr. hybridized target DNA, but not evident for 18 hours. This result concludes that dsDNA exists in the measurement of complementary target DNA measurements with the ssDNA assay following 50 mM NaOH denaturation. It is also concluded that dsDNA exists in the solution following 50 mM NaOH treatment which are not denatured and contributes to the heightened fluorescent signals when measured with the Qubit ssDNA assay.

No other groups have performed a quantitation of denatured complementary target DNA in NaOH nor a quantitation of probe DNA desorbed from an electrode surface using the Qubit ssDNA assay. Groups which have used the Qubit ssDNA/dsDNA assays have measured much longer DNA strands for simple quantitation procedures. For example, Wittman et. al [159] used the Qubit ssDNA assay to quantitate the amount of DNA following reverse transcription of RNA. Simbolo et. al [160] quantitated human genomic DNA with the Qubit dsDNA assay kit. Sah et. al [161] quantitated DNA obtained from human tissue in formalin-fixed, paraffin-embedded samples using the Qubit dsDNA assay kit.

The probe and target densities obtained using this characterization method are seen to be in range with those presented in section 6.2. For the densities with planar electrodes, typical maximum probe densities are approximately between 10-20 pmols/cm^2 which this assay demonstrates. The densities for 100 nm and 200 nm WSPEs are expected to be greater than planar electrodes owing surface area enhancements. This is trend demonstrated with the characterization method described in this chapter. In comparison to the probe densities for 100 nm and 200 nm WSPEs obtained by Woo et. al, this characterization method yields densities approximately twice as much, although a strict comparison cannot be made since Woo et. al did not perform a backfill procedure, which would decrease the potential probe density compared to characterization performed here.

6.6 Conclusion

This section presented the development of a hybridization efficiency characterization scheme which permits the sequential determination of probe and target densities in one experiment. Following hybridization of target DNA to the electrode, 50 mM NaOH is used to denature duplex DNA, followed by a desorption of probe DNA using 12 mM MCE and 0.3 M PB solution. The Qubit ssDNA assay was compared to conventional fluorescence plate reading DNA quantitation and the difference in measurement was found not to be significant. Next, a hybridization efficiency experiment for planar, 100 nm WESPEs, and 200 nm WESPEs indicated higher target densities than probe densities. The hypothesis that dsDNA is causing inflated fluorescence readings with the ssDNA assay kit was confirmed by performing PAGE analysis on samples combined by ethanol purification.

7.0 Conclusion

7.1 Thesis Findings and Contributions

This thesis demonstrated the fabrication and use of all-solution processed electrodes for the electrocatalytic detection of DNA hybridization. Also, a label-free characterization method for hybridization efficiency was developed. To review, the following summarizes the objectives of this thesis:

I. To rapidly-fabricate micro/nano-structured electrodes using an all-solution-processing technique,

II. To characterize the binding of probe DNA to these electrodes by variations in deposition time and probe molar fraction,

III. To demonstrate the electrocatalytic detection of DNA hybridization using these electrodes, and

IV. To develop a label-free technique for the characterization of DNA hybridization efficiency by the sequential determination of probe and target DNA densities in one experiment, yielding electrode-specific information.

By combining the techniques of xurography, surface silanization, and electroless-deposition, micro/nano-structured gold electrodes could be rapidly-fabricated, employing pre-stressed polystyrene as a substrate for heat-induced micro/nano-structuring of the electrolessly-deposited surface gold film (section 5.1)

Optical measurements indicate that the reduction of feature sizes (reduction of length and width dimensions by 60%) adhered to observations seen previously with wrinkled, polystyrene electrodes (section 5.2.1). Measurements of electro-active surface area (section 5.2.1) conclude that 2 min. electrolessly-deposited electrodes contribute to the highest surface area enhancement factor (4.24) compared with those deposited at 8 min. and 20 min., which SEM analysis reveals is due to porosity (section 5.2.2). This analysis also reveals both an increase in the size of wrinkling with the increase in deposition duration, as well as the decrease in pore size which disappear completely between 3 and 5 min. deposition periods.

Electrodes deposited at 2 min., 8 min., and 20 min. all demonstrated tunability in 20mer probe DNA density with the probe molar ratio (section 5.3.1) and with the probe deposition duration (section 5.3.2), with the highest density occurring at a molar ratio of 1 and at 16 hour deposition duration. Densities for all electrolessly-deposited electrodes were higher than for planar electrodes, with 2 min., electrodes exhibiting the highest density throughout.

Cyclic voltammetry of 2 min., 8 min., and 20 min. electrodes (section 5.3.3.1) indicate clear reduction in charge transfer upon the modification of the surfaces with probe DNA and MCH spacer molecules, with 2 min. devices showing a further reduction upon complementary target capture. An electrocatalytic detection system employing RuHex and FiCN [129] was used for electrochemical detection of complementary target hybridization. Electrodes deposited at 2 min. showed the highest % signal change (70.08%±16.69%) compared to 8 min. and 20 min. electrodes which is hypothesized to be due to the high surface are enhancement provided by porosity (section 5.3.3.2). The limit of detection for 2 min. electrodes was found to be 10 μM, which is the lowest concentration leading to a signal discernible from background signals and is a factor of 3 greater than the standard deviation at the limit of detection (section 5.3.4).

By using 50 mM NaOH as a denaturating agent for duplex DNA [155], complementary target DNA could be removed from surface-bound probe DNA, which could then be desorbed from the surface with MCE (section 6.3). The Qubit ssDNA assay was found to be a comparable method to fluorescence plate reading for measuring DNA density (section 6.4). As such, the sequential removal of DNA was paired with the Qubit ssDNA assay which allowed the determination of target and probe densities in one experiment, for the same electrode. This characterization method was applied to planar, 100 nm and 200 nm wrinkled, polystyrene electrodes (section 6.5.1). It was found that target densities were higher than probe densities which was hypothesized to be due to the presence of duplex DNA in the ssDNA measurements. Measurements using the Qubit dsDNA assay to quantitate this possible dsDNA proved to be inconclusive (section 6.5.2). PAGE analysis (section 6.5.3) confirmed the existence of dsDNA in the measurements of complementary target DNA captured by planar electrodes for 15 minutes and 4 hours (section 6.5.5).

7.2 Future Work

Further tuning of electrocatalytic detection parameters for the all-solution processed porous detection have the potential to lower detection limits further. It has been demonstrated that the probe molar ratio affects the electrocatalytic detection performance [97]; therefore, optimization of this parameter would likely benefit sensing. Another parameter which could be explored for further tuning is the pore-size of the electrode. It was seen in the SEM images presented in section 5.2.2 that the pore sizes decreased as the deposition duration increased. An optimal pore size may exist which could be more accessible to both probe and target DNA, enhancing the electrocatalytic detection. Another possible development could be the use of peptide-nucleic acid (PNA) instead of DNA for the probe. PNA has a similar chemical structure to DNA except it contains a neutral back-bone [162]. This has the potential to lower background currents for the electrocatalytic detection scheme. A third dimension of micro/nanostructuring, apart from wrinkling and porosity, could be imparted to the electrodes by electrodeposition, as discussed in section 2.3.3. Further tuning of the deposited structures may yield significant enhancement to DNA detection [72]. Other signal amplification strategies could also be investigated. Rolling cyclic amplification (RCA) is an attractive candidate owing to the low temperature requirement for amplification (37 degree Celsius) and the potential yield of duplicated DNA [75]. This strategy could potentially decrease the amount of redox reporters necessary for detection as a significant increase in the amount of DNA would be able to be replicated and detected upon target hybridization.

For further development of the hybridization efficiency characterization, purification techniques such as high performance liquid chromatography (HPLC) could be investigated to purify dsDNA from ssDNA samples. An optimization of both the NaOH concentration and treatment duration could also be of benefit to increase the denaturation of dsDNA at the surface such as to lower the dsDNA which survive in the quantitation stage. An extra denaturation step preceding quantitation may also help to further decrease signal contamination by dsDNA when performing ssDNA quantitation. More elaborate implementations may also be explored which could be of benefit for purification of dsDNA, including the possible use of microfluidic channels and integrated active components to separate DNA by electrophoresis. The smaller volumes used in

microfluidic applications may make the separation efficiency greater than for conventional PAGE or agarose gels.

7.3 Final Remarks

POC diagnostics devices are required to meet the current and future challenges posed by the burden of disease [9]. One path to achieve lower detection limits and higher sensitivities is the development of low-cost, rapid-fabrication techniques to aid in the turnaround time of device research and development. Micro/nano-structured electrodes have shown to be a promising method to achieve these lower detection limits [163]; however, adequate rapid-prototyping techniques have yet to be demonstrated for creating electrodes with tunable micro/nano-scale features. The all-solution processed electrodes presented in this thesis are an attractive candidate to fulfill this need, showing tunability in surface features as well as probe DNA density for the electrocatalytic detection of DNA down to 1 nM concentration.

Characterization of hybridization efficiency for DNA biosensors provides an understanding of the capture efficiency of immobilized probe DNA at the sensor surface; however, current techniques require multiple experiments to be performed and micro/nano-structured electrodes may not be compatible with conventional techniques. The label-free characterization method presented in this thesis has the potential to offer researchers the ability to study electrodes with any surface structuring, providing an electrode-specific measure of hybridization efficiency.

References

[1] P. B. Luppa, A. Bietenbeck, C. Beaudoin, and A. Giannetti, “Clinically relevant analytical techniques, organizational concepts for application and future perspectives of point-of-care testing,” *Biotechnol. Adv.*, vol. 34, no. 3, pp. 139–160, May 2016.

[2] M. J. O’Kane, “Point of Care Testing - Current and Emerging Quality Perspectives,” *Point Care*, vol. 13, no. 1, pp. 1–5, 2014.

[3] I. V Jani and T. F. Peter, “How point-of-care testing could drive innovation in global health,” *N Engl J Med*, vol. 368, no. 24, pp. 2319–2324, 2013.

[4] A. St John and C. P. Price, “Existing and Emerging Technologies for Point-of-Care Testing.,” *Clin. Biochem. Rev.*, vol. 35, no. 3, pp. 155–67, 2014.

[5] M. Medical, “World Market for POC Diagnostics,” 2015.

[6] W. H. Organization, “The World Health Report 2005,” Jun. 2005.

[7] G. Jones, R. W. Steketee, R. E. Black, Z. A. Bhutta, and S. S. Morris, “How many child deaths can we prevent this year?,” *Lancet*, vol. 362, no. 9377, pp. 65–71, 2003.

[8] S. Rosen and M. P. Fox, “Retention in HIV care between testing and treatment in sub-Saharan Africa: A systematic review,” *PLoS Med.*, vol. 8, no. 7, 2011.

[9] P. Yager, G. J. Domingo, and J. Gerdes, “Point-of-care diagnostics for global health.,” *Annu. Rev. Biomed. Eng.*, vol. 10, pp. 107–44, 2008.

[10] J. M. Blandford, T. L. Gift, S. Vasaikar, D. Mwesigwa-Kayongo, P. Dlali, and R. N. Bronzan, “Cost-Effectiveness of On-Site Antenatal Screening to Prevent Congenital Syphilis in Rural Eastern Cape Province, Republic of South Africa,” *Sex. Transm. Dis.*, vol. 34, no. Supplement, pp. S61–S66, Jul. 2007.

[11] R. W. Peeling and P. Olliaro, “Reimagining the Future of the Diagnosis of Viral Infections,” *J. Infect. Dis.*, p. jiw107, Mar. 2016.

[12] C. D. Mathers and D. Loncar, “Projections of Global Mortality and Burden of Disease

from 2002 to 2030," *PLoS Med.*, vol. 3, no. 11, p. e442, Nov. 2006.

[13] H. Kettler, K. White, and S. Hawkes, "Mapping the landscape of diagnostics for sexually transmitted infections: Key findings and recommandations," pp. 1–44, 2004.

[14] A. Niemz, T. M. Ferguson, and D. S. Boyle, "Point-of-care nucleic acid testing for infectious diseases," *Trends Biotechnol.*, vol. 29, no. 5, pp. 240–250, 2011.

[15] M. A. Dineva, L. Mahilum-Tapay, and H. Lee, "Sample preparation: a challenge in the development of point-of-care nucleic acid-based assays for resource-limited settings," *Analyst*, vol. 132, no. 12, p. 1193, 2007.

[16] S. Park, Y. Zhang, S. Lin, T.-H. Wang, and S. Yang, "Advances in microfluidic PCR for point-of-care infectious disease diagnostics," *Biotechnol. Adv.*, vol. 29, no. 6, pp. 830–839, Nov. 2011.

[17] L. Doleman, L. Davies, L. Rowe, E. A. Moschou, S. Deo, and S. Daunert, "Bioluminescence DNA Hybridization Assay for Plasmodium f alciparum Based on the Photoprotein Aequorin," *Anal. Chem.*, vol. 79, no. 11, pp. 4149–4153, Jun. 2007.

[18] D. R. Thévenot, K. Toth, R. A. Durst, and G. S. Wilson, "Electrochemical biosensors: recommended definitions and classification1International Union of Pure and Applied Chemistry: Physical Chemistry Division, Commission I.7 (Biophysical Chemistry); Analytical Chemistry Division, Commission V.5 (Electroanalytical," *Biosens. Bioelectron.*, vol. 16, no. 1–2, pp. 121–131, Jan. 2001.

[19] D. G. Rackus, M. H. Shamsi, and A. R. Wheeler, "Electrochemistry, biosensors and microfluidics: a convergence of fields," *Chem. Soc. Rev.*, vol. 44, no. 15, pp. 5320–5340, 2015.

[20] K. R. Rogers, "Principles of Affinity-Based Biosensors," *Mol. Biotechnol.*, vol. 14, no. 2, pp. 109–130, 2000.

[21] S. M. Borisov and O. S. Wolfbeis, "Optical Biosensors," *Chem. Rev.*, vol. 108, no. 2, pp. 423–461, Feb. 2008.

[22] T. M. A. Gronewold, "Surface acoustic wave sensors in the bioanalytical field: Recent

trends and challenges," *Anal. Chim. Acta*, vol. 603, no. 2, pp. 119–128, Nov. 2007.

[23] K. Länge, B. E. Rapp, and M. Rapp, "Surface acoustic wave biosensors: a review," *Anal. Bioanal. Chem.*, vol. 391, no. 5, pp. 1509–1519, Jul. 2008.

[24] J. Fritz, "Translating Biomolecular Recognition into Nanomechanics," *Science (80-.).*, vol. 288, no. 5464, pp. 316–318, Apr. 2000.

[25] R. Datar, A. Passian, R. Desikan, and T. Thundat, "Microcantilever Biosensors," in *2007 IEEE Sensors*, 2007, vol. 37, no. 2005, pp. 5–5.

[26] Y. Zhang, H. Kim, and A. Heller, "Enzyme-Amplified Amperometric Detection of 3000 Copies of DNA in a 10-μL Droplet at 0.5 fM Concentration," *Anal. Chem.*, vol. 75, no. 13, pp. 3267–3269, Jul. 2003.

[27] D. C. Duffy, J. C. McDonald, O. J. Schueller, and G. M. Whitesides, "Rapid Prototyping of Microfluidic Systems in Poly(dimethylsiloxane).," *Anal. Chem.*, vol. 70, no. 23, pp. 4974–84, Dec. 1998.

[28] A. Waldbaur, H. Rapp, K. Länge, and B. E. Rapp, "Let there be chip—towards rapid prototyping of microfluidic devices: one-step manufacturing processes," *Anal. Methods*, vol. 3, no. 12, p. 2681, 2011.

[29] H. Peng, L. Zhang, C. Soeller, and J. Travas-Sejdic, "Conducting polymers for electrochemical DNA sensing.," *Biomaterials*, vol. 30, no. 11, pp. 2132–48, Apr. 2009.

[30] C. M. B. Ho, S. H. Ng, K. H. H. Li, and Y.-J. Yoon, "3D printed microfluidics for biological applications," *Lab Chip*, vol. 15, no. 18, pp. 3627–3637, 2015.

[31] D. Chudobova, K. Cihalova, S. Skalickova, J. Zitka, M. A. M. Rodrigo, V. Milosavljevic, D. Hynek, P. Kopel, R. Vesely, V. Adam, and R. Kizek, "3D-printed chip for detection of methicillin-resistant Staphylococcus aureus labeled with gold nanoparticles," *Electrophoresis*, vol. 36, no. 3, pp. 457–466, 2015.

[32] R. M. Dirkzwager, S. Liang, and J. A. Tanner, "Development of Aptamer-Based Point-of-Care Diagnostic Devices for Malaria Using 3D Printing Rapid Prototyping," *ACS Sensors*, p. acssensors.5b00175, 2016.

[33] W. Lee, D. Kwon, B. Chung, G. Y. Jung, A. Au, A. Folch, and S. Jeon, “Ultrarapid Detection of Pathogenic Bacteria Using a 3D Immunomagnetic Flow Assay,” *Anal. Chem.*, vol. 86, no. 13, pp. 6683–6688, Jul. 2014.

[34] W. Lee, D. Kwon, W. Choi, G. Y. Jung, and S. Jeon, “3D-printed microfluidic device for the detection of pathogenic bacteria using size-based separation in helical channel with trapezoid cross-section.,” *Sci. Rep.*, vol. 5, p. 7717, 2015.

[35] A. I. Shallan, P. Smejkal, M. Corban, R. M. Guijt, and M. C. Breadmore, “Cost-Effective Three-Dimensional Printing of Visibly Transparent Microchips within Minutes,” *Anal. Chem.*, vol. 86, no. 6, pp. 3124–3130, 2014.

[36] E. C. Spivey, B. Xhemalce, J. B. Shear, and I. J. Finkelstein, “3D-Printed Micro fl uidic Microdissector for High-Throughput Studies of Cellular Aging,” 2014.

[37] J. L. Erkal, A. Selimovic, B. C. Gross, S. Y. Lockwood, E. L. Walton, S. McNamara, R. S. Martin, and D. M. Spence, “3D printed microfluidic devices with integrated versatile and reusable electrodes,” *Lab Chip*, vol. 14, no. 12, pp. 2023–2032, 2014.

[38] N. Bhattacharjee, A. Urrios, S. Kang, and A. Folch, “The upcoming 3D-printing revolution in microfluidics,” *Lab Chip*, 2016.

[39] F. Li, H. Zhang, B. Dever, X.-F. Li, and X. C. Le, “Thermal Stability of DNA Functionalized Gold Nanoparticles,” *Bioconjug. Chem.*, vol. 24, no. 11, pp. 1790–7, 2013.

[40] C. Parolo and A. Merkoci, “Paper-based nanobiosensors for diagnostics,” *Chem. Soc. Rev.*, vol. 42, no. 2, pp. 450–457, 2013.

[41] A. W. Martinez, S. T. Phillips, and G. M. Whitesides, “Three-dimensional microfluidic devices fabricated in layered paper and tape.,” *Proc. Natl. Acad. Sci. U. S. A.*, vol. 105, no. 50, pp. 19606–19611, 2008.

[42] M. Li, Y.-T. Li, D.-W. Li, and Y.-T. Long, “Recent developments and applications of screen-printed electrodes in environmental assays--a review.,” *Anal. Chim. Acta*, vol. 734, pp. 31–44, Jul. 2012.

[43] A. Hayat and J. Marty, “Disposable Screen Printed Electrochemical Sensors: Tools for

Environmental Monitoring," *Sensors*, vol. 14, no. 6, pp. 10432–10453, Jun. 2014.

[44] R. Ren, C. Leng, and S. Zhang, "A chronocoulometric DNA sensor based on screen-printed electrode doped with ionic liquid and polyaniline nanotubes," *Biosens. Bioelectron.*, vol. 25, no. 9, pp. 2089–2094, 2010.

[45] B. R. Šljukić, R. O. Kadara, and C. E. Banks, "Disposable manganese oxide screen printed electrodes for electroanalytical sensing," *Anal. Methods*, vol. 3, no. 1, pp. 105–109, 2011.

[46] N. a. Choudry, D. K. Kampouris, R. O. Kadara, and C. E. Banks, "Disposable highly ordered pyrolytic graphite-like electrodes: Tailoring the electrochemical reactivity of screen printed electrodes," *Electrochem. commun.*, vol. 12, no. 1, pp. 6–9, Jan. 2010.

[47] N. a. Choudhry, D. K. Kampouris, R. O. Kadara, N. Jenkinson, and C. E. Banks, "Next generation screen printed electrochemical platforms: Non-enzymatic sensing of carbohydrates using copper(ii) oxide screen printed electrodes," *Anal. Methods*, vol. 1, no. 3, p. 183, 2009.

[48] W.-Y. Su, S.-M. Wang, and S.-H. Cheng, "Electrochemically pretreated screen-printed carbon electrodes for the simultaneous determination of aminophenol isomers," *J. Electroanal. Chem.*, vol. 651, no. 2, pp. 166–172, Feb. 2011.

[49] H. Wei, J.-J. Sun, Y. Xie, C.-G. Lin, Y.-M. Wang, W.-H. Yin, and G.-N. Chen, "Enhanced electrochemical performance at screen-printed carbon electrodes by a new pretreating procedure.," *Anal. Chim. Acta*, vol. 588, no. 2, pp. 297–303, Apr. 2007.

[50] T. G. Henares, K. Yamada, K. Suzuki, and D. Citterio, *Design of Polymeric Platforms for Selective Biorecognition*. Cham: Springer International Publishing, 2015.

[51] I. Barbulovic-Nad, M. Lucente, Y. Sun, M. Zhang, A. R. Wheeler, and M. Bussmann, "Bio-Microarray Fabrication Techniques—A Review," *Crit. Rev. Biotechnol.*, vol. 26, no. 4, pp. 237–259, Jan. 2006.

[52] M. S. Khan, D. Fon, X. Li, J. Tian, J. Forsythe, G. Garnier, and W. Shen, "Biosurface engineering through ink jet printing," *Colloids Surfaces B Biointerfaces*, vol. 75, no. 2, pp. 441–447, Feb. 2010.

[53] J. Wu, R. Wang, H. Yu, G. Li, K. Xu, N. C. Tien, R. C. Roberts, and D. Li, "Inkjet-printed microelectrodes on PDMS as biosensors for functionalized microfluidic systems," *Lab Chip*, vol. 15, no. 3, pp. 690–695, 2015.

[54] T. H. da Costa, E. Song, R. P. Tortorich, and J.-W. Choi, "A Paper-Based Electrochemical Sensor Using Inkjet-Printed Carbon Nanotube Electrodes," *ECS J. Solid State Sci. Technol.*, vol. 4, no. 10, pp. S3044–S3047, Aug. 2015.

[55] R. Gasparac, B. J. Taft, M. A. Lapierre-Devlin, A. D. Lazareck, J. M. Xu, and S. O. Kelley, "Ultrasensitive electrocatalytic DNA detection at two- and three-dimensional nanoelectrodes," *J. Am. Chem. Soc.*, vol. 126, no. 39, pp. 12270–12271, 2004.

[56] S. Mathur, A. Erdem, C. Cavelius, S. Barth, and J. Altmayer, "Amplified electrochemical DNA-sensing of nanostructured metal oxide films deposited on disposable graphite electrodes functionalized by chemical vapor deposition," *Sensors Actuators B Chem.*, vol. 136, no. 2, pp. 432–437, Mar. 2009.

[57] J. A. Hansen, R. Mukhopadhyay, J. Hansen, and K. V. Gothelf, "Femtomolar electrochemical detection of DNA targets using metal sulfide nanoparticles," *J. Am. Chem. Soc.*, vol. 128, no. 12, pp. 3860–3861, 2006.

[58] S.-J. Park, T. A. Taton, and C. A. Mirkin, "Array-based electrical detection of DNA with nanoparticle probes.," *Science*, vol. 295, no. 5559, pp. 1503–1506, 2002.

[59] L. Authier, C. Grossiord, P. Brossier, and B. Limoges, "Gold nanoparticle-based quantitative electrochemical detection of amplified human cytomegalovirus DNA using disposable microband electrodes," *Anal. Chem.*, vol. 73, no. 18, pp. 4450–4456, 2001.

[60] J. Li, Q. Liu, Y. Liu, S. Liu, and S. Yao, "DNA biosensor based on chitosan film doped with carbon nanotubes," *Anal. Biochem.*, vol. 346, no. 1, pp. 107–114, 2005.

[61] J. Li, H. T. Ng, A. Cassell, W. Fan, H. Chen, Q. Ye, J. Koehne, J. Han, and M. Meyyappan, "Carbon nanotube nanoelectrode array for ultrasensitive DNA detection," *Nano Lett.*, vol. 3, no. 5, pp. 597–602, 2003.

[62] A. Bonanni, M. J. Esplandiu, and M. del Valle, "Impedimetric genosensors employing COOH-modified carbon nanotube screen-printed electrodes," *Biosens. Bioelectron.*, vol.

24, no. 9, pp. 2885–2891, May 2009.

[63] O. Akhavan, E. Ghaderi, and R. Rahighi, “Toward single-DNA electrochemical biosensing by graphene nanowalls,” *ACS Nano*, pp. 2904–2916, 2012.

[64] Z. Wang, J. Zhang, P. Chen, X. Zhou, Y. Yang, S. Wu, L. Niu, Y. Han, L. Wang, P. Chen, F. Boey, Q. Zhang, B. Liedberg, and H. Zhang, “Label-free, electrochemical detection of methicillin-resistant staphylococcus aureus DNA with reduced graphene oxide-modified electrodes,” *Biosens. Bioelectron.*, vol. 26, no. 9, pp. 3881–3886, May 2011.

[65] H. Chang, Y. Yuan, N. Shi, and Y. Guan, “Electrochemical DNA biosensor based on conducting polyaniline nanotube array,” *Anal. Chem.*, vol. 79, no. 13, pp. 5111–5115, 2007.

[66] N. Zhu, Z. Chang, P. He, and Y. Fang, “Electrochemically fabricated polyaniline nanowire-modified electrode for voltammetric detection of DNA hybridization,” *Electrochim. Acta*, vol. 51, no. 18, pp. 3758–3762, May 2006.

[67] Y. Bo, H. Yang, Y. Hu, T. Yao, and S. Huang, “A novel electrochemical DNA biosensor based on graphene and polyaniline nanowires,” *Electrochim. Acta*, vol. 56, no. 6, pp. 2676–2681, 2011.

[68] E. Spain, T. E. Keyes, and R. J. Forster, “DNA sensor based on vapour polymerised pedot films functionalised with gold nanoparticles,” *Biosens. Bioelectron.*, vol. 41, no. 1, pp. 65–70, Mar. 2013.

[69] X. Liu, Z. Cheng, H. Fan, S. Ai, and R. Han, “Electrochemical detection of avian influenza virus H5N1 gene sequence using a DNA aptamer immobilized onto a hybrid nanomaterial-modified electrode,” *Electrochim. Acta*, vol. 56, no. 18, pp. 6266–6270, 2011.

[70] S. Radhakrishnan, C. Sumathi, A. Umar, S. Jae Kim, J. Wilson, and V. Dharuman, “Polypyrrole–poly(3,4-ethylenedioxythiophene)–Ag (PPy–PEDOT–Ag) nanocomposite films for label-free electrochemical DNA sensing,” *Biosens. Bioelectron.*, vol. 47, pp. 133–140, Sep. 2013.

[71] K. B. Cederquist and S. O. Kelley, “Nanostructured biomolecular detectors: pushing

performance at the nanoscale," *Curr. Opin. Chem. Biol.*, vol. 16, no. 3–4, pp. 415–421, Aug. 2012.

[72] L. Soleymani, Z. Fang, E. H. Sargent, and S. O. Kelley, "Programming the detection limits of biosensors through controlled nanostructuring.," *Nat. Nanotechnol.*, vol. 4, no. 12, pp. 844–8, Dec. 2009.

[73] Q. Zhou, S. Wang, N. Jia, L. Liu, J. Yang, and Z. Jiang, "Synthesis of highly crystalline silver dendrites microscale nanostructures by electrodeposition," *Mater. Lett.*, vol. 60, no. 29–30, pp. 3789–3792, 2006.

[74] F. Li, X. Han, and S. Liu, "Development of an electrochemical DNA biosensor with a high sensitivity of fM by dendritic gold nanostructure modified electrode," *Biosens. Bioelectron.*, vol. 26, no. 5, pp. 2619–2625, Jan. 2011.

[75] L. Zhou, L. J. Ou, X. Chu, G. L. Shen, and R. Q. Yu, "Aptamer-based rolling circle amplification: A platform for electrochemical detection of protein," *Anal. Chem.*, vol. 79, no. 19, pp. 7492–7500, 2007.

[76] Y. Tian, H. Liu, G. Zhao, and T. Tatsuma, "Shape-controlled electrodeposition of gold nanostructures," *J. Phys. Chem. B*, vol. 110, no. 46, pp. 23478–23481, 2006.

[77] H. Liu, Y. Tian, and P. Xia, "Pyramidal, rodlike, spherical gold nanostructures for direct electron transfer of copper, zinc-superoxide dismutase: Application to superoxide anion biosensors," *Langmuir*, vol. 24, no. 12, pp. 6359–6366, 2008.

[78] C. X. Xu and X. W. Sun, "Field emission from zinc oxide nanopins," *Appl. Phys. Lett.*, vol. 83, no. 18, p. 3806, 2003.

[79] L. Jiang, G. Li, Q. Ji, and H. Peng, "Morphological control of flower-like ZnO nanostructures," *Mater. Lett.*, vol. 61, no. 10, pp. 1964–1967, 2007.

[80] L. Soleymani, Z. Fang, B. Lam, X. Bin, E. Vasilyeva, A. J. Ross, E. H. Sargent, and S. O. Kelley, "Hierarchical nanotextured microelectrodes overcome the molecular transport barrier to achieve rapid, direct bacterial detection," *ACS Nano*, vol. 5, no. 4, pp. 3360–3366, 2011.

[81] E. Vasilyeva, B. Lam, Z. Fang, M. D. Minden, E. H. Sargent, and S. O. Kelley, "Direct Genetic Analysis of Ten Cancer Cells: Tuning Sensor Structure and Molecular Probe Design for Efficient mRNA Capture," *Angew. Chemie Int. Ed.*, vol. 50, no. 18, pp. 4137–4141, Apr. 2011.

[82] E. Gultepe, D. Nagesha, S. Sridhar, and M. Amiji, "Nanoporous inorganic membranes or coatings for sustained drug delivery in implantable devices," *Adv. Drug Deliv. Rev.*, vol. 62, no. 3, pp. 305–315, Mar. 2010.

[83] A. Jane, R. Dronov, A. Hodges, and N. H. Voelcker, "Porous silicon biosensors on the advance," *Trends Biotechnol.*, vol. 27, no. 4, pp. 230–239, Apr. 2009.

[84] J. Li, A. Cassell, L. Delzeit, J. Han, and M. Meyyappan, "Novel Three-Dimensional Electrodes: Electrochemical Properties of Carbon Nanotube Ensembles," *J. Phys. Chem. B*, vol. 106, no. 36, pp. 9299–9305, Sep. 2002.

[85] Y. Zhang, S. Zha, and M. Liu, "Dual-Scale Porous Electrodes for Solid Oxide Fuel Cells from Polymer Foams," *Adv. Mater.*, vol. 17, no. 4, pp. 487–491, Feb. 2005.

[86] G. C. Martin, T. T. Su, I. H. Loh, E. Balizer, S. T. Kowel, and P. Kornreich, "The metallization of silicone polymers in the rubbery and the glassy state," *J. Appl. Phys.*, vol. 53, no. 1, pp. 797–799, 1982.

[87] N. Bowden, S. Brittain, and A. Evans, "Spontaneous formation of ordered structures in thin films of metals supported on an elastomeric polymer," *Nature*, vol. 393, no. May, pp. 146–149, 1998.

[88] A. L. Volynskii, S. Bazhenov, O. V. Lebedeva, and N. F. Bakeev, "Mechanical buckling instability of thin coatings deposited on soft polymer substrates," *J. Mater. Sci.*, vol. 35, no. 3, pp. 547–554, 2000.

[89] R. HUANG, "Kinetic wrinkling of an elastic film on a viscoelastic substrate," *J. Mech. Phys. Solids*, vol. 53, no. 1, pp. 63–89, Jan. 2005.

[90] H. Jiang, D.-Y. Khang, J. Song, Y. Sun, Y. Huang, and J. a Rogers, "Finite deformation mechanics in buckled thin films on compliant supports," *Proc. Natl. Acad. Sci.*, vol. 104, no. 40, pp. 15607–15612, Oct. 2007.

[91] J. Genzer and J. Groenewold, “Soft matter with hard skin: From skin wrinkles to templating and material characterization,” *Soft Matter*, vol. 2, no. 4, p. 310, 2006.

[92] C.-C. Fu, A. Grimes, M. Long, C. G. L. Ferri, B. D. Rich, S. Ghosh, S. Ghosh, L. P. Lee, A. Gopinathan, and M. Khine, “Tunable Nanowrinkles on Shape Memory Polymer Sheets,” *Adv. Mater.*, vol. 21, no. 44, pp. 4472–4476, Nov. 2009.

[93] A. Lendlein and S. Kelch, “Shape-Memory Polymers,” *Angew. Chemie Int. Ed.*, vol. 41, no. 12, p. 2034, Jun. 2002.

[94] J.-H. Zhao, M. Kiene, C. Hu, and P. S. Ho, “Thermal stress and glass transition of ultrathin polystyrene films,” *Appl. Phys. Lett.*, vol. 77, no. 18, p. 2843, 2000.

[95] C. Chen, D. Breslauer, J. Luna, and A. Grimes, “Shrinky-Dink microfluidics: 3D polystyrene chips,” *Lab Chip*, no. C, pp. 622–624, 2008.

[96] C. M. Gabardo, Y. Zhu, L. Soleymani, and J. M. Moran-Mirabal, “Bench-Top Fabrication of Hierarchically Structured High-Surface-Area Electrodes,” *Adv. Funct. Mater.*, vol. 23, no. 24, pp. 3030–3039, Jun. 2013.

[97] S. M. Woo, C. M. Gabardo, and L. Soleymani, “Prototyping of Wrinkled Nano-/Microstructured Electrodes for Electrochemical DNA Detection,” *Anal. Chem.*, vol. 86, no. 24, pp. 12341–12347, Dec. 2014.

[98] C. M. Gabardo, A. M. Kwong, and L. Soleymani, “Rapidly prototyped multi-scale electrodes to minimize the voltage requirements for bacterial cell lysis,” *Analyst*, vol. 140, no. 5, pp. 1599–1608, 2015.

[99] A. Hosseini and L. Soleymani, “Benchtop fabrication of multi-scale micro-electromagnets for capturing magnetic particles,” *Appl. Phys. Lett.*, vol. 105, no. 7, p. 074102, Aug. 2014.

[100] J. Watson and F. H. F. Crick, “Molecular structure of nucleic acids,” *Nature*, vol. 171, no. 4356, pp. 737–8, 1953.

[101] M. M. Cox, J. A. Doudna, and M. O’Donnell, *Molecular Biology*. Academic Press, 2011.

[102] X. Wang, H. J. Lim, and A. Son, “Characterization of denaturation and renaturation of DNA for DNA hybridization,” pp. 1–8, 2014.

[103] R. Weissleder, “A clearer vision for in vivo imaging Progress continues in the development of smaller , more penetrable probes for biological imaging . Toward the phosphoproteome,” *Nat. Biotechnol.*, vol. 19, no. 4, pp. 316–317, Apr. 2001.

[104] J. R. Lakowicz, *Principles of Fluorescence Spectroscopy Principles of Fluorescence Spectroscopy*. 2006.

[105] I. Johnson, *The Molecular Probes Handbook: A Guide to Fluorescent Probes and Labeling Technologies*. Life Technologies Corporation, 2010.

[106] C. R. Treadway, M. G. Hill, and J. K. Barton, “Charge transport through a molecular ??-stack: Double helical DNA,” *Chem. Phys.*, vol. 281, no. 2–3, pp. 409–428, 2002.

[107] E. M. Boon and J. K. Barton, “Charge transport in DNA,” *Curr. Opin. Struct. Biol.*, vol. 12, no. 3, pp. 320–329, 2002.

[108] M. E. Núñez, D. B. Hall, and J. K. Barton, “Long-range oxidative damage to DNA: Effects of distance and sequence,” *Chem. Biol.*, vol. 6, no. 2, pp. 85–97, 1999.

[109] S. Steenken, J. P. Telo, H. M. Novais, and L. P. Candeias, “One-electron-reduction potentials of pyrimidine bases, nucleosides, and nucleotides in aqueous solution. Consequences for DNA redox chemistry,” *J. Am. Chem. Soc.*, vol. 114, no. 12, pp. 4701–4709, 1992.

[110] M. A. Rosen, D. Live, and D. J. Patel, “Comparative NMR study of A(n)-bulge loops in DNA duplexes: intrahelical stacking of A, A-A, and A-A-A bulge loops,” *Biochemistry*, vol. 31, no. 16, pp. 4004–4014, 1992.

[111] P. K. Bhattacharya and J. K. Barton, “Influence of intervening mismatches on long-range guanine oxidation in DNA duplexes,” *J. Am. Chem. Soc.*, vol. 123, no. 36, pp. 8649–8656, 2001.

[112] T. T. Williams, D. T. Odom, and J. K. Barton, “Variations in DNA charge transport with nucleotide composition and sequence [12],” *J. Am. Chem. Soc.*, vol. 122, no. 37, pp. 9048–9049, 2000.

[113] S. O. Kelley, E. M. Boon, J. K. Barton, N. M. Jackson, and M. G. Hill, “Single-base

mismatch detection based on charge transduction through DNA.," *Nucleic Acids Res.*, vol. 27, no. 24, pp. 4830–4837, 1999.

[114] D. Mandler and S. Kraus-Ophir, "Self-assembled monolayers (SAMs) for electrochemical sensing," *J. Solid State Electrochem.*, vol. 15, no. 7–8, pp. 1–24, 2011.

[115] H. Häkkinen, "The gold–sulfur interface at the nanoscale," *Nat. Chem.*, vol. 4, no. 6, pp. 443–455, 2012.

[116] I. Turyan and D. Mandler, "Selective Determination of Cr(VI) by a Self-Assembled Monolayer-Based Electrode.," *Anal. Chem.*, vol. 69, no. 5, pp. 894–7, 1997.

[117] F. Davis and S. P. J. Higson, "Structured thin films as functional components within biosensors," *Biosens. Bioelectron.*, vol. 21, no. 1, pp. 1–20, 2005.

[118] T. Doneux, A. De Rache, E. Triffaux, A. Meunier, M. Steichen, and C. Buess-Herman, "Optimization of the Probe Coverage in DNA Biosensors by a One-Step Coadsorption Procedure," *ChemElectroChem*, vol. 1, no. 1, pp. 147–157, Jan. 2014.

[119] D. Mandler and I. Turyan, "Applications of Self-Assembled Monolayers in Electroanalytical Chemistry," *Electroanalysis*, vol. 8, no. 3, pp. 207–213, 1996.

[120] D. Grieshaber, R. MacKenzie, J. Vörös, and E. Reimhult, "Electrochemical biosensors-Sensor principles and architectures," *Sensors*, no. January, pp. 1400–1458, 2008.

[121] X. Zhang, H. Ju, and J. Wang, *Electrochemical Sensors, Biosensors and their Biomedical Applications*. Elsevier Science, 2008.

[122] a Numnuam, K. Y. Chumbimuni-Torres, Y. Xiang, R. Bash, P. Thavarungkul, P. Kanatharana, E. Pretsch, J. Wang, and E. Bakker, "Potentiometric detection of DNA hybridization," *J. Am. Chem. Soc.*, vol. 130, no. 2, pp. 410–411, 2008.

[123] J. Wu, K. Y. Chumbimuni-torres, M. Galik, C. Thammakhet, D. A. Haake, and J. Wang, "Potentiometric Detection of DNA Hybridization using Enzyme-Induced Metallization and a Silver Ion Selective Electrode," *Work*, vol. 81, no. 24, pp. 10007–10012, 2009.

[124] T. V. Shishkanova, R. Volf, M. Krondak, and V. Kr??l, "Functionalization of PVC membrane with ss oligonucleotides for a potentiometric biosensor," *Biosens. Bioelectron.*,

vol. 22, no. 11, pp. 2712–2717, 2007.

[125] J. Kafka, O. Pänke, B. Abendroth, and F. Lisdat, “A label-free DNA sensor based on impedance spectroscopy,” *Electrochim. Acta*, vol. 53, no. 25, pp. 7467–7474, Oct. 2008.

[126] A. Ebrahimi, P. Dak, E. Salm, S. Dash, S. V Garimella, R. Bashir, and M. a Alam, “Nanotextured superhydrophobic electrodes enable detection of attomolar-scale DNA concentration within a droplet by non-faradaic impedance spectroscopy,” *Lab Chip*, vol. 13, no. 21, p. 4248, 2013.

[127] K.-S. Ma, H. Zhou, J. Zoval, and M. Madou, “DNA hybridization detection by label free versus impedance amplifying label with impedance spectroscopy,” *Sensors Actuators B Chem.*, vol. 114, no. 1, pp. 58–64, Mar. 2006.

[128] E. M. Boon, D. M. Ceres, T. G. Drummond, M. G. Hill, and J. K. Barton, “Mutation detection by electrocatalysis at DNA-modified electrodes.,” *Nat. Biotechnol.*, vol. 18, no. 10, pp. 1096–1100, 2000.

[129] M. a. Lapierre, M. O’Keefe, B. J. Taft, and S. O. Kelley, “Electrocatalytic Detection of Pathogenic DNA Sequences and Antibiotic Resistance Markers,” *Anal. Chem.*, vol. 75, no. 22, pp. 6327–6333, 2003.

[130] T. M.-H. Lee, M. C. Carles, and I.-M. Hsing, “Microfabricated PCR-electrochemical device for simultaneous DNA amplification and detection.,” *Lab Chip*, vol. 3, no. 2, pp. 100–105, 2003.

[131] R. H. Liu, J. Yang, R. Lenigk, J. Bonanno, and P. Grodzinski, “Self-Contained, Fully Integrated Biochip for Sample Preparation, Polymerase Chain Reaction Amplification, and DNA Microarray Detection,” *Anal. Chem.*, vol. 76, no. 7, pp. 1824–1831, 2004.

[132] P. J. Asiello and A. J. Baeumner, “Miniaturized isothermal nucleic acid amplification, a review.,” *Lab Chip*, vol. 11, no. 8, pp. 1420–1430, 2011.

[133] M. U. Ahmed, Q. Hasan, M. Mosharraf Hossain, M. Saito, and E. Tamiya, “Meat species identification based on the loop mediated isothermal amplification and electrochemical DNA sensor,” *Food Control*, vol. 21, no. 5, pp. 599–605, 2010.

[134] K. Hsieh, A. S. Patterson, B. S. Ferguson, K. W. Plaxco, and H. T. Soh, "Rapid, sensitive, and quantitative detection of pathogenic DNA at the point of care through microfluidic electrochemical quantitative loop-mediated isothermal amplification," *Angew. Chemie - Int. Ed.*, vol. 51, no. 20, pp. 4896–4900, 2012.

[135] H. Ji, F. Yan, J. Lei, and H. Ju, "Ultrasensitive electrochemical detection of nucleic acids by template enhanced hybridization followed with rolling circle amplification," *Anal. Chem.*, vol. 84, no. 16, pp. 7166–7171, 2012.

[136] A. J. Bard and L. R. Faulkner, *Electrochemical Methods: Fundamentals and Applications, 2nd Edition*. Wiley Global Education, 2000.

[137] F. Sholz, *Electroanalytical Methods: A guide to Experiments and Applications*. Springer Berlin Heidelberg, 2010.

[138] D. Rand and R. Woods, "A study of the dissolution of platinum, palladium, rhodium and gold electrodes in 1 m sulphuric acid by cyclic voltammetry," *J. Electroanal. Chem. Interfacial …*, vol. 35, pp. 209–218, 1972.

[139] A. B. Steel, T. M. Herne, and M. J. Tarlov, "Electrochemical Quantitation of DNA Immobilized on Gold," *Anal. Chem.*, vol. 70, no. 22, pp. 4670–4677, Nov. 1998.

[140] K. C. Grabar, R. G. Freeman, M. B. Hommer, and M. J. Natan, "Preparation and Characterization of Au Colloid Monolayers," *Anal. Chem.*, vol. 67, no. 4, pp. 735–743, 1995.

[141] J. Turkevich, P. C. Stevenson, and J. Hillier, "A Study of the Nucleation and Growth Processes in the Synthesis of Colloidal Gold," *Discuss. faraday Soc.*, vol. 11, no. c, pp. 55–75, 1951.

[142] J. Hu, W. Li, J. Chen, X. Zhang, and X. Zhao, "Novel plating solution for electroless deposition of gold film onto glass surface," *Surf. Coatings Technol.*, vol. 202, no. 13, pp. 2922–2926, Mar. 2008.

[143] M. Steichen and C. Buess-Herman, "Electrochemical detection of the immobilization and hybridization of unlabeled linear and hairpin DNA on gold," *Electrochem. commun.*, vol. 7, no. 4, pp. 416–420, 2005.

[144] S. D. Keighley, P. Li, P. Estrela, and P. Migliorato, “Optimization of DNA immobilization on gold electrodes for label-free detection by electrochemical impedance spectroscopy,” *Biosens. Bioelectron.*, vol. 23, no. 8, pp. 1291–1297, 2008.

[145] K. Hu, D. Lan, X. Li, and S. Zhang, “Electrochemical DNA biosensor based on nanoporous gold electrode and multifunctional encoded DNA-Au bio bar codes,” *Anal. Chem.*, vol. 80, no. 23, pp. 9124–9130, 2008.

[146] P. Daggumati, Z. Matharu, and E. Seker, “Effect of Nanoporous Gold Thin Film Morphology on Electrochemical DNA Sensing,” *Anal. Chem.*, vol. 87, no. 16, pp. 8149–8156, 2015.

[147] S. Rho, D. Jahng, J. H. Lim, J. Choi, J. H. Chang, S. C. Lee, and K. J. Kim, “Electrochemical DNA biosensors based on thin gold films sputtered on capacitive nanoporous niobium oxide,” *Biosens. Bioelectron.*, vol. 23, no. 6, pp. 852–856, 2008.

[148] A. de la Escosura-Muñiz and A. Mekoçi, “Nanoparticle based enhancement of electrochemical DNA hybridization signal using nanoporous electrodes.,” *Chem. Commun. (Camb).*, vol. 46, no. 47, pp. 9007–9, 2010.

[149] P. Takmakov, I. Vlassiouk, and S. Smirnov, “Hydrothermally shrunk alumina nanopores and their application to DNA sensing.,” *Analyst*, vol. 131, no. 11, pp. 1248–1253, 2006.

[150] a B. Steel, R. L. Levicky, T. M. Herne, and M. J. Tarlov, “Immobilization of nucleic acids at solid surfaces: effect of oligonucleotide length on layer assembly.,” *Biophys. J.*, vol. 79, no. 2, pp. 975–981, 2000.

[151] R. Lao, S. Song, H. Wu, L. Wang, Z. Zhang, L. He, and C. Fan, “Electrochemical interrogation of DNA monolayers on gold surfaces.,” *Anal. Chem.*, vol. 77, no. 19, pp. 6475–80, Oct. 2005.

[152] Y. Cho, S. Kim, Y. A. Kim, H. Kyun, K. Lee, D. Yoon, G. Lim, Y. E. Pak, T. Hwan, and K. Kim, “Characterization of DNA immobilization and subsequent hybridization using in situ quartz crystal microbalance , fluorescence spectroscopy , and surface plasmon resonance,” vol. 278, pp. 44–52, 2004.

[153] A. Peterson, “The effect of surface probe density on DNA hybridization,” *Nucleic Acids*

Res., vol. 29, no. 24, pp. 5163–5168, 2001.

[154] B. P. Nelson, T. E. Grimsrud, M. R. Liles, R. M. Goodman, and R. M. Corn, "Surface plasmon resonance imaging measurements of DNA and RNA hybridization adsorption onto DNA microarrays," *Anal. Chem.*, vol. 73, no. 1, pp. 1–7, 2001.

[155] L. M. Demers, C. A. Mirkin, R. C. Mucic, R. A. Reynolds, R. L. Letsinger, R. Elghanian, and G. Viswanadham, "A fluorescence-based method for determining the surface coverage and hybridization efficiency of thiol-capped oligonucleotides bound to gold thin films and nanoparticles," *Anal. Chem.*, vol. 72, no. 22, pp. 5535–5541, 2000.

[156] K. Castelino, B. Kannan, and A. Majumdar, "Characterization of grafting density and binding efficiency of DNA and proteins on gold surfaces," *Langmuir*, vol. 21, no. 5, pp. 1956–1961, 2005.

[157] P. Gong and R. Levicky, "DNA surface hybridization regimes.," *Proc. Natl. Acad. Sci. U. S. A.*, vol. 105, no. 14, pp. 5301–5306, 2008.

[158] J. Wang, G. Rivas, M. Jiang, and X. Zhang, "Electrochemically induced release of DNA from gold ultramicroelectrodes," *Langmuir*, vol. 15, no. c, pp. 6541–6545, 1999.

[159] G. Wittmann, J. Szabon, P. Mohácsik, S. S. Nouriel, B. Gereben, C. Fekete, and R. M. Lechan, "Parallel Regulation of Thyroid Hormone Transporters OATP1c1 and MCT8 During and After Endotoxemia at the Blood-Brain Barrier of Male Rodents," *Endocrinology*, vol. 156, no. 4, pp. 1552–1564, Apr. 2015.

[160] M. Simbolo, M. Gottardi, V. Corbo, M. Fassan, A. Mafficini, G. Malpeli, R. T. Lawlor, and A. Scarpa, "DNA Qualification Workflow for Next Generation Sequencing of Histopathological Samples," *PLoS One*, vol. 8, no. 6, p. e62692, Jun. 2013.

[161] S. Sah, L. Chen, J. Houghton, J. Kemppainen, A. C. Marko, R. Zeigler, and G. J. Latham, "Functional DNA quantification guides accurate next-generation sequencing mutation detection in formalin-fixed, paraffin-embedded tumor biopsies," *Genome Med.*, vol. 5, no. 8, p. 77, 2013.

[162] C. Briones and M. Moreno, "Applications of peptide nucleic acids (PNAs) and locked nucleic acids (LNAs) in biosensor development," *Anal. Bioanal. Chem.*, vol. 402, no. 10,

pp. 3071–3089, 2012.

[163] P. E. Sheehan and L. J. Whitman, “Detection limits for nanoscale biosensors.,” *Nano Lett.*, vol. 5, no. 4, pp. 803–7, Apr. 2005.